Nanostructured Transition Metal Oxides as a Bifunctional Electrocatalyst for Water Splitting Reactions

By

Ramsha khan

School of Chemical and Material Engineering

National University of Sciences and Technology

August 2020

Nanostructured Transition Metal Oxides as a Bifunctional Electrocatalyst for Water Splitting Reactions

Name: Ramsha khan

Reg No: 00000273899

This thesis is submitted as partial fulfillment of the requirements for the degree of

MS in Chemical Engineering

Supervisor: Dr. Muhammad Taqi Mehran

School of Chemical and Material Engineering (SCME)

National University of Sciences and Technology (NUST)

H-12 Islamabad, Pakistan

August 2020

Dedication

This thesis is dedicated exclusively to the seekers, willing to do something in their lives.

Acknowledgements

First and foremost, I am grateful to **Almighty Allah,** who created; created man from the clot of congealed blood. Who taught man the use of pen, taught man that which he knew not.

I am in a debt of gratitude to my respected supervisor, **Dr. Muhammed Taqi Mehran**, for believing in my abilities. His incessant direction, encouragement and support was the driving force behind the success of this project. It was an honor working under his esteemed supervision and publishing a lot of data I have never thought.

I would like to encompass my sincere thankfulness to my worthy GEC members, **Dr. Salman Raza Naqvi, Dr Iftikhar Hussain Gul** and **Dr. Aftab Akram.**

The words are not in my command to compliment my loving and sweet mother, **Shakila Mobeen**, who has been my intellectual and spiritual inspiration. Her never-ending efforts and prayers sustained me at every stage of my life and invigorated me for attaining high goals. The greatest credit goes to my father, **Muhammad Aslam,** who pushed me get in this journey, which I was so not interested. I can never payback the encouragement, affection, and money of my father, who stimulated me to pursue my dream and complete my MS study. I can never forget to mention the great hustle created by my dear husband, **Mr. Muhammad Jabran Khan** to complete my research work. Thank you for supporting me and chilling me out, when I was mourning.

Lastly, I would like to pay my special thanks to my siblings, who are behind the scene editors. **Mishkoat khan,** and **Eishaal Fatima** thank you very much for understanding the load of this journey and doing my quarantine duties. **Muhammad Sameed Daniyal** and **Sachal Abdullah**, your efforts for cheering me up by fulfilling me with my everlasting craving, the biryani and bearing me on every weekend would be very much acknowledged. Deprived of this moral support, the thesis would have been much difficult.

Ramsha Khan

Table of Contents

List of Abbreviations

OER: Oxygen evolution reaction

HER: Hydrogen evolution reaction

Nickle: Ni

Strontium: Sr

Lanthanum: La

Titanium: Ti

Oxidation: Ox

Reduction: Red

Manganese: Mn

Iron: Fe

Oxygen: O

LDH: Layered double hydroxide

2D: 2 Dimensional

ECSA: Electrochemically active surface area

Pt: Platinum

List of Figures

List of Tables

Abstract

The electrochemical water splitting by using renewable electricity is being considered as a sustainable, clean, and considerable source of hydrogen fuel for future transportation and energy applications. However, the large-scale production of H_2 via water splitting is restrained due to the lesser stability of these electrode materials, effective proceeding of HER step in acidic media, as well as lethargic kinetics and high overpotential values of complex four-electron transfer OER process. Thus, ongoing research is based on fabricating effective bifunctional electrocatalyst, which can lessen the overpotential for OER and HER.

This study has been focused on developing efficient bifunctional electrocatalysts for water splitting reactions. The primary emphasis has been done on the preparation of perovskite materials and its composites with other transition metal oxides. The great flexibility in composition and crystal structure points them to the tuneable electronic structure of perovskite oxides. Herein, LSTN perovskite has been synthesized initially followed by its exsolution in a reduced environment. The composite of LSTN has been made with a NiMn-LDH, to develop a 3D hierarchical heterostructure LSTN@NiMn-layered double hydroxide ($La_{0.4}Sr_{0.4}Ti_{0.9}Ni_{0.1}O_{3-\delta}$ @NiMn-LDH) supported on highly conductive nickel foam. Another way to improve the characteristic property of LSTN, both for HER and OER was proposed and a composite of LSTN has been prepared with MXene to improve the conductive path for ion transportation. Currently, research has been driven towards double perovskite due to the stable nature of non-stoichiometric perovskite that has a great impact on transition metal 3d σ^*- antibonding (e_g) orbital electron filling. Moreover, the catalysts have been characterized by x-ray diffraction (XRD), Fourier transform infrared spectroscopy (FTIR), Raman spectroscopy, energy-dispersive x-ray spectroscopy (EDX), and Scanning electron microscopy (SEM). The results show that catalysts have been prepared successfully. The bifunctional activity of catalysts has been tested by calculating Tafel slope, overpotential, and mass activity. Among the prepared composites, LSTN@NiMn-LDH, LSTN/MXene 66.67%, and STPF-0.2 has shown the most proficient results with high stability and low resistance values.

Chapter No 1

Introduction

An energy system which is sustainable as well as eco-friendly and with least consumption of natural sources is one of the pivotal targets of scientist for future[1], [2]. According to the figures from 2013, global energy demand reached 18 TW, 80% of which is being derived from natural energy resources (coal, oil and gas)[3]. The increase in global energy demand is anticipated to be 24 or 26 TW up till 2040, under the scenario of "new policies" or "current policies" accordingly. Also, the increase in carbon dioxide emissions is predicted to be 37 or 44 Gt yr^{-1} in 2040, which was recorded to be 32 Gt yr^{-1} in 2013. And all this is to happen because of the rapid population growth and increased industrialization. The situation seems quite alarming because of the increase in energy demand and supply and a drastic decrease in the sources responsible for its production. Given to this, the world is putting its thought and resources to develop anergy systems which consume renewable energy sources (hydroelectric power, solar power and wind energy) for the sake of preservation of nature and climate[4].

An increase in the production and usage of renewable resources in electricity sector is pivotal, from the figures of 2010 it was only 2.1 TW out of 17.6 TW which is 12 % of the global energy demand[5]. The increased penetration of renewable resources is also required in transportation and chemical industry which was 19 % in 2010, i.e., 3.3 TW out of 17.6 TW, where 43% (1.4TW) of it was by light duty vehicles and the rest 57 % (1.9 TW) was consumed by heavy duty vehicles, rail, aviation and marine. Among the consumption by light duty vehicles electrification (electric cars) is already decarbonizing the environment but electrification in heavy duty vehicles is quite difficult[5]. As a result, it is anticipated that among light duty vehicles the energy demand will remain the same or even decrease but the consumption of energy by commercial transportation will rise by approximately 2/3 from 2010 to 2040, which is 1.9 to 3.2 TW. In the same way the energy demand in chemical industry is currently 8 % of global energy which is (1.5 TW) which is likely to grow by 2/3 from 2010 to 2040 which is 1.5 TW to 2.5 TW as the worldwide demand of plastic and fertilizer will increase[5]. Owing to all these

circumstances the world is focusing on the production of chemical fuels which are sustainable and are a much more natural and cheap resource of energy. For this the industrial chemicals like, methanol (40 Mt yr^{-1}), ethylene (115 Mt yr^{-1}), propylene (73 Mt yr^{-1}), hydrogen (50 Mt yr^{-1}), hydrogen peroxide (2.2 Mt yr^{-1}), ammonia (175 Mt yr^{-1}) etc., could be used as a sustainable energy resource for the production of chemicals to make products needed worldwide on daily basis with reduced emission of CO_2[6]. The **Fig. 1** illustrates the renewable sources for production of energy.

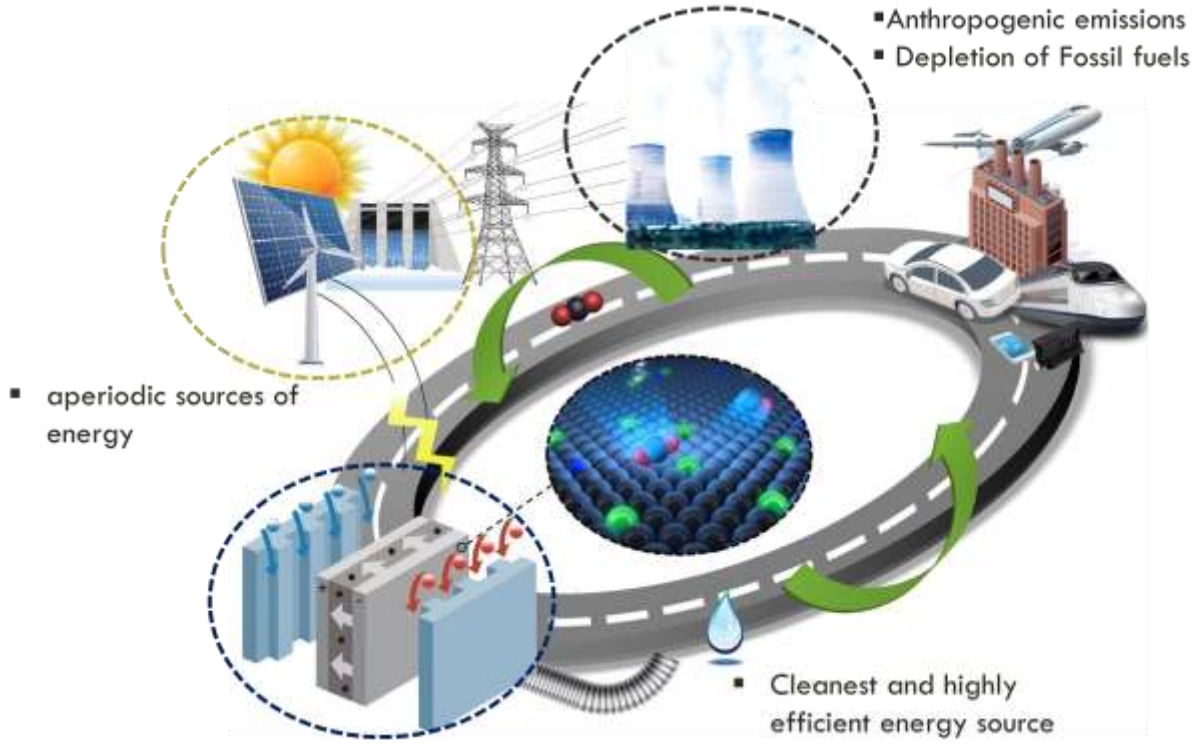

Figure 1: *Schematic illustration of resources that can be used for generating energy to perform water splitting.*

The Earth's atmosphere contains CO_2, nitrogen and water which can be used for the production of hydrocarbons, ammonia and oxygenates. These in turn can be used for the production of important fuels and chemicals by using electrochemical processes for renewable energy, but only if catalysts with suitable properties can be developed. For instance, for a sustainable source of hydrogen, water splitting reaction (oxygen and

hydrogen evolution half reactions) is of great scope[7], [8]. The stable hydrogen thus produced is used in various places, such as in fuel cells where hydrogen is oxidized and oxygen is reduced thus converting chemical energy into electrical energy, hydrogen peroxide being used in water treatment industries and in pulp/paper bleaching can also be gained from oxidation reduction reactions. In the same way, CO_2 in the atmosphere or coming from other sources can be used for the production of certain fuels, chemicals, polymers and plastics by preliminary electroreduction[3]. Similarly, nitrogen going through electrochemical process produces ammonia which is used for fertilizer production, and also on their application in a required concentration, also in Haber Bosch process and in the prevention of environmental hazards in case of run off. Given to all these uses of these natural resources an efficient and improved electrocatalysts with selective abilities for specific transformations is crucial[4].

For an enhanced electrocatalytic system two main methods are used

1. By providing more active sites on given electrode
2. Increasing the inherent activity of each active site

The respective ways are mutually exclusive and in an ideal case can be addressed simultaneously, thus giving the utmost improvement. But there are limitations to them as well such as, the maximum amount of charge that can be loaded on the electrode leaving the processes such as charge and mass transport unaffected.

For the generation of oxygen and hydrogen, electrochemical water splitting is an ideal strategy[9], [10]. However, the determining step of the water-splitting process i.e. (OER) oxygen evolution reaction which requires the formation of oxygen-oxygen bond and four proton-coupled electron transfer, which is quite a slow process having dallying kinetics[11]–[13] and thus require a catalyst. Up till now, inert metals or oxides, like RuO_2 and IrO_2 are considered as “state of the art” electrocatalysts for oxygen evolution reaction (OER), but they being expensive and rare are the hindrance between their large-scale production[14], [15]. Moreover, being unstable metals, they can undergo oxidation in alkaline electrolytes. Due to these reasons, extensive work and research are in process for the exploration of alternatives having aces as low cost, earth abundance, high efficiency, and stability[16], [17].

Significant efforts are required to develop catalytically active and economic electrocatalyst for large scale hydrogen production from water splitting reactions. In the past few years, many earth-abundant economical materials like metal phosphides, carbides[18], transition metal oxides[19] (e.g., perovskites and spinel oxides), carbonaceous materials, layered double hydroxides[20], [21], transition metal dichalcogenides[22]–[24], and selenides[25] have been studied on a wide-scale for OER. However, the utilization of most non-precious metal catalysts is still a challenge for HER as a catalyst showing higher activity for OER may not be active for HER. Thus, an electrolysis cell constructed for bifunctional activity does not meet the electrocatalytic performance standards for the overall water splitting process. Therefore, these challenges urge the researchers to develop a stable bifunctional electrocatalyst, equally active for OER as well as HER reaction.

1.1 Transition metal oxides

2D catalysts are catalytically more active than their 3D counterparts, as they provide more exposed active sites and highly conductive surface. The selective etching method in LDH nanosheets is a great way of enhancing OER activity. The problem associated with conductivity of catalysts can be resolved by directly growing metal oxides over Ni foam, that provide high surface area[26].

Moreover, carbon materials as a support (e.g., carbon paper, carbon nanotubes, reduced graphene oxides (rGO), etc.) are widely studied for improvement in the transference of charge, electrolyte accessibility of electrolyte, gas evacuation and electrochemically active surface area (ECSA)[27]. To achieve the smooth and fast charge transfer during electrochemical reactions, while attaining the best electronic properties and interfacial connection is very challenging. This requires defined hybridization of the electrocatalytically active phase into reactive[28]. MXene, which is two-dimensional (2D) early transition metal carbonitrides/carbides (e.g., Ti_3C_2, Ti_2C, Nb_2C, V_2C, Ti_3CN and Mo_2C, etc.), offers the possibility to satisfy the above mentioned requirements owing to well combination of hydrophilic surface, rich surface chemistries and metallic conductivity[29], [30]. The manufacture of MXene with various alignments is obtained by selectively etching layered MAX phase having general formula of $M_{n+1}AX_n$, where M

represents early transition metal, A is an element of group IIIA or IVA, X is C and/or N element, and n can be 1, 2, or 3[31], [32]. The process occurs by substituting the "A" atoms between $M_{n+1}X_n$ layers by following chemical groups, -O, -F and -OH, which subsequently provides a highly reactive MXene surface, but there are some exceptions in metallic conductivity such as semi-conductive Ti_2CO_2[33]. A new group of two-dimensional nano sheets MXene (early transition metal carbides/arbonitides), having its tremendous surface hydrophilicity and electrical conductivity are being produced. Researches have shown that in electrocatalytically active phases, MXene demonstrates improved catalytic activity while coupling, like graphitic C_3N_4/MXene hybrid film[34], MoS_2/MXene[35], ZIF-67/MXene[36], MnO_2/MXene[37], BGFSO/MXene hybrids[38]. But still the progression of MXene-based perovskite composites is in very early stages as compare to its hybrids with other 2D materials.

The designing of heterostructures have drawn great attention as bifunctional electrocatalyst as compared to the single component electrodes. A vigorous research has shown that the high activity of heterostructures is attributed to improved physical and chemical properties that are associated with the synergistic effects [39]. At present, some researchers have reported efficient heterostructured electrocatalysts for water splitting reactions. Geng et al.[40] presented a highly active bifunctional electrocatalyst based on NiFe-LDH ultrathin nanosheets grown on $NiCo_2O_4$ nanowire arrays. Similarly, Feng et al.[41] developed MoS_2/Ni_3S_2 heterostructures attaining the synergistic interfaces that enhanced the electrochemical performance of these heterostructures towards both OER and HER. Feng et al.[25] reported highly active 3D hybrid $Co_{0.85}Se$/NiFe LDH nanosheets which were vertically oriented on exfoliated graphene foil as overall water splitting electrocatalyst. Recently, Liu et al.[42] synthesized a heterointerface of cobalt and transition metal dichalcogenide supported on highly conductive CNT's formalized as Co/β-Mo_2C@N-CNT. The resulting heterostructure showed proficient performance towards water splitting and suggested a favorable way to achieve high catalytic activity for OER and HER.

In addition, the two-dimensional materials (2D) such as layered double hydroxides nanosheets (LDHs), have been proposed to be highly active for OER[43]. LDH's are

highly feasible due to their widely available active sites and greater surface to bulk ratio, as compared to the zero-dimensional (0D) and one-dimensional (1D) materials, yet, to make it available as a competitive candidate for OER reactions, it is required to improve its conductivity, increase electron and charge transfer ability along with the major issue associated with its stability. Zhang et al.[44] reported Mn^{+3} retained from δ-MnO_2 as a highly active OER site suggested from DFT calculations and experimentation. Therefore, NiMn LDH can be studied as an effective OER catalyst but to overcome the fundamental problem of lower electrical conductivity, Ni foam (NF) matrix can be used as a conductive substrate.

Transition metal oxides can possibly serve the purpose for traditional precious metal oxygen electrocatalyst, as they offer for the binding of oxygen species and are economical. Perovskites are considered superior due to their exceptional capability to accommodate various cations, with the facility of partial cationic substitution at A-site and B-site. The partial substitution serves several objectives such as it produces oxygen vacancy and create variable valance state of A/B site cations. The respective compositional changes and the electrochemical stability are the driving forces in perovskite oxides that enhance catalytic activity by monitoring the adsorption behavior of reaction intermediate[45], [46]. Perovskites are having an alleged formula of ABO_3, in this, A site is taken by rare-earth metals and transition metals occupy B-site, which represents fundamental and practical values owing to their compositional and structural flexibility, ionic & magnetic properties, unique electronic structure, low cost, environmental benignity and chemical durability[47]–[55]. Despite their high activity, their low conductivity, which increases the charge transfer resistance, and long-term stability is a problem which needs to be resolved to achieve high performance[15], [56].

1.2 Mechanism on the catalyst surface

1.2.1 Electrochemistry of water splitting

The catalyst is applied on anode and cathode where it assists in carrying out OER and HERs, by speeding up the water splitting mechanism[57]. The reaction can occur in an alkaline media or an acidic media with the given mechanism as follows[58], [59].

In acidic solution

At cathode

$$2H^+ = 2e^- \rightarrow H_2 \quad (1)$$

At anode

$$H_2O \rightarrow 2H^+ + \frac{1}{2}O_2 + 2e^- \quad (2)$$

In neutral or alkaline solution

At cathode

$$2H_2O + 2e^- \rightarrow 2OH^- \quad (3)$$

At anode

$$2OH^- \rightarrow H_2O + \frac{1}{2}O_2 + 2e^- \quad (4)$$

Alkaline electrolytes, in comparison with acidic electrolytes, allow precious metal catalysts such as platinum, Iridium, or ruthenium, to be substituted with inexpensive transition metal and/or functional carbon-based catalysts[60].

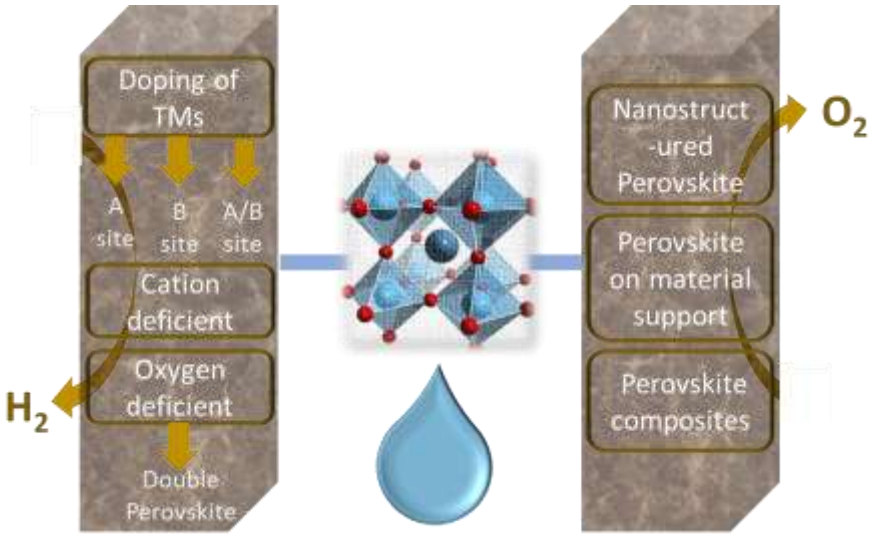

***Figure 2**: Schematic overview of different perovskite catalyst used for water splitting reaction of HER and OER*

1.2.2 Hydrogen evolution reaction mechanism

The overall HER in alkaline media operates at a standard potential of -0.829 V. Generally, three steps are involved in HER process, which are processed by three types of

reactions (Volmer, Heyrovsky and Tafel reaction), Eq. 5-9 in acidic and alkaline media[58]. These are given below[61], [62].

Volmer reaction (adsorption electrochemically) (Eq. 5-6)

$$H^+ + * + e^- \rightarrow H^*(\text{in acidic medium}) \quad (5)$$

$$H_2O + * + e^- \rightarrow H^* + OH^-(\text{in alkaline medium}) \quad (6)$$

Heyrovsky reaction (desorption electrochemically) (Eq. 7-8)

$$H^* + H^+ + e^- \rightarrow * + H_2(\text{in acidic medium}) \quad (7)$$

$$H^* + H_2O + e^- \rightarrow * + H_2 + OH^-(\text{in alkaline medium}) \quad (8)$$

Or Tafel reaction (desorbed chemically) is expressed in Eq. 9.

$$2H^* \rightarrow 2 * + H_2 \quad (9)$$

Volmer reaction pathways are involved in Heyrovsky and Tafel steps that involves the molecular adsorption of H_2O molecules over the bared active sites. The process is followed by electrochemical reduction of water molecule that got adsorbed on active site into H^* and OH^-, that leads to desorption of OH^- and finally hydrogen molecule leaves the surface. A mechanism was suggested for perovskite oxide catalyst exhibits that perovskite oxide own non-metal reactive site, rather a surface charged oxygen that is negatively charged serves the purpose. A mechanism showing alkaline HER steps, given in **Fig. 3**, was proposed by Xu et al. [63]. The efficacy of $Pr_{0.5}(Ba_{0.5}Sr_{0.5})_{0.5}Co_{0.8}Fe_{0.2}O_{3-\delta}$ perovskite oxide in catalysing HER is discussed. The mechanism presents that the water molecule available from electron and electrolyte, that interaction with an active site occupied by oxygen to evolve as an intermediate given as adsorbed H^*, where, the metal sites in vicinity either gets or reduced (with oxidation state toggle between n+1 and n). Though, the involvement of second step (Heyrovsky reaction or Tafel reaction) is not easy to guess, various reaction intermediates are obtained in OER/ORR. But, there is only one intermediate achieved during the two electron transfer HER, this thus, provides zero overpotential for highly active catalysts (e.g., Pt)[64], which shows a need to improve perovskite catalysts. HER rate depends on binding potential of H^* intermediate, which is generally given free energy for hydrogen adsorption (ΔG_H)[65]. The efficicency of HER

catalyst depends upon its binding ability of hydrogen, which should be intermediate, neither too strong nor too weak, providing a ΔG_H value close to zero[56].

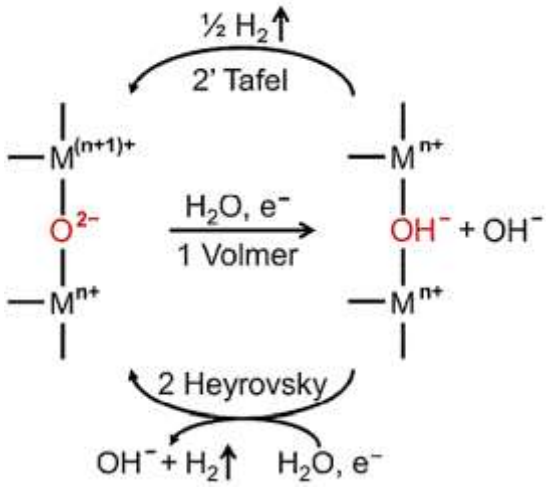

***Figure 3**:Mechanism proposed for HER on the surface of perovskite oxide (Reprinted with permission of ref. 47 copyright © 2016 WILEY-VCH Verlag GmbH & Co. KGaA, Weinheim).*

1.2.3 OER/ORR reaction mechanism

Tseung and Jasem[62], in 1977, proposed the idea that more active sites are formed with higher states of oxidation, if the transition metals were coupled with redox electrode at lower potentials than the oxygen electrode. This resulted in the preparation of an exceptional catalyst with better electrical conductivity and an active OER/ORR catalyst. Trasatti[66],[67] from 1980–1984, researched on perovskite-type oxides and found that OER overpotential and enthalpy of transition from lower oxidation state to higher oxidation state had volcano-type relationship. Meanwhile, Bockris and Otagawa[68], [69] investigated eighteen different perovskite oxides and found that the enthalpy of formation of $M(OH)_3$ hydroxide is inversely related to current density when tested under constant overpotential.

Man et al.[70] suggested an extension of the originally proposed mechanism. In Fig. 4(b) The mechanism is a combination of a series of acid-base steps involving the oxygen nucleophile(OH^-), that attacks a Lewis base, which is a metal-bound electrophile [62]. The ORR reaction in alkaline solution can be written as $O_2 + 2H_2O + 4e^- \rightarrow 4OH^-$[59], whose standard electrode potential is 0.401 V. The reaction proceeds via four

step proton coupled process taking place at metal sites[71]. The reactions are sequenced as 1). Hydroxide displacement; 2). Peroxide formation; 3). Oxide formation; and 4). Regeneration of hydroxide as shown in Fig. 4(c). The first step involves H_2O or molecular O_2 and electron, that reacts with metal surface sites to produce oxygenated products given as OO^*, OOH^*, O^* and OH^*, where * represents a reactive site on catalytic surface. The oxidation and reduction (redox) of surface metal sites accompany these oxygenated adsorbates whose oxidation state varies between n+ and n+1. The reaction kinetics for ORR is largely dependent on oxygen binding energy and surface metal sites. The weak binding energy for oxygen refers OH^* to OO^* displacement as the rate determining step (RDS), whereas, too strong of an oxygen binding energy directs the last transition step of O^* to OH^* as rate limiting step (RLS). According to Sabatier principle, an optimum perovskite catalyst has moderate oxygen binding energy[71],[72]. Suntivich et al. [73], [74] declared that e_g orbital filling in metal cations strongly affects the rate-determining steps, arguing that, if the e_g filling was to be greater than 1, the formation of O-O bond in OOH^* adsorbate would actually determine the rate. While for less than 1, the formation of peroxide ion from oxyhydroxide, can be rate determining step (RDS). In Fig. 4(d) a similar mechanism can be found for OER with the regeneration and disappearance of OH^-. For OER, the reaction on perovskite surface in an alkaline media can be written as $4OH^- \rightarrow O_2 + 4e^- + 2H_2O$, which undergoes four sequential steps given as: 1) Hydroxide deprotonation; 2) Peroxide formation; 3) Peroxide deprotonation; and 4) Hydroxide formation (Fig. 4(d)). In the following mechanism, OH^- from electrolyte interacts with the metal sites undergoing redox reaction at metal surfaces while the oxidation state changes between n+ and n+1. The reactive intermediates are sequenced as O*, OOH^*, OO^*, and OH^*. The reaction kinetics for OER is also controlled by binding strength of oxygen with metal sites. The peroxide formation (O^* to OOH^*) stands for the rate limiting step (RLS), where oxygen binds too weakly. While, in deprotonation step (OOH^* to OO^*), where, oxygen binds too strongly, it serves as a rate determining step (RDS)[73]. The binding strength of the surface oxygen adsorbate in OER and ORR are highly interlinked due to scaling relations[70], computing the non-zero overpotential for many observed perovskites.

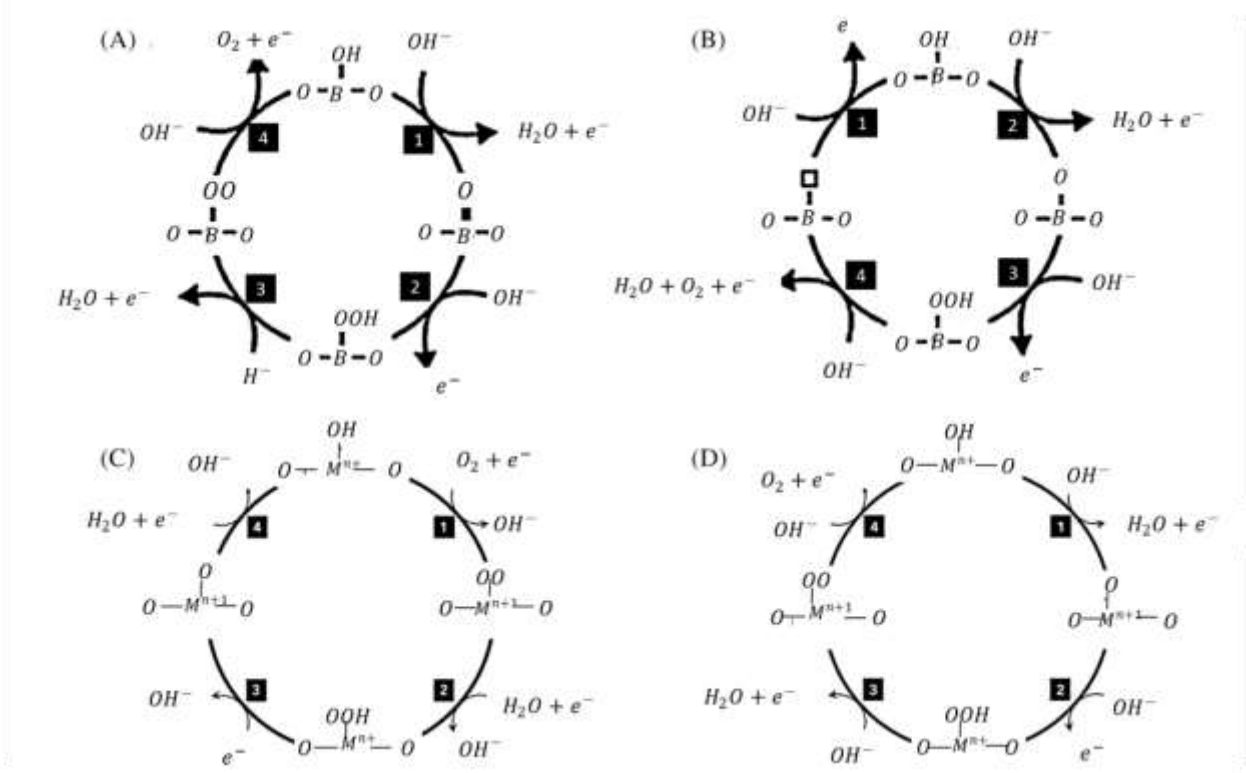

Figure 4: *OER/ORR mechanism proposed for oxide surfaces59. (a) Four-step reaction mechanism proposed by Goodenough et al. for the ORR on perovskite surfaces60. (b) Four-step reaction mechanism proposed by Rossmeisl and co-workers for the OER on noble metal catalyst surfaces*[70] *and then applied to oxide surfaces*[75]*. (c) Four-electron ORR mechanism for perovskite surface (d) Four-electron OER mechanism on perovskite surface in alkaline solution*[71]*. (Reprinted with permission from the above references).*

The density functional theory's (DFT) calculations propose different types of intermediates on perovskite oxide surfaces in above mentioned ORR/OER mechanisms. Although, the calculated elementary steps are similar, but the intermediates are in the order of O_2^*, OOH^*, O^*, and OH^* for ORR[76], while for OER, the order is reversed on metal sites (OH^*, O^*, OOH^* and O_2^*)[75]. The varying surface properties of metal surfaces and perovskite oxides are responsible for such difference. The scaling relation can be utilized between adsorption energies of oxygen binding species taking part in reaction mechanism as shown in Eq. 6-9[70], [77]. A single descriptor defines the deviation of theoretical overpotential between two oxide surfaces, which is given as either the oxygen adsorption energy (ΔG_o)[77] or the relative stability of OH^* vs OOH^*

($\Delta G_{OH} - \Delta G_{OOH}$)[70]. Consequently, a volcano shaped relation based on Sabatier's principle was obtained, which locates $LaNiO_3$ and $SrCoO_3$ close to the top due to their lowest overpotential, attained as a result of optimal binding of oxygen. While, the strong oxygen bonding places $LaCoO_3$, $LaFeO_3$, $LaMnO_3$, $LaCrO_3$, $LaVO_3$ to the left side, contrarily, $LaCuO_3$ to the right side of volcano, owing to its weak oxygen binding.

$$* + H_2O \rightarrow OH^* + e^- + H^+ \quad (10)$$

$$OH^* \rightarrow O^* + e^- + H^+ \quad (11)$$

$$O^* + H_2O \rightarrow OOH^* + e^- + H^+ \quad (12)$$

$$OOH^* \rightarrow O_2 + e^- + H^+ \quad (13)$$

Since, following studies cannot elaborate the current experimental findings based on doped transition metal oxides such as BSCF[78], LSTN[79], because they do not follow the formerly proposed mechanism. Mefford et al.[80] recently proposed using DFT calculations that the high catalytic activity of $La_{1-x}Sr_xO_{3-\delta}$ and its similar compounds can be justified by the involvement of lattice oxygen in OER mechanism. Moreover, a latest study based on DFT calculations showed the new OER mechanism (Eq. 10-13[81]), in which lattice oxygen contributes through the formation of surface oxygen vacancy (V_o), reversibly[81]. The shifting of surface lattice oxygen out of the plane is highly promising in order to interact with OH* to form V_o and OO^* on $LaNiO_3$ and other perovskites that are not highly stable.

$$OH^* \rightarrow (V_o + OO^*) + H^+ + e^- \quad (14)$$

$$(V_o + OO^*) + H_2O \rightarrow O_2 + (V_o + OH^*) + H^+ + e^- \quad (15)$$

$$(V_o + OH^*) + H_2O \rightarrow (H^*_{O-site} + OH^*) + H^+ + e^- \quad (16)$$

$$(H^*_{O-site} + OH^*) \rightarrow OH^* + H^+ + e^- \quad (17)$$

Thus, the two proposed mechanisms for OER, adsorbate evolution mechanism (AEM) shown in Eq. 6-9[70], [77], and lattice-oxygen participation mechanism (LOM) presented in Eq. 14-17[81], can participate on defining highly active perovskites. **Fig. 5** shows the possible preferred mechanism for different perovskite among AEM and LOM.

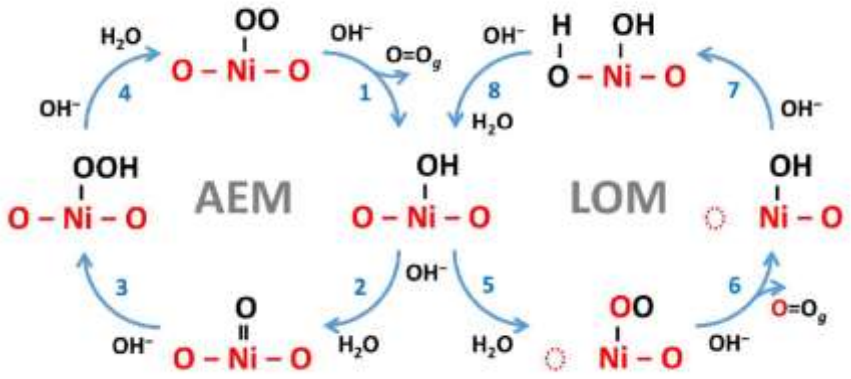

Figure 5: *Schematic illustration of adsorbate evolution mechanism and lattice-oxygen participating mechanism (Reprinted with permission ref.*[68] *Copyright © American Chemical Society.*

Chapter No 2

Literature review

Starting from the late ’90s, when researchers diverted their attention towards the cheaper sources of catalysing such reactions, perovskites were considered a good opportunity for research. Practically, the activity of perovskite electrocatalyst can be enhanced in two ways. One is to aim the intrinsic increment in the activity of each reactive site by accounting the physicochemical properties of perovskite electronic structures. These properties include a range of composition achieved by substitution, oxygen vacancy and diverse crystal structures. The other is to extrinsically increase the activity and number of reactive sites which is a function of geometric effect. This can be achieved by proposing novel methods for the synthesis of perovskite nanostructures and its composites. These parameters are interrelated, changing the composition could directly alter the oxygen vacancy as well as crystal structure. For instance, both extrinsic and intrinsic properties can undergo simultaneous increment in some cases[56].

2.1 Composition of the perovskite

The substitution of B-site/A-site elements strongly influence the activity of the catalyst through modification in the electronic structure. Combining the rare earth metal with transition metal induces alteration in net positive charge contribution by metal cations at A-site. This does not only change the oxidation state but also influences the spin state of transition metal cations and may create an oxygen vacancy[13]. Most of the work has been done on doping rare earth metals at A-site and transition metals at B-site while comparing their properties. Starting from the results shown by A-site dopant catalyst towards doping at both A/B site.

2.1.1 A-site doping ($A_{1-x}A'_xBO_3$)

Lanthanum has been used most excessively as an A-site element placed for rare earth metal. A-site doping clearly enhances the catalytic activity depending upon stoichiometry and method of preparation. Shao et al. [82] worked on strontium-based lanthanum $La_{1-x}Sr_xFeO_{3-\delta}$ (x = 0, 0.2, 0.5, 0.8, and 1) perovskite catalyst and found one with composition showing the best OER activity in alkaline solution. The increment in Sr doping directly

reduces the lattice size due to oxidation of Fe^{2+} to Fe^{3+} and compensation of charge when Sr^{2+} substitutes La^{3+}. As Sr doping enhances the activity, a very unique structured strontium doped perovskite was presented by Jin and Gao[83], who synthesized an urchin-like $La_{0.8}Sr_{0.2}MnO_3$ (LSM) perovskite via co-precipitation method with urea precipitator for ORR and OERs. The high specific surface area, LSV results for OER and high cathodic current density (3.7 mA cm^{-2} at 0.9 V (vs. Ag/AgCl)) of LSM created a huge impact on bifunctional catalytic activity. The sphere diameter was 3-5 µm, while the thorn length was 0.2-0.6 µm. Urchin like LSM showed linear and parallel plots for applied potentials, representing the first-order kinetics of O_2 and dependence on the following electrocatalyst [83]. A similar contribution was made by Tulloch et al. [84] who worked on $La_{1-x}Sr_xMnO_3$ type perovskite for even values of X (0-1) and found $La_{0.4}Sr_{0.6}MnO_3$ to be most active towards oxygen reduction reaction. The catalyst was found to be quite crystalline with low surface area (<1m^2 g^{-1}) and a high degree of porosity.

2.1.2 B-site doping ($AB_{1-x}B'_xO_3$)

The catalytic activity of perovskite oxides is more directly affected by B-site doping as compared to A-site, because B-site is available as a more reactive site in conventional mechanisms proposed for OER/ORR. A range of Transition metal oxides is available whose doping at B-site strongly influences the perovskite catalytic properties. Fe and Ni being the most prominent ones, because of having high optimal energy. Duan et al. [85] studied the Fe substitution at B-site in $LaCoO_3$ which has the ability to increase the OER performance of perovskite-type oxide. The increased spin state of Co^{3+} in $LaCoO_3$ resulted in high OER performance due to a 10% substitution of Fe.

2.1.3 A/B site Doping ($A_{1-x}A'_xB_{1-y}B'_yO_3$)

Doping of both, rare earth metal and transition metal increases the surface roughness and availability of active sites. In this case, a more thorough investigation is needed to locate the optimal composition for higher activity. Depending upon the material doped, the adopted method modifies their structural properties. Several methods have been proposed to develop the quaternary perovskite catalyst, providing with different catalytic properties and structures. Singh et al. [86] studied the influence of substituting the transition metals

in $La_{0.8}Sr_{0.2}Co_{1-y}$ B_yO_3, where B can be Ni, Fe, Cu, and Cr on a strontium doped perovskite. The electrocatalytic properties of the following catalysts and found a pair of redox peaks before the onset of OER via CV has been revealed. The substitution of transition metals at B-site significantly increased the surface roughness, thus providing a large active surface area.

Barium based strontium doped cobalt iron perovskite oxide has been studied for many years, because of the high charge transferability. J. May et al. [87] reported $Ba_{0.5}Sr_{0.5}Co_{0.8}Fe_{0.2}O_{3-\delta}$ (BSCF82), to be the best catalyst for water oxidation reaction in an alkaline solution. The focus was on the stability and changes in surface morphology occurring during OER for many catalysts, like BSCF82, $La_{0.4}Sr_{0.6}CoO_{3-\delta}$ (LSC46), $LaCoO_3$ (LCO) and $LaMnO_3$ (LMO) via HRTEM. As the cluster size of cobalt atoms increases, the OER activity reduces[87]. Jin and Gao[78] reported in the same area, with a different stoichiometry of rare earth metals (x=0.5), studying the electrochemical behavior of $Ba_{0.5}Sr_{0.5}Co_{0.8}Fe_{0.2}O_3$ (BSCF). It has been confirmed that it is useful as a bifunctional catalyst (OER and ORR) in alkaline media. The catalyst exhibits the limiting current density comparable to 20 wt% Pt/C. But the onset potential is lower than Pt/C catalyst, when compared to Jin and Gao's work because of diffusion limiting current density exhibited by BSCF perovskite catalyst. This is due to the different type of interactions of O_2 on electrocatalyst and adsorption of different nature of species on transition metal cations. Thus, BSCF can be considered as a promising bifunctional catalyst when used in an alkaline media[78].

To analyze the effect of other rare earth metals such as Pr doping in perovskite structure, Bu et al. [8] worked on the substitution of Pr in BSCF perovskite-type oxide that is having high oxygen vacancies, which shows higher stability and good electrical conductivity. The presence of higher oxygen vacancy and oxidation state of cobalt exceptionally increases the ORR/OER activity. It exhibited the high electron transfer number 3.77-3.89 within a potential range of 0.3-0.6 V. It also indicated the higher cycling stability in a charge-discharge curve and thus, proved to produce a promising future for OER/ORR.

Highly stable substituted perovskite structure based on ruthenium as B-site dopant was developed by Chang et al. [88] reported $La_{0.6}Ca_{0.4}Co_{0.8}Ru_{0.2}O_3$ powders prepared by amorphous citrate precursor method for ORR. A foam-like microporous structure is formed with pore size in the range of 0.5-3.0 μm. The improved catalytic ability for this catalyst is attributed to a higher hydrogen peroxide deposition rate in the KOH solution. The results for the polarization curve of $La_{0.6}Ca_{0.4}Co_{0.8}Ru_{0.2}O_3$, $La_{0.6}Ca_{0.4}Co_{0.8}Ru_{0.2}O_3$/BP2000 (black pearl 2000), and $La_{0.6}Ca_{0.4}CoO_3$/BP2000.

2.1.4 Main group element doping at cation site

Substitution of transition metals and rare earth metals has been a common practice in research, but a new idea of doping catalytically inactive compound at B-site was proposed that can assist in electronic structure tuning of redox-active metal and thus, can enhance the catalytic activity. Shao et al. [89] reported the utilization of phosphorous, a non-metal as a dopant on the cation site for developing a new perovskite oxide. The different compositions of phosphorous like, $La_{0.8}Sr_{0.2}\ Mn_{1-x}\ O_{3-\delta}\ P_x$ (x = 0, 0.02, 0.05, and 0.1, denoted as LSM, LSMP-0.02, LSMP-0.05, and LSMP-0.1) and found that phosphorous is soluble at 0.05 composition. The 5 % doping of P not only enhances the electrocatalytic activity, but also greatly influences its stability, due to its exceptional electrical conductance and providence of highly reactive oxygen species in abundance. The LSMP0.05 has shown the highest BET surface area of 27.3 $m^2\ g^{-1}$ with high kinetic current density value (2.97 mA cm^{-2}) among them for ORR[89] . The same approach has been applied on $SrCo_{0.95}P_{0.05}O_{3-\delta}$(SCP)[90] and Mo doping in $Ba_2CoMo_{0.5}Nb_{0.5}O_{6-\delta}$(BCMN) [91] composition and found it a very stable and high in its activity for OER. The approach has opened a new research phase for other non-metal doped perovskite oxides as bifunctional catalysts.

A similar approach was again designed to achieve high activity by the Shao et al. [92] The enhanced OER activity of Iron-based perovskite has been discussed, when it is doped by earth-abundant Si metalloid $SrFe_{0.9}Si_{0.1}O_{3-\delta}$ (SFSi). This newly prepared catalyst exhibits an exceptional electrochemical property demonstrating a small Tafel slope. SFSi shows OER intrinsic activity that is about 3 times higher than SF under these potentials: 0.13 ± 0.02 mA cm^{-2}_{oxide} for SFSi and 0.05 ± 0.01 mA cm^{-2}_{oxide} for SF at η = 0.4 V. This

idea of doping earth-abundant elements results in cost-effective and high-performance electrocatalyst[92].

2.1.5 Cation deficient Perovskite

Anion deficiency has known to be very popular and a lot of work has been done in this area. But cationic deficiency is still a topic of research. Non stoichiometry of perovskite structure favours OER and HERs by facilitating H_2 adsorption. Zhu et al. [93] worked on developing a catalyst with cationic deficiency at A site that favors the catalytic activity in terms of ORR and OERs. The employment of $LaFeO_3$ in an alkaline solution and found definite results for OER than ORR. Among the prepared perovskites of $La_{1-x}FeO_{3-\delta}$ $L_{0.95}F$ showed the best performance for both reactions. The provision of oxygen vacancies at the surface and the presence of Fe^{4+} species in A-site cation deficient perovskite were the reason for high activity. Thus, these results make it a promising bifunctional catalyst. Similar work was presented by Shao et al. [79] who prepared a non-stoichiometric hybrid catalyst with metal nanoparticles homogeneously dispersed on the perovskite backbone via insitu- exsolution process. Exolved-$La_{0.4}Sr_{0.4}Ti_{0.9}Ni_{0.1}$(LSTN), Ex-$La_{0.4}Sr_{0.4}Ti_{0.9}Co_{0.1}$(LSTC), Ex-$La_{0.4}Sr_{0.4}Ti_{0.9}Fe_{0.1}$(LSTF), Ex-$La_{0.4}Sr_{0.4}Ti_{0.9}Ni_{0.075}Fe_{0.025}$(LSTNF), and Ex-$La_{0.4}Sr_{0.4}Ti_{0.9}Ni_{0.05}Co_{0.05}$(LSTNC) have been prepared by the same process. Among them, Ex-LSTN showed the highest activity for hydrogen evolution reaction, because of the presence of optimal free energy of H_2 adsorption, but shows inferior activity for OER in which cobalt performs better. Recently, Islam et al. [94] also presented exsolved $Sr_{0.95}Nb_{0.1}Co_{0.9-x}Ni_xO_{3-\delta}$ (SNCN) as a trifunctional catalyst in which Ni-Co NPs has undergone exsolution. Liu et al. [95] also developed cation deficient $Sr_{1-x}Nb_{0.1}Co_{0.7}Fe_{0.2}O_{3-\delta}$ (x = 0.02, 0.05 and 0.1), denoted as S0.98NCF, S0.95NCF and S0.90NCF that resulted shrinkage in crystal structure and diverse oxidation states. **Table. 9** is shown in appendices that give a brief insight to activity of perovskites for OER.

2.2 Oxygen deficient Perovskites

The creation of oxygen-deficient oxides results in an immediate filling and formation of lattice oxygen vacancies, which play a vital role in their intrinsic OER/ORR and HER activities. Catalytic activity is a strong function of oxygen deficiency concentration,

resulting in a distorted structure that is non-cubic. Mefford et al. [80] found that the OER activity of the $La_{1-x}Sr_xCoO_{3-\delta}$ series is a strong function of oxygen vacancy concentration, with the highest activity obtained on $SrCoO_{2.7}$ and the largest vacancy content. Yuasa et al. [96] published their work on LSFM with (x = 0-0.4) and (y = 0-0.8) prepared by reverse miscella method to develop the unique properties for ORR. $La_{0.6}Sr_{0.4}Mn_{0.8}Fe_{0.2}O_{3+\delta}$ loaded electrode has shown the higher ORR activity at the current density above 80 mA cm^{-2} than the Pt/C, but the activity reduced on decreasing the current density. Although, the performance increased as x is increased and decreased on increasing y, but the oxides preparation for greater x was not satisfactory. The durability test was much more stable for x = y = 0.2 perovskite-type oxide[96].

Singh et al. [97], worked on this type of perovskite with general formula $MMoO_4$ (where, M = Co, Fe or Ni). The Fe doping on-base oxides of $MMoO_4$ with M as Ni and Co results in enhanced catalytic activity by increasing the current density by 11 times for $CoMoO_4$ and 15 times for $NiMoO_4$. The doping of Fe in $Cr_2(MoO_4)_3$ improves the catalytic property by reducing the Tafel slope an enhancing the specific activity by 80 times[98].

Different types of structures are obtained upon creating oxygen defects. Zhou et al. [99] claimed that the crystal structure has a direct effect on ORR and OER activities. The experiments were performed on different crystalline structures of $LaNiO_{3-\delta}$ obtained from heating at 400 ºC, 600 ºC and 800 ºC temperatures. The ORR/OER performance increased when the transition occurred from rhombohedral to cubic. Ni-O bond length elongation in cubic structure favors high OER/ORR performance[99].

Along moving with oxygen-deficient perovskite, Zhang et al. [100] analyzed the oxidation state of Mn in perovskite-type oxides. A method is proposed of improving the electrocatalytic activity of non-stoichiometric $CaMnO_{3-\delta}$ type perovskite by introducing the facile technique, that will originate the oxygen defects. The work was further taken by Kim et al. [101] declaring the $Ca_2Mn_2O_5$ electrocatalyst for OER in alkaline media and found it to be catalytically more active than $CaMnO_3$ reported by Zhang et al. [100]. $Ca_2Mn_2O_5$ showed 30.1 A/g at 1.70 V (vs RHE) of mass activity for OER. The most promising factors for the enhanced activity are the high porosity due to oxygen vacancy and the manganese's high spin electronic configuration in a crystallatic morphology. The

difference was found in developing the catalyst by a new method, named as reductive annealing process. The crystal structure supports the easier transport of OH^- ion, thus, contributing towards making this catalyst highly active.

The properties of oxygen-deficient perovskite can be further enhanced by adopting a suitable method for preparing small-sized nanoparticles as an electrocatalyst. Chen et al.[102] mentioned barium-based oxygen-deficient bifunctional electrocatalyst. It was reported that $BaTiO_{3-x}$ nanoparticles are prepared by the sol-gel method, which exhibit much higher OER performance than precious noble metals prepared by similar method. It has exhibited much negative onset potentials and higher current densities at low potentials <1.6V than IrO_2 and higher oxygen vacancies, that are responsible for easier adsorption and charge transfer phenomenon for OER.

As we know, the substitution of transition metals at the cation site enhances the catalytic activity and the effect gets more pronounced on creating oxygen defects. Doping Ni in manganite type perovskite $La_{0.8}Sr_{0.2}Mn_{1-x}Ni_xO_3$ and compared it with undoped catalyst was reported by Wang et al. [103]. Both were prepared via facile sol-gel technique for ORR and OER activities. The Ni doping enhanced the catalytic activity by providing more oxygen vacancies, due to the presence of significant Ni^{3+} on the surface. BET surface area of $La_{0.8}Sr_{0.2}Mn_{0.6}Ni_{0.4}O_3$ turned out to be 14.41 $m^2\ g^{-1}$, nearly double to that of the undoped $La_{0.8}Sr_{0.2}MnO_3$, (8.69 $m^2\ g^{-1}$). The prepared catalyst showed much-reduced overpotential and long-term stability of 79 cycles within 2.0 - 4.8 V (vs. Li^+/Li), comparable to Pt/C at a much lower cost. P block metal due to their good conducting properties is also a good option for doping. Christ et al. [104] worked on synthesizing Al-doped $Ca_xLa_{(1-x)}Al_{(1-x)}Mn_xO_{(3-\delta)}$ perovskite oxides via solid-state(SS) reaction, hybrid sol-gel, and aerogel synthesis technique, with the aim of developing a catalyst with the high surface area for ORR. Among the prepared samples from SS technique, $Ca_{0.9}La_{0.1}Al_{0.1}Mn_{0.9}O_{3-\delta}$ (9119) was found with maximum homogeneous elemental distribution. and it showed the highest performance in tested electrochemical properties. The same sample was tested for other techniques, aerogel method produced the highest surface area of 6.1 m^2g^{-1} and thus, the highest mass activity of 108 mA mg^{-1}, but the reduction of oxide structure under low potential is a big concern.

In the same area, Jing Xia et al. [105] did a substitution of P block metals at A sites and found the availability of surface-active sites that originate due to non-stoichiometric behavior of oxygen. Unfilled d orbitals in p-block metals induce a dual nature of property in them, associated with metallicity and non-metallicity, which results in dissociation of p-block metals ions on increased alkalinity with the availability of increased vacant sites at the surface. Shao et al. [106] prepared another perovskite via different approach, based on nickel-iron structured electrocatalyst for OER. The amorphous electrocatalyst showed a low BET surface area along with low Tafel slope and low onset potential.

A diverse field of study along with oxygen deficiency, based on developing a layered structure that enhances water dissociation properties, thus, facilitating the hydrogen adsorption. Shao et al. [107] prepared a layered metal oxide for hydrogen evolution reaction given as Sr_2RuO_4 oxide. The electrocatalyst exhibited very low overpotential and low Tafel slope along with a high current density of 0.898 mA cm^{-2}. These properties of the layered catalyst are mainly due to water dissociation, which gets enhanced by cleave in the rock salt layer by strontium oxide terminated surface.

Properties of a catalyst are a strong function of its morphology. Nanostructured materials always enrich the catalyst with high catalytic properties. Shao et al. [108] worked on preparing a nanorod of oxygen-deficient perovskite-type oxide. The facile electrospinning method was used for the preparation of $SrNb_{0.1}Co_{0.7}Fe_{0.2}O_{3-\delta}$ perovskite nanorod, and found excellent electrochemical properties based on this catalyst. The tetragonal structured SNCF-NR exhibited a very small η of 0.39 V to approach 10 mA cm^{-2}. The catalyst break to nanorod like structure after its calcination, with an average diameter of 100 nm. It can be used for both OER and HERs with the output of a very high current density of 10 mA cm^{-2} at a cell voltage.

A different approach was used by Deganello et al. [109], who worked on preparing $La_{0.6}Sr_{0.4}Fe_{0.6}Mn_{0.4}O_{3-\delta}$ (LSFM) via soft-hard template method by using silica as a template, and developed a highly active catalyst of high surface area showing good performance for ORR (showing higher selectivity for 4 electron pathway) and OERs. The presence of amorphous metal silicate resulted in an increment in onset potential for ORR and Si below 4 wt% was recommended by the authors. Although, oxygen deficiency with

cation site Iron doping improves structure ability to catalyze a reaction, but along with this, the order of structure does influence a lot, which can be developed by a suitable technique as mentioned by Zhou and Shao[47], worked on improving the catalytic activity of iron-based perovskite by deficiency tuning and designing the crystal structure. The 3D macroporous structure building of $LaFeO_3$(LF) in combination with bulk doping is responsible for stability and high catalytic activity. The results obtained for 20% doping of cobalt has really made 3DOM-LFC82 a stable, active with largest MA (44 A g_{ox}^{-1}) and life lasting catalyst during the HER. Table 1. Given below shows the HER activity for some perovskite catalysts.

Table 1: *Electrochemical properties of Perovskites based on HER.*

Ref #	Catalyst	Group	Preparation	Characteristics BET surface area m^2/g	Tafel slope mV dec^{-1}	Onset Potential V
[47]	$LaFeO_3$ (LF) 3DOM-LF 3DOM-LFC82 $LaFe_{0.8}Co_{0.2}O_3$(LFC82)	B-site Co doped perovskite	Colloidal crystal template method	8 20 16 6	140 123 111 113	-0.37 -0.3 -0.25 -0.34
[107]	A layered Ruddlesden−Popper (RP)-type oxide Sr_2RuO_4 RuO_2 $SrRuO_3$	Oxygen deficient perovskite	Solid-state reaction route	1.4	51 49 67	0.003 0.046 0.028
[79]	Ex-LSTN LSTN LST LST/Ni bulk	A-site Sr and B-site Ni doped oxygen deficient perovskite	Insitu exsolution of perovskite	N.A.	97 276 313 139	-0.27
[110]	P-3G	Perovskite composite		N.A.	45	-0.22
[94]	$Sr_{0.95}Co_{0.8}Nb_{0.1}Ni_{0.1}O_{3-\delta}$ $Sr_{0.95}Co_{0.7}Nb_{0.1}Ni_{0.2}O_{3-\delta}$	A-site cation deficient and B-site doped oxygen deficient	Non-aqueous sol-gel method	N.A.	64 80	N.A.

		perovskite				
[111]	PBC-900	B-site doped	Sol-gel method	N.A.	183.1	-0.37
	PBC-1000	perovskite			128.2	-0.35
	PBC-1100				120.1	-0.24
	PBC-1150				89	-0.3

2.2.1 Cation ordered double perovskite

The reason of existence of the O-p band center at a certain distance from the fermi level, is to create a special layered structure, responsible for significant activity and stability of perovskites. Grimaud et al. [112] worked on double perovskites, considering $LnBaCo_2O_{5+\delta}$ (Ln = Pr, Sm, Gd, and Ho) and found $PrBaCo_2O_{5+\delta}$ (PBC) to be the most active and stable OER catalyst, while, Sun et al. [111] presented $PrBaCo_2O_{5.5}$ orthorhombic perovskite highly active for HER, shown in Table 3. Most recently Shao et al. [113] worked in a similar area, where, multi-active sites are introduced in order to develop the optimal binding for intermediates following the shortest reaction path. The study focused on creating a double perovskite $Sr_2Fe_{0.8}Co_{0.2}Mo_{0.65}Ni_{0.35}O_{6-\delta}$ with multi-active sites to enhance OER performance of electrocatalyst. Sun et al. [91] reported a double perovskite with B-site molybdenum and niobium co-doping, having a compositional formula of $Ba_2CoMo_{0.5}Nb_{0.5}O_{6-\delta}$ (BCMN) and $Ba_2Co_{1.5}Mo_{0.25}Nb_{0.25}O_{6-\delta}$ (BC1.5 MN)[114] as a highly efficient OER and ORR catalyst. The later has shown low overpotential of 40 $mVcm^{-2}$ and 3.5 times higher mass activity as compared to BCMN. Another B-site doped perovskite $Ba_2Bi_{0.1}Sc_{0.2}Co_{1.7}O_{6-\delta}$ (BBSC) was synthesized via the sol-gel method, with the property of ordered dual-site cobalt which has shown extremely good performance in durability test in comparison with BSCF and PBC electrocatalysts. The B-site ordering has played a significant role in enhancing the OER activity as at the η=0.5V, lower specific activity for disorderly arranged $Ba_{0.5}Sr_{0.5}Co_{0.8}Fe_{0.2}O_{3-\delta}$ (BSCF) and $Ba_2Bi_{0.1}Sc_{0.2}Co_{1.7}O_{6-\delta}$ (BBSC) catalysts. Basically, the enhanced activity is attributed to the ordering of Co^{+2} and Co^{+3} ions and the presence of these two valence ions in a mixed manner[115].

As mentioned earlier, that perovskite composite with reduced graphene oxide has undergone very high catalytic results that would be enhanced by creating oxygen vacancies. Kim et al. [116] presented substantial work on perovskite oxides by creating

triple perovskites and showed that $Nd_{1.5}Ba_{1.5}CoFeMnO_{9-\delta}$ (NBCFM) has a higher activity for OER and ORRs. However, the catalytic activity was enhanced by nitrogen-doped-reduced graphene oxide, as it is having 4 electron transfer numbers. The major reason behind the higher catalytic activity of NBCFM is a nonstoichiometric ratio of oxygen and electronic configuration. As the triple perovskite-type oxide produces large vacancies for oxygen, which were created due to structural distortion caused by continual stacking[116]. Wang et al. [117] studied the HER activity of a series of H_2-reduction-treated $NdBaMn_2O_{6-\delta}$ double perovskites with various oxygen vacancy contents (δ = 0.35, 0.54, and 0.80). The best activity was shown by $\delta = 0.54$ which was considered to be the results of number of factors, including distorted structure, near-unity e_g occupancy and O-p band centre. Therefore, oxygen deficient perovskites should be developed cautiously.

2.3 Nanostructured Perovskites

The bulk perovskites have large size but small surface area, and thus, have limited catalytic ability. Developing the catalyst at the nano-scale not only presents a diversely active compound with high phase purity, but also strengthens its structural properties providing the more active sites. Perovskite with La as an A-site element has excessively been a topic of research. Many different catalytic properties have been achieved by just changing the B-site transition earth metal. Hardin et al. [118] prepared $LaNiO_3$ nanocrystals, that exhibited extremely high activity results for OER and ORRs due to their high phase purity, high BET surface area and introduction of a hydroxyl group in a lattice structure. The activity for ns$LaNiO_3$/NC (Nitrogen-doped Caron) (89 mA/mg_{oxide}) reached 2.5 times that of a leading benchmark catalyst, 6 nm IrO_2 (36 mA/mg_{oxide}). During the reverse phase growth precipitation, hydrolysis of La^{3+} and Ni^{2+} nitrate takes place that results in the development of the highly active structure of the catalyst. Perovskite structural properties were also enhanced by taking Co as B-site element, forming an amorphous surface via hydrothermal process proposed by Kim et al. [119], focuses on developing porous nanostructures and hollow spheres of $LaCoO_3$. The morphology of the perovskite-type oxide along with the examination of electrochemical properties were evaluated. A rhombohedral unit cell structure was found with truncation

at specific corners, that can be the result of a diverse molar ratio between metal precursor and organic molecules.

2.4 Perovskite on material support

Supporting the catalyst on some material imparts specific properties related to support and significantly influences the catalytic performance, based on either increasing the charge transfer, exposing the active sites, enabling the high interaction to an electrolyte, providing the short conduction path for oxygen absorption and improvement in structural stability. Perovskite can be supported on many types of materials depending upon the property desired.

Singh et al. [120] worked on a thin film of cobalt oxide type perovskites supported on the conductive material and prepared thin film catalyst $La_{1-x}Sr_xCoO_3$ (x = 0, 0.2, and 0.4) by two different methods, named as maleic acid aided method and nitrate decomposition method. The grains obtained in oxide by the second method are larger than the prior one. The new method has produced a reduction in the oxygen overpotential of -175, -130, and -75 mV for $LaCoO_3$, $La_{0.8}Sr_{0.2}CoO_3$, and $La_{0.6}Sr_{0.4}CoO_3$ respectively, at 10 mA cm^{-2} in 1M KOH at 25^oC.

Carbon can also be used as a support in different forms, thus directly influencing the catalytic activity of electrocatalyst. Yuasa et al. [121] reported a distinctive work on $La_{1-x}Ca_xMn_{1-y}Fe_yO_3$ nanoparticles supported on carbon. The reverse miscella method with $KmnO_4$ for high Mn valency was chosen as a method for preparing this carbon supported catalyst. Oxygen reduction capacity was found to be enhanced by doping Ca in the range of 0.4-0.8 that made it comparable to the Pt/C catalyst. Resulting carbon to be better support material for perovskite, Chang et al. [122] developed carbon nano-capsules (CNCs) as a base for perovskites and reported on Ir doped $La_{0.6}Ca_{0.4}CoO_3$ perovskites. It is further concluded that the perovskite prepared by the solid-state reaction is of an irregular shape having a size between 100 and 250 nm. The $La_{0.6}Ca_{0.4}Co_{0.8}Ir_{0.2}O_3$/CNCs catalyzed GDE showed high catalytic performance, exhibiting a charging voltage of 2.39 V at a current density of 150 mA/cm^2.The prepared iridium doped lanthanum cobalt perovskite-type catalyst is having a smaller surface area than $La_{0.6}Ca_{0.4}CoO_3$, and Ir^{4+} doping showed high bifunctional catalytic activity.

Another type of sustenance, that favors fast oxygen reduction can be of oxophilic nature resulting in enhanced oxygen adsorption. Park et al. [123] reported using Ag, that significantly increases the water activation on LMO and, thus, enhancing the ORR activity. The catalytic activity is strongly dependent on oxophilixcity and has shown the order ($Ag/LaCoO_3$ < $Ag/LaFeO_3$ < $Ag/LaMnO_3$), as it promotes the water activation, thus, promoting the ORR. The adsorption of oxygen species is enhanced by charge transfer from Mn to Ag and increased oxophilic nature of Mn sites. Thus, it is suggested that the support used, must be of highly oxophilic nature to reduce interference between catalyst and support[123].

2.5 Perovskite composites

There is a new dimension of achieving high catalytic properties by developing a hybrid of perovskite with some material of equal importance. Considering noble metal nanoparticles to develop the composite, enhances the current density and lowers the overpotential. Soares et al. [124] presented a new idea of preparing composites of $PtRu/C\text{-}LaNiO_3$. The presence of Pt-Ru nanoparticles has significantly enhanced the electrocatalytic activity of the composite on Ni foam support. The elemental distribution map showed that the nanoparticles were uniformly distributed over the electrode. The oxygen produced in anodic sweep reduces, thus, producing a cathodic peak at E= -200 mV. The well-defined redox peaks were observed, followed by an increment in current value at a potential higher than 600 mV. The changes in Voltammetric curves were obtained, that indicated the increased catalytic activity under OER after running for 50, that can be attributed to increased surface roughness. Thus, the access of electrolyte towards active site get increased.

A different approach of preparing a composite with Pt was reported by Han et al. [125], who synthesized Pt clusters supported on porous perovskite-type oxide such as $CaMnO_3$. Beside noble metals, 2-D materials have also been considered as an active catalyst. In order to reduce the charge transfer resistance and attain long term stability, Thanh and Chong[126] presented a new porous and hollow structured nanohybrid $LaNiO_3$ co-doped graphene ($LaNiO_3$-N-S-Gr. A similar type of work was done by G Kim [110], who published his work on 3D porous nitrogen-doped graphene with a ($PrBa_{0.5}Sr_{0.5}$

$)_{0.95}Co_{1.5}Fe_{0.5}O_{5+\delta}$ (PBSCF) perovskite termed as P-3G. The composite showed the highly promising results for HER, OER and ORRs. The DFT calculations have revealed that the higher activity for water splitting reactions is due to electron transfer to $л^*$ orbital of O_2 gas, which is favored by PBSCF. Thus, very low Tafel slope and high current density values are obtained by 3DNG-PBSCF composite, which exhibits a broad future of P-3G for energy applications.

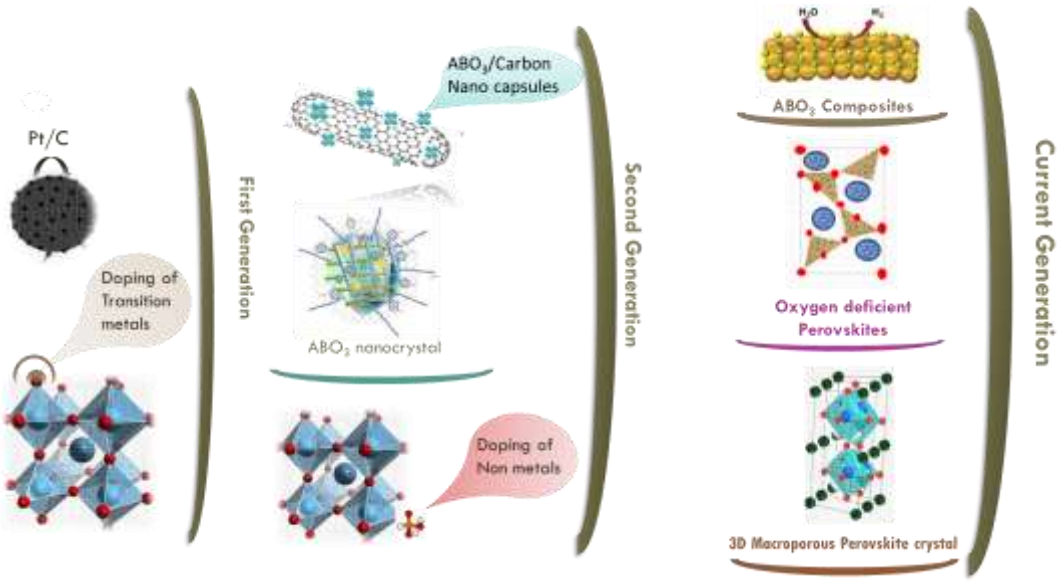

Figure 6: *Progressive developments in perovskite type catalyst for HER/OER and ORRs.*

The intrinsic increment in the activity of each reactive site can be done by accounting the physicochemical properties of perovskite electronic structures. These properties include a range of composition achieved by substitution, oxygen vacancy and diverse crystal structures. The other is to extrinsically increase the activity and number of reactive sites which is a function of geometric effect. This can be achieved by proposing novel methods for the synthesis of perovskite nanostructures and its composites. These parameters are interrelated, changing the composition could directly alter the oxygen vacancy as well as crystal structure.

In this work, it has been tried to develop bifunctional electrocatalyst, which is cost effective as well as highly stable. Three types of composites have been prepared by

preparing a composite and doping method. The extensive literature review has been done on various type perovskite oxides as well as their composite. Then, the A/B site doped perovskite composited with 2D material MXene, and layered double hydroxide have been prepared to increase their activity and make them compareable to state-of-the-art catalyst. Moreover, B-site doped double perovskite has also been prepared and characterized to explore their importance in practical application for hydrogen production.

Chapter No 3

Materials and methods

3.1 Materials

The material purchased for preparation of LSTN@NiMn-LDH consist of nickel (II) nitrate hexahydrate ($Ni(NO_3)_2.6H_2O$), urea (CH_4N_2O), thiourea (C_2H_5NO), lanthanum nitrate hexahydrate ($La(NO_3)_2.6H_2O$), strontium nitrate ($Sr(NO_3)_2$, titanium n-butoxide ($C_{16}H_{36}O_4Ti$), EDTA-2Na dihydrate ($C_{10}H_{14}O_8N_2Na_2.2H_20$), manganese nitrate tetrahydrate ($Mn(NO_3)_2.4H_2O$, MAX phase Ti_3AlC_2, hydrofluoric acid, ethanol (97% wt.%), sodium hydroxide, and citric acid ($C_6H_8O_7$). All materials were purchased from Sigma Aldrich USA.

3.2 Synthesis of LSTN perovskite

The sol-gel method was adopted for $La_{0.4}Sr_{0.4}Ti_{0.9}Ni_{0.1}O_{3-\delta}$ nanopowder preparation followed by high-temperature calcination. The catalyst was prepared by dissolving 0.016 moles of lanthanum nitrate hexahydrate, 0.016 moles of strontium nitrate and 0.0045 moles of nickel nitrate hexahydrate in 50 ml DI water. 0.045 moles of titanium (IV) n-butaoxide were added dropwise with continuous stirring in the above solution. Then a combination of EDTA-2Na dihydrate ($C_{10}H_{14}O_8N_2Na_2.2H_2O$) and anhydrous Citric acid ($C_6H_8O_7$) was added with continuous stirring in a molar ratio of 1:2, which served as complexing agents. Strong base (1 M KOH) was added to maintain PH of the solution. The solution was then heated on a hot plate at 150^oC till a transparent gel appeared. The gel was then uniformly heated at 250 ^oC for 12 hrs to remove organic compounds, followed by calcination at 900 ^oC for 8 hrs.

3.3 Synthesis of e-LSTN electrode

The exsolution of Ni in LSTN has been done by reducing LSTN perovskite particles in 10% H_2/Ar environment at 900 ^oC for 10 hrs to obtain Ni nanoparticles/$La_{0.4}Sr_{0.4}Ti_{0.9}O_{3-\delta}$. The ink was prepared by adding 10mg e-LSTN in a mixture of 500µL DI water, 450µL

isopropanol, and 50µL Nafion followed by 45 min sonication in a sonication bath. The prepared ink of powdered LSTN was deposited on dried Ni foam till a mass loading around 2-3 mg cm^{-2} was achieved. After deposition, Ni foam was dried and weighed.

3.4 Synthesis of bifunctional LSTN@NiMn-LDH electrode

A highly economical and simple hydrothermal method was used to develop NiMn-LDH nanosheets on perovskite coated Ni foam (NF) substrate. Firstly, the NF substrate was cleaned by sonication with acetone, 2M HCL, distilled water, and lastly by absolute ethanol respectively, individually for 15 min. The drying of Ni foam was carried out at 60 ºC in drying oven for 2 hrs. The prepared ink of powdered LSTN was deposited on dried Ni foam till a mass loading around 2-3 mg cm^{-2} was achieved. The ink was prepared by adding 10 mg of prepared LSTN in a mixture of 500µL DI water, 450µL isopropanol, and 50µL Nafion followed by 45 min sonication in a sonication bath. After deposition, Ni foam was dried and weighed. For Ni-Mn LDH growth, a solution was prepared by adding 0.7mmol of nickel (II) nitrate hexahydrate, 0.35mmol manganese nitrate tetrahydrate, 0.063g urea and 0.08 g thiourea in 40 ml DI water and 30 ml ethanol. The precursor along with the dried LSTN deposited Ni foam was poured to a Teflon vessel, which is encased in stainless steel autoclave. The vessel was maintained at 90 ºC for 4 hrs. followed by 110 ºC for 9 hrs. After the hydrothermal reaction, NiMn-LDH grown substrates were rinsed using DI water along with absolute ethanol three times, which is followed by drying of composite for 2 hrs at 60 ºC. **Fig. 7** shows the synthesis method of NiMn-LDH over LSTN nanoparticles.

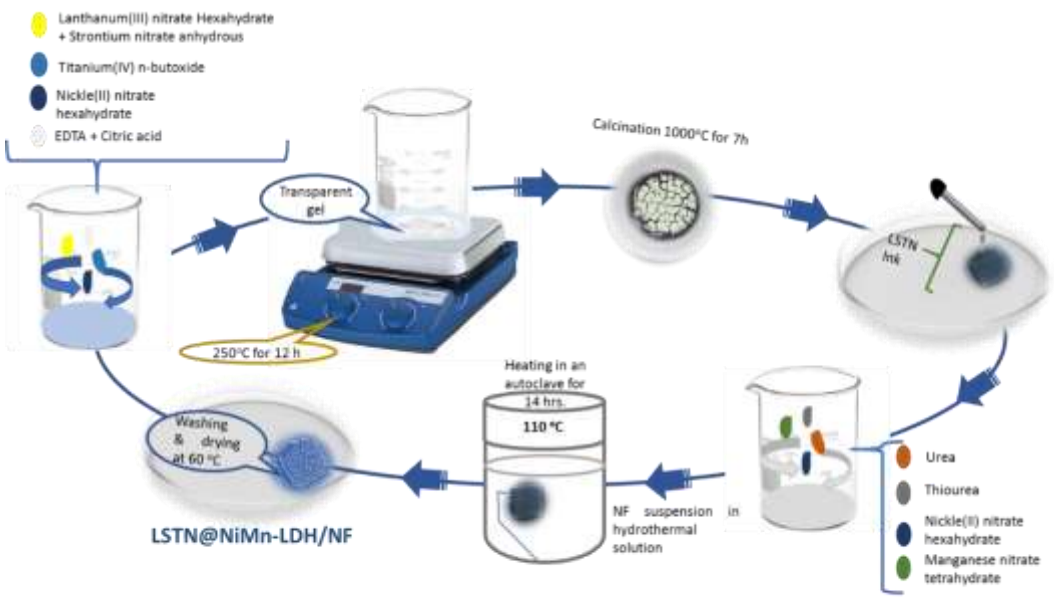

Figure 7:*Schematic of experimental procedure for LSTN@NiMn-LDH preparation.*

3.5 Synthesis of LSTN perovskite and MXene

The synthesis of $La_{0.4}Sr_{0.4}Ti_{0.9}Ni_{0.1}O_{3-\delta}$ nanopowder was done by using sol-gel method, the powder was calcined at high temperature to remove all impurities. 16 mM of $La(NO_3)_2.6H_2O$ and $Sr(NO_3)_2$ are dissolved in 50 ml DI water along with the continuous addition of 45 mM of $Ni(NO_3)_2.6H_2O$ in the same mixture. $C_{16}H_{36}O_4Ti$ (0.045 moles) was added dropwise in the above solution with continuous stirring to make it homogeneous. A combined mixture of EDTA-2Na dihydrate and anhydrous citric acid, which are used as a complexing agent, was added with continuous stirring in a molar ratio of 1:2. In order to maintain the PH of the solution, a strong base (1 M KOH) was added. The prepared solution was then placed on a hot plate, where it was heated at 150^{o}C a transparent gel appeared. The gel was then uniformly heated at 250 ^{o}C for 12 hrs. to remove organic compounds, followed by calcination at 900 ^{o}C for 8 hrs.

The 2 g MXene was synthesized by using hydrofluoric acid. 12 ml of 40% HF was added in 7.98 ml of deionized water. The MAX phase was added subsequently in the above solution and it was placed on a hotplate at 35 ^{o}C, with continuous stirring for 8 hrs.

The solution was then diluted to lower the PH, which was followed by the settling of MXene overnight. Then, the washing of the MXene solution was done by centrifugation at 4000 rpm for 3 h., till the PH gets closer to 6. The MXene was then dried in a vacuum oven at 80 ^{o}C overnight.

3.5.1 **Synthesis of LSTN/MXene composite**

The electrode was synthesized by co-precipitation of LSTN powder with MXene nanosheets in three ratios (1:1, 1:2 & 2:1) which are given the names as LSTN/MXene 50%, LSTN/MXene 66.67%, and LSTN/MXene 33.33%, respectively. Firstly, the MXene solution was prepared by sonicating it in deionized water for 20 min. While, Sr and Ni-doped $La_{0.4}Sr_{0.4}Ti_{0.9}Ni_{0.1}O_{3-\&}$ (LSTN) nanoparticles were added into the solution of ethylene glycol and acetic acid, added in 1:1 with a molarity of 0.01M. This solution was sonicated for 1 h at 60^{o}C. Then, both solutions were mixed and sonicated for 1 h. The prepared solution was then rinsed with deionized water three times, followed by drying at 50^{o}C for 24 hrs. The schematic of synthesis of LSTN/MXene composite is given below in **Fig. 8**.

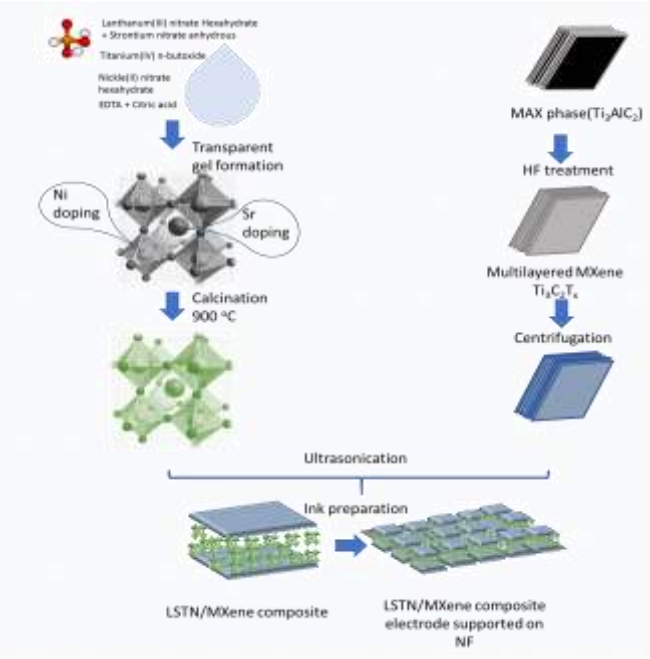

Figure 8: *Schematic illustration of synthesis method of LSTN/MXene composite.*

Table 2: *Characterization for nano transition metal oxide composites.*

Catalyst	XRD	FTIR	Raman	SEM	TEM	EDS
LSTN@NiMnLDH	▪	▪	▪	▪	-----	▪
LSTN/MXene 50%	▪	-----	▪	▪	-----	-----
LSTN/MXene 66.67%	▪	-----	▪	▪	▪	▪
LSTN 66.67%/MXene	▪	-----	▪	▪	----	----
STF	▪	----	----	----	▪	----
STPF-0.1	▪	----	----	----	▪	----
STPF-0.2	▪	----	----	----	▪	▪
LSTN	▪	----	▪	▪	----	----
MXene	▪	----	▪	▪	----	----
NiMn-LDH	▪	----	▪	▪	----	----

3.6 Characterization Techniques

3.6.1 X-ray Diffraction (XRD)

The X-ray Diffraction of STOE-Germany was used to evaluate the crystalline nature of LSTN, LSTN@NiMn-LDH composite, LSTN/MXene composites, and MXene layered structure. The voltage of 40 kV was applied accompanied with current of 40 mA. The scanning of sample was done at a step size of 0.04 and a step time of 0.5s/step was provided. The scan angle was ranged from 2θ (10° to 80°). The wavelength of CuKα radiation was 1.540 Å.

The following Debye-Scherrer Equation was used to find out the average crystallite size.

$$\tau = \frac{0.9\pi}{\beta Cos\theta} cos\theta$$

τ represents average crystallite size,

λ stands for wavelength of X-rays,

β is the full width at half maximum,

θ shows the Braggs angle

X-ray diffraction is used to analyze the atomic spacing and crystal structure.

3.6.1.1 Objectives of XRD

The objectives of XRD are

I. It identifies of crystallinity of material

II. It is used to distinguish between crystalline and amorphous forms

III. To calculate the lattice spacing of material.

IV. To find out average particle size.

3.6.1.2 Working Principle

The XRD works on constructive interference between monochromatic X-rays. Cathode ray tube produce X-rays which are then filtered to generate monochromatic radiations. To focus the rays towards specimen, these rays are concentrated by collimation. The interaction between these rays and specimen results constructive interference, which satisfy Bragg's Law. Bragg's Law states the direct relation of wavelength of the electromagnetic radiations with lattice spacing and diffraction angle of the specimen. It can be written as

$$n\lambda = 2d\ sin\theta$$

Where,

n is order of reflection,

λ represents wavelength of X-rays,

d is the characteristic spacing between crystal planes of a given specimen

θ is the angle formed between incident beam and that normal to the lattice plane

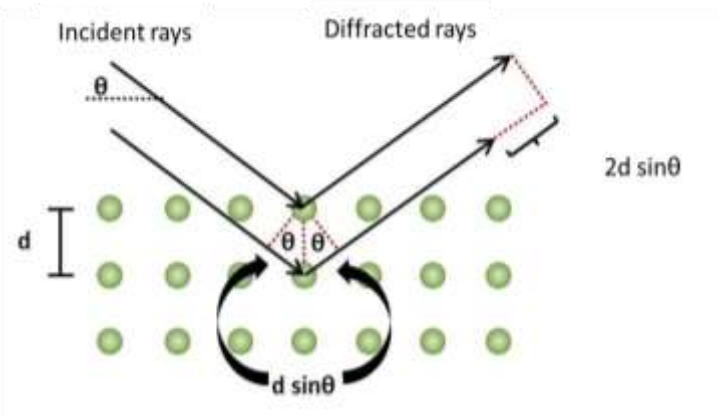

Figure 9: *Schematic Diagram of Bragg's Law*[115]

3.6.2 Fourier Transform Infrared Spectroscopy (FTIR)

FTIR was used to study the interfacial interactions among two phases employing formation of composite. The following machine Fourier Transform Infrared Spectroscopy (ATR-FTIR, BRUKER) was used for analysis. The analysis was carried out in the range of 4000-500 cm^{-1} at resolution of 4 cm^{-1} and applying a scanning frequency of 32.

3.6.2.1 Objectives of FTIR

The objective of FITR is to

I. Recognize organic, polymeric or sometimes inorganic compounds

II. Characterization of unknown materials

III. Identification of contaminations (in or on the materials)

IV. In failure analysis, identify decomposition, oxidation or uncured substances

3.6.2.2 Working Principle

The FTIR works on absorbance of light by molecules, while they are in infrared region of the electromagnetic region. The absorption of light uniquely implies to the bonds present

in the molecules. The infrared region lies within range of 12800 to 10 cm^{-1}, which is further divided into near, mid and far infrared regions[127].

Table 3: *Frequency Range of different IR Regions.*

Infrared region	Range of frequency (cm^{-1})
Near IR	12800-4000
Mid IR	4000-200
Far IR	1000-50

Infrared absorption spectrum mechanism is based on vibrations of molecules. When the specimen is exposed to radiations, its molecules absorb radiations of certain wavelength. This changes the dipole movement of specimen molecules. As a result, the energy level of the specimen molecule is transfer to excited state from the ground state. The energy gap determines the frequency of absorption peak. The change in intensity is subjected to the dipole moments and shift of energy levels.

3.6.2.3 Components of FTIR

The basic components of FTIR are

1. Source

2. Interferometer

3. Sample compartment

4. Detector

5. Amplifier

6. A/D Converter

7. Computer

The radiations are generated by the source. These radiations after passing through the interferometer reaches the specimen and are recognized by the detector. The signals are amplified by means of amplifier, are converted to digital signals by analog-to-digital converter. Finally, signal is transferred to a computer where Fourier Transformation is carried out.

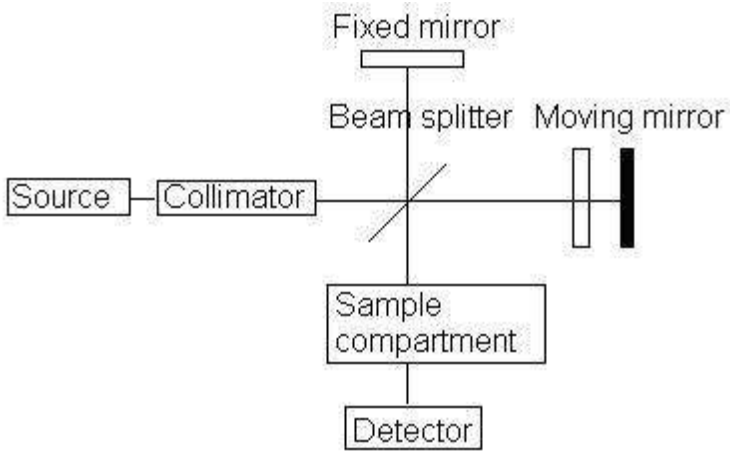

Figure 10: *Components of FTIR* [117]

3.6.3 Raman spectroscopy

It is a molecular spectroscopic technique that uses light to interact with specimen and give characteristic information. It works by scattering of light rather than absorption of light like FTIR, to get an insight to the spectrum characteristic of specific vibrations of a molecule. It also provides information about lower frequency modes and vibrations, which are very useful to det brief understanding of crystal lattice and basis of molecular structure.

3.6.3.1 Working Principle

The light interacts with the molecules available in gas, liquid or, solid, the photons within incoming light get dispersed with same energy as that of incident photons, thereby undergoing elastic scattering. Only a small number among them undergo inelastic

scattering. Raman helps user to capture vibrational characteristic signature of molecule, that develops an understanding of how they are put together as well as their method of interaction with other molecules around it.

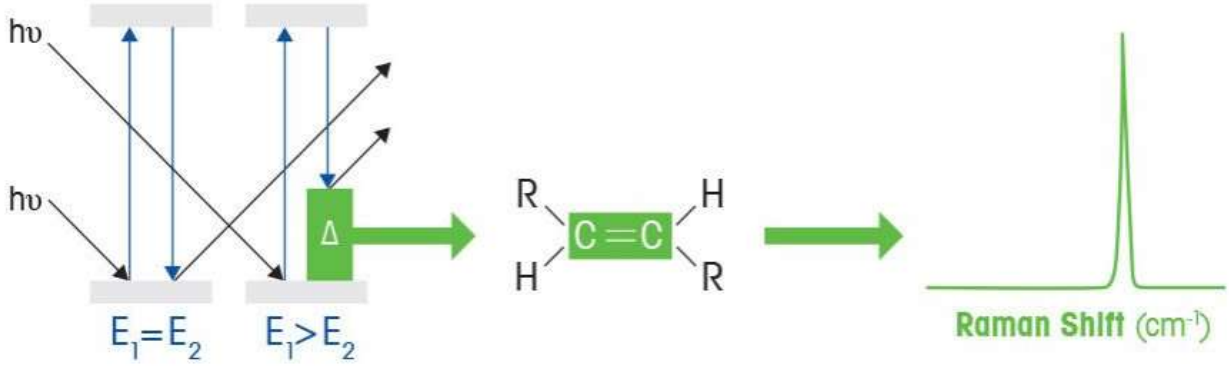

Figure 11: *Schematic illustration Raman spectroscopy principle* [115]

3.6.4 Scanning Electron Microscopy (SEM)

The morphology of perovskites and its composites were recognized by SEM (JSM-64900). Prior to analysis, powder of material was placed on stud and gold plated to provide a conductive layer.

3.6.4.1 Objective of SEM

SEM is an outstanding technique for observing the surface of material and provides excruciate details about surface projections. It provides information about

I. Texture (External Morphology)

II. Chemical composition

III. Orientation

IV. Crystalline Structure

3.6.4.2 Working Principle

It uses an electron beam to generate the image of a material and the magnifications are obtained by means of electromagnetic fields.

3.6.4.3 Components of SEM

The components of SEM include

1. Electron source

2. Condenser lens

3. Scan coils

4. Objective lens

5. Secondary electron detector

At the top of the column the electrons are generated by the electron source. A beam of electrons is produced. When their thermal energy exceeds the work function of the source, the electrons are emitted. These electrons then get accelerated and are attracted by the anode (positively charged). The diameter of electron beam is adjusted by means of lens. If it is weakened, a broader beam is produced and vice versa. The path of electrons is also controlled by the lens. Electromagnetic lens is utilized owing to the fact that electrons couldn't pass through the glass. Firstly, the electrons meet the condenser lens. After converging by condenser lens, the electrons are further condensed by the objective lens[128].

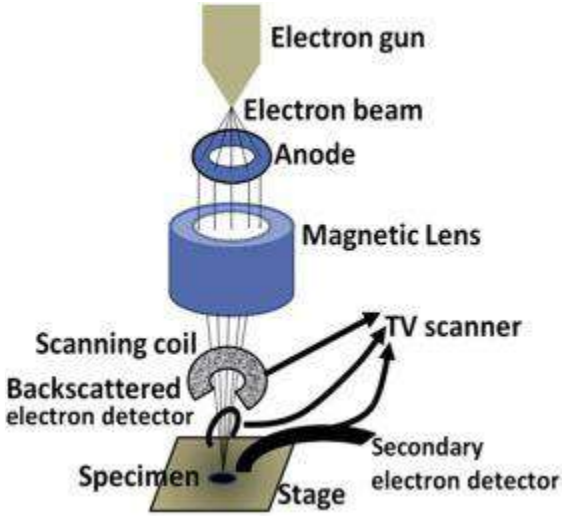

Figure 12: *Components of SEM.*

3.6.5 Transmission electron microscopy (TEM)

The Transmission electron microscope uses an electron gun that utilizes electron beam to display he image of specimen. It is having high magnification power approx. 2 million times as compared to light microscope.

3.6.5.1 Working Principle

The working principle is similar to light microscope, except it uses a beam of electron to focus rather than light. As electron exhibit shorter wave length and thus an increase in resolution power occur when electron illuminates, which increases the electron transmission. It has three major working units.

1. Electron gun.

2. Image producing unit.

3. Image recording unit.

3.6.6 Energy dispersive X-ray spectroscopy (EDS)

Energy dispersive x-ray spectroscopy is a prevailing technique that is used to analyze the elemental composition of sample. It majorly works on capacity of x-rays to emit core electrons from an atom. This process is known as Moseley's Law, which shows that as the frequency of light released increases, the atomic number of atom also increases. When the electron leaves the system, a hole will be created. This hole gets occupied by a higher energy electron, which releases energy as it gets relaxed[128]. The energy released is characteristic to each element in periodic table, which can be used to identify element as well as their proportion. It consists of three major parts.

1. Emitter

2. Collector

3. analyzer

These parts are connected to SEM, or TEM. Combining three pieces gives information about ho may x-rays are released and energy associated with it.

3.7 Electrochemical characterization

The as-synthesized electrodes were analyzed by X-ray diffraction (STOE-Seifert X'Pert PRO), using 2θ values from 20º to 80º using Cu-Kα radiation. Scanning electron microscopy (JEOL-instrument JSM-6490A) equipped with an EDX and transmission electron microscopy ((TEM, JEM 2100 LaB6, Tokyo, Japan) was used to investigate the morphology of the electrode materials. The electrochemical tests for OER and HER were carried out with three-electrode assembly. The working electrode was nickel foam-based electrodes while the reference and counter electrode were consisting of Ag/AgCl and Pt mesh (1x1), respectively. For the preparation of working electrode, the Ni foam substrate was cleaned by sonication with acetone, 2M HCL, distilled water, and lastly by absolute ethanol respectively, individually for 15 min. The drying of Ni foam was carried out at 60 ºC in drying oven for 2 hrs. To prepare the electrode ink of LSTN/MXene, 10 mg of

composite powder were added in 500 µl DI water, 450 µl isopropanol and 50 µl Nafion. The ink was then sonicated for 30 min in sonication bath and was loaded on cleaned Ni foam to achieve a mass loading of 2-3 mg cm^{-2}. After deposition, Ni foam was dried overnight at 80 ºC. The catalytic activities of all electrodes have been analyzed in 1 M KOH solution using a three-electrode assembly at 10 mVs^{-1}, 20 mV s^{-1}, 30 mV s^{-1}, 40 mV s^{-1}, and 50 mV s^{-1}. For simplicity, reversible hydrogen electrode potential was used for further calculations, which was obtained by the following equation; $E_{RHE} = E_{Ag/AgCl} + 0.059pH + 0.1976$, with PH = 14. In addition, electrochemical impedance spectroscopy was performed at a frequency range of 200kHz-100mHz, by providing a 10 mV alternating voltage amplitude. The stability of as-prepared electrocatalyst was analyzed by chronopotentiometry measurements. The cyclic voltammetry tests were also performed at voltage range of 0-0.6 V, at diverse scan rate range of 10 mVs^{-1}, 20 mV s^{-1}, 30 mV s^{-1}, 40 mV s^{-1}, and 50 mV s^{-1}.

Table 4: *Electrochemical characterization of catalysts.*

Catalyst	LSV	CV	EIS	Chronopotentiometry
LSTN@NiMnLDH	▪	▪	▪	▪
LSTN/MXene 50%	▪	▪	▪	-----
LSTN/MXene 66.67%	▪	▪	▪	▪
LSTN 66.67%/MXene	▪	----	▪	▪
STF	▪	----	▪	-----
STPF-0.1	▪	----	▪	-----
STPF-0.2	▪	▪	▪	-----
LSTN	▪	▪	▪	----
MXene	▪	▪	▪	----

NiMn-LDH	▪	▪	▪	----

3.7.1 Linear sweep voltammetry

The Linear sweep voltammetry technique comprises of a fixed potential range, which is applied in a similar way as potential step measurement. The voltage scanning is performed from lower to upper limit as given below.

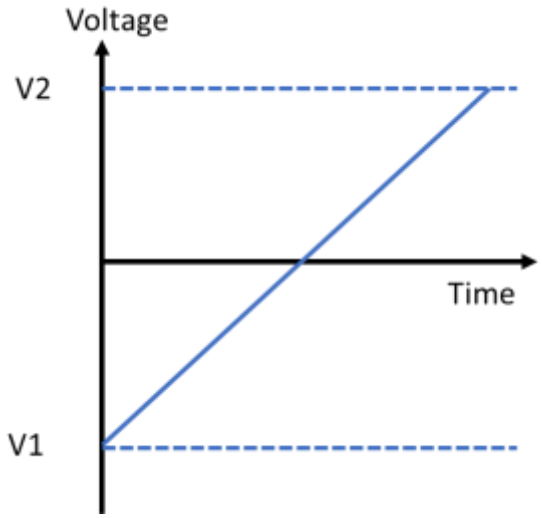

Figure 13: *Schematic representation of LSV..*

The scan rate can be calculated from slope of the line. It depends on time required to sweep the voltage range. The characteristics of LSV curve depends on many factors.

1. Reaction rate required to transfer an electron

2. The chemical reactivity of species that are electroactive

3. The voltage scan rate

The response of current is plotted against voltage.

3.7.1.1 Tafel slope

The purpose of Tafel slope is to understand the Tafel behaviour among electrocatalysts and reactants. The Tafel equation can be transformed to log functions, where a low Tafel slope indicates efficient kinetics of electro catalyst which corresponds to smaller overpotential with quick increase in current density. Tafel slope also provides an insight to OER mechanism, pointing out to the rate determining step. the intrinsic rate of electron transfer among electrode and analyte can be directly reflected by exchange current density($j_\circ$). however, the complex OER mechanism and extensive errors associated with exchange current density estimation j_0 is rarely used in OER and HER

$$\eta = b.\log\frac{j}{j_.}$$

where η is overpotential b is Tafel slope j is current density and j. is exchange current density.

3.7.1.2 Overpotential

For the purpose of formation of reaction intermediates with efficacy overpotential is applied to propel the processes of electron transfer at a desired rate that has been subjected to inactivity because of the high activation energies[26]. Under the conditions that, water is at 25°C and pH = 0 then according to Nernst equation, (E_{eq}= NHE = RT/NF = $\ln\frac{Ox}{Red}$) where,

E_{eq}= potential under equilibrium conditions R= ideal gas constant T= temperature in Kelvin n= number of moles of electrons F= Faraday Constant [Red]= concentration of reduced molecules [Ox]=concentration of oxidized molecules.

The required potential for electrolization of water will be E_{eq} = 1.23V vs. NHE.

With the change of pH, the electrode potential changes, which in turn utilizes reversible hydrogen electrode (RHE) as a reference potential at a given temperature of 25°C.

E_{eq} (RHE) = E_{eq} (RHE) +0.059 pH =1.23V

The cell potential given as E is

$E(RHE)=E_{Test}+E^{o}+0.059$ pH, Where E_{RHE}=converted cell potential

E_{Test} = applied cell potential

E^o = cell potential at standard conditions

For different overpotential values there will be different current values accordingly. The overpotential value was commonly used as criterion at a current density of J=10 mA cm^{-2} (η_{10}). The smaller the value of η_{10} more improved will be the electrolytic ability.

$\eta = E(RHE) - E_{eq}(RHE)$

3.7.2 Cyclic voltammetry (CV)

Cyclic voltammetry testing is shares very common features to LSV in this process the voltage is changed between two values at a fixed rate and when voltage reaches the value V_2, reverse scanning is performed and is taken back to V_1. The **Fig. 14** shows a cyclic voltammogram performed for a reversible single electrode. When the voltage increases from V_1 toV_2 the response is similar to LSV. Reversal of scan shifts the curve from equilibrium position resulting in oxidation. In this case the current flows from electrolyte solution towards the electrode. When electrochemical reaction is performed reversibly the CV has certain characteristics.

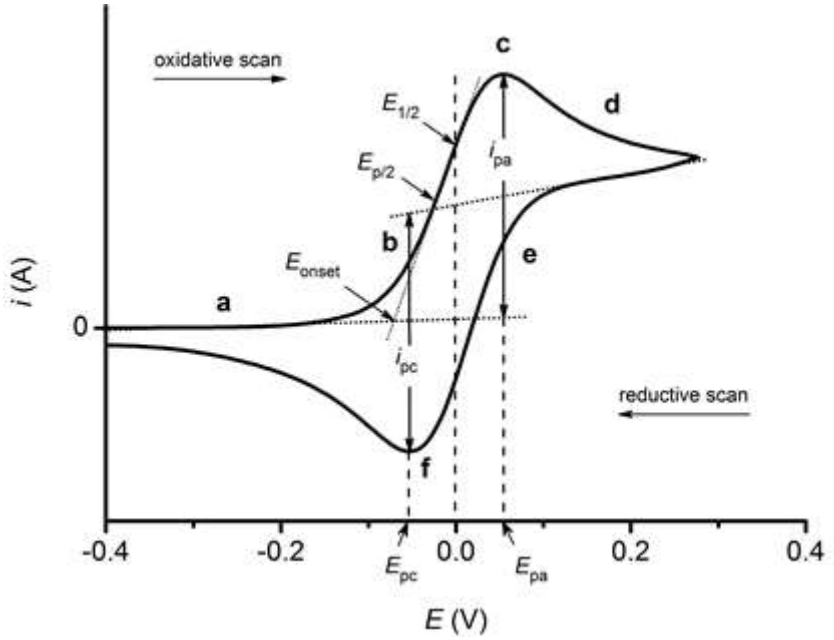

Figure 14: *Cyclic voltammetry curve illustration*[129]

1. The current peaks separate by voltage of $\Delta E = E_P^a - E_P^c$
2. The peak voltage position remains the same as scan rate changes.
3. The ratio of the peak current gives the value of one

   $\frac{|i_p^a|}{|i_p^c|}$ =1
4. The peak currents are proportional to the square root of the scan rate.

3.7.3 Electrochemical Impedance Spectroscopy (EIS)

Electrochemical impedance spectroscopy is used to measure resistance and capacitance properties of catalyst, when an AC excitation signal is applied at 10 mV. The resistance and capacitance values are calculated by measuring in-phase and out-phase responses of current. It also provides an insight to electrochemical reactions occurring at anode and cathode. Internal resistance is measured in several terms, such as ohmic resistance, charge transfer resistance and the diffusion transfer resistance. The measurements are carried out in a potentiostat of at a frequency range of 100 kHz to 1 MHz over an AC amplitude of 10 mV. The variations in current as well as in voltage response can be recorded via frequency response analyzer.

EIS values are represented by Nyquist plot, or Bode plot. The Nyquist plot is drawn by plotting negative imaginary impedance values on x-axis, while real impedance values on y-axis. The Bode plot gives the low and high frequency data. The difference between low frequency and high frequency resistance gives the value R_p. To form an equivalent circuit, the Warburg element is connected in parallel to R_s and R_p to demonstrate diffusion mechanism[130].

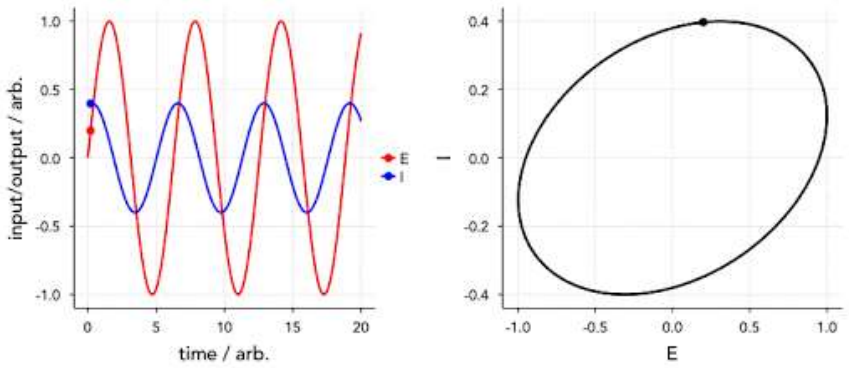

Figure 15: *Principle of Electrochemical impedance spectroscopy.*

3.7.4 Stability test

The stability of electrocatalysts is an important activity parameter related to OER catalysis it can be determined in various ways. The cyclic stability depends upon the change in linear sweep voltammetry (LSV) after performing 1000 cycle Voltammetric scans. It can also be depicted by durability test, which is provided by the change in performance at specific current density (chrono-amperometry) or at a specific applied potential (chronopotentiometry) as a function of time. It works by performing Galvano static or at potentiostatic mode at very long time. The material can be referred as stable if the activity does not vary after such long-term polarization.

Chapter No 4

Results and discussion

4.1 Characterization of e-LSTN

4.1.1 X-ray diffraction analysis of e-LSTN

The crystalline structure of all prepared electrodes was validated by means of XRD and is given in **Fig. 16**. The XRD of as synthesized LSTN exhibited characteristic peaks at $22.76°, 32.46°, 39.94°, 46.50°, 52.40°, 57.84°, 67.89°, 72.65°, 77.32°$, that implies directly to a crystal plane of (100), (110), (111), (200), (210), (211), (220), (221), and (310). The related cubic LSTN structure have a space group of Pm-3m and cell dimensions of $a_o = b_o = c_o$= 3.90, in which A-site is occupied by La, Sr, while B-site is shared by Ti and Ni (JCPDS No: 01-079-0181). Whereas, more pronounced effect of Ni peaks has been observed in e-LSTN.

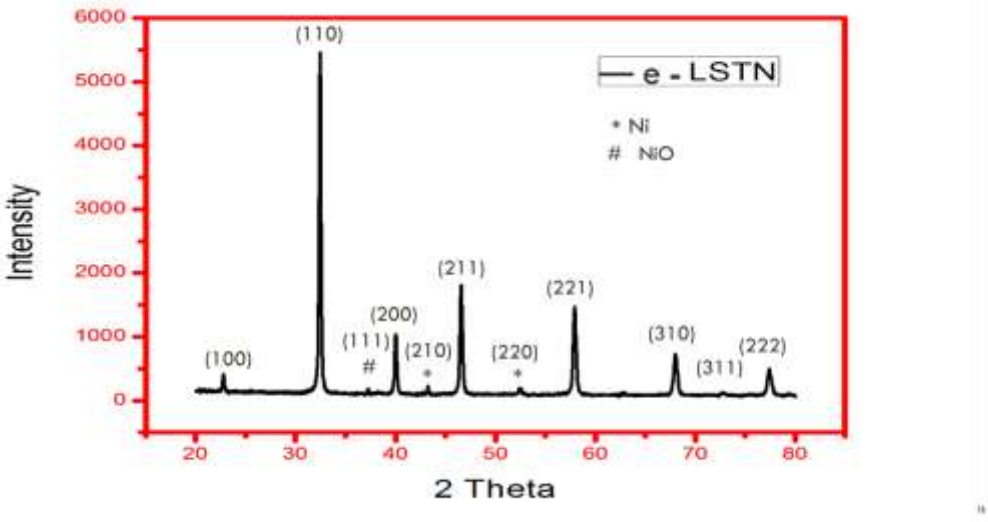

Figure 16: *XRD graph of e-LSTN.*

4.1.2 Scanning electron microscopy (SEM)

The SEM image displayed in **Fig. 17** depicts the irregularly shaped clusters of LSTN perovskite. The clusters are the fine grains of LSTN aggregates having an average dimension of ~70 nm, that provides porous channels to facilitate electrolyte mobility. The interconnecting grains are very useful in regulating charge transportation. Generally, micropores more actively support the adsorption and desorption of electrolyte and offer various active sites for redox reactions, as compared to macropores[131]. The Ni particles get more exposed after exsolution, thereby facilitating the electron/ion diffusion and its contact with electrolyte. This has significantly increased the electrode surface area and efficiency of catalyst. Very small Ni nanoparticles of approx. 30 nm have been observed.

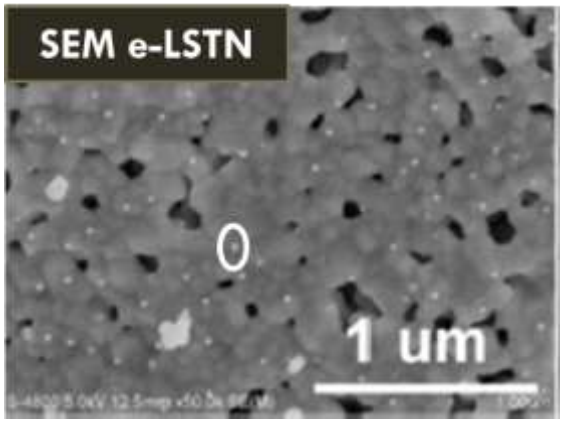

Figure 17: *SEM image of e-LSTN.*

4.2 Electrochemical characterization of e-LSTN for HER

The catalyst has exhibited quite favourable results as compare to LSTN. The synergistic effect between LST that promotes water dissociation as well as the increased H_{ads} from Ni nanoparticles would significantly increase the HER activity. The LST perovskite have excessive OH^-, which are responsible for faster dissociation of water, this will increase e-LSTN activity. The onset of LSV occurs at -0.01, which is less than LSTN (-0.1). Moreover, a very low Tafel slope has been observed for exsolved LSTN along with low overpotential of 91 mV as compared to LSTN (112 mV) at 15 mA cm^{-2} current density, shown in **Fig. 18(a, b)**. The Nyquist plot in Fig. 18(d) shows the smaller resistance for e-

LSTN, which point towards smaller charge transfer resistance and fast transfer of electrons. This will significantly increase HER activity[79]. The compositional flexibility of perovskites makes them highly favourable for energy applications[132].

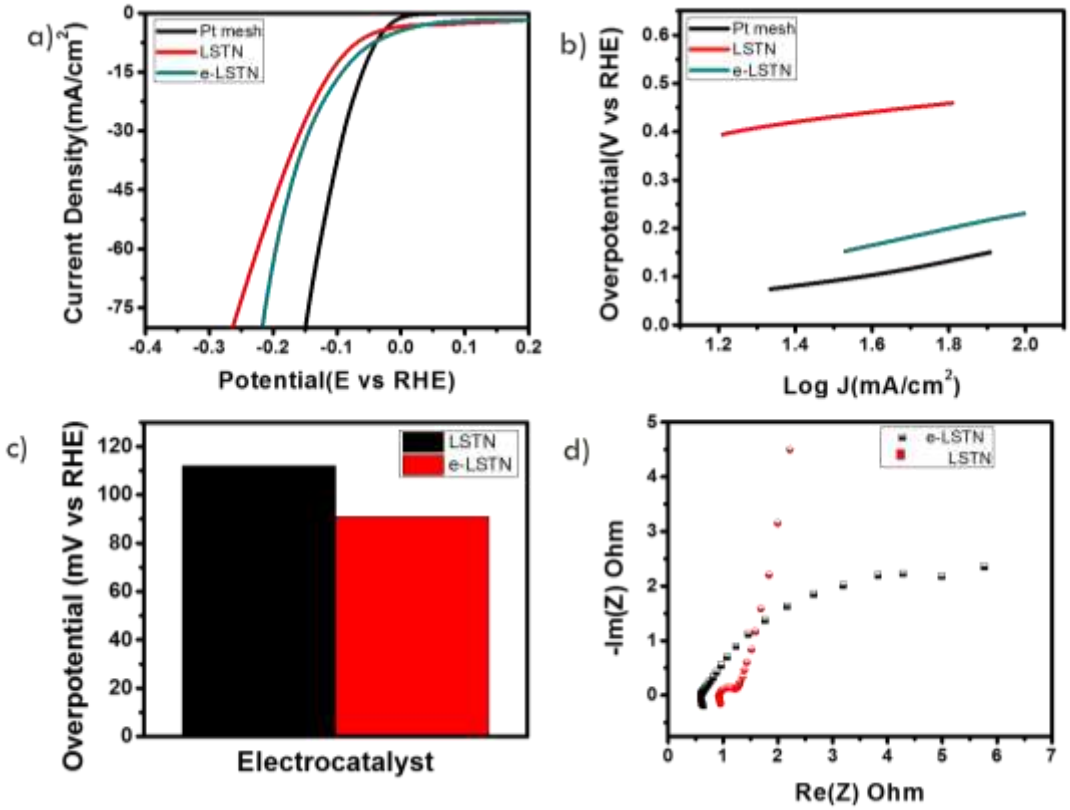

Figure 18: *LSV comparison of Pt mesh, LSTN, e-LSTN at 10 mV s^{-1}. (b) corresponding Tafel plots. (c) corresponding overpotential at 10 mA cm^{-2}(d) Nyquist plot of LSTN, and e-LSTN.*

4.3 Characterization of LSTN, NiMn-LDH, and LSTN@NiMn-LDH electrocatalyst

4.3.1 XRD Pattern of LSTN perovskite and its composite with Layered double hydroxide

The crystalline structure of all prepared electrodes was validated by means of XRD and is given in **Fig. 19.** The XRD of as synthesized LSTN exhibited characteristic peaks at $22.76°, 32.46°, 39.94°, 46.50°, 52.40°, 57.84°, 67.89°, 72.65°, 77.32°$, that implies directly to a crystal plane of (100), (110), (111), (200), (210), (211), (220), (221), and (310). The related cubic LSTN structure have a space group of Pm-3m and cell dimensions of $a_o = b_o = c_o$= 3.90, in which A-site is occupied by La, Sr, while B-site is shared by Ti and Ni (JCPDS No: 01-079-0181). Whereas, the NiMn-LDH has shown seven definite peaks which are located at $10.8°, 22.8°, 34.9°, 38.1°, 48.1°, 60.1°,$ and $61.2°$, which can be referred to crystal plane of following(003), (006), (101/012), (015), (018), (110) and (113) plane reflections of NiMn LDH sheet having a rhombohedral phase (JCPDS No: 00-038-0715). The distance between two planes is (d_{003}) 0.818 nm, which validate a successful manufacturing of NiMn-LDH. For confirmation of LSTN@NiMN-LDH nanocomposite, the individual diffraction peaks of both, LSTN powder and NiMn-LDH were taken as a reference, the heterostructure showed the XRD peaks at $32.46°, 39.94°, 46.50°, 57.84°, 67.89°, 77.32°$, that correspond to plane of (110), (111), (200), (211), (220), and (310), pointing towards LSTN phase. While, peaks at $34.9°, 48.1°, 60.1°,$ and $61.2°$ that correspond to plane of (101/012), (018), (110) and (113) directs to NiMn-LDH phase. The coexistence of two different phases (LSTN and NiMn-LDH) confirms the formation of hybrid nanostructures. However, planes such as (003) and (006) of LDH were not observed in LSTN@NiMN-LDH nanocomposite, which can be attributed to complex and randomly layered NiMn-LDH on LSTN particles, leading to decreased signal intensity, for the plane (003) and (006)[133]. Additionally, the diffraction peaks for pristine NiMn-LDH are much wider, which can be related to comparatively poor crystallinity of LDH, when compared to LSTN[134]. Moreover, no extra peaks are observed indicating that the pure phase LDH layers are grown effectively

on LSTN particles, by using the hydrothermal method without inclusion of any impurities.

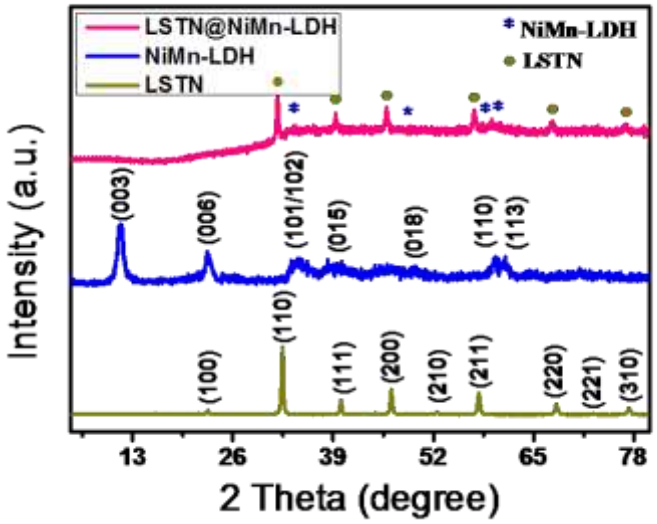

Figure 19: *XRD spectrum of LSTN and LSTN@NiMn-LDH (* shows the characteristic peak of NiMn-LDH, o represents characteristic peaks of LSTN).*

4.3.2 Fourier Transform Infrared Spectroscopy (FTIR)

To further explore the structural characteristics of composite, Fourier Transform-infrared (FT-IR) technique was exploited. The metal oxide bands vibrate within a range of 400-700 cm^{-1} shown in **Fig. 20** FTIR shows broad peaks at 3435 cm^{-1} with strong transmittance, which is assigned to O-H stretching vibration, this is accompanied by interlayer water at around 1634 cm^{-1}. The peak around 1300-1400 cm^{-1} confirms the presence of CO_3^{-2} in composite. The stretching vibration of C-O corresponds to peak at 1097 cm^{-1} [135]. The peaks around 1000-1100 cm^{-1} depicts the presence of $SrTiO_3$, that signifies TiO_6 vibrations, corresponding to bending of Ti-O-Ti[136]. Whereas, the peak around 800 represents metal-oxygen bond, along with the Ti-O stretching vibration shown by TiO_2, that confirms the formation of brucite type layers on LSTN particles.

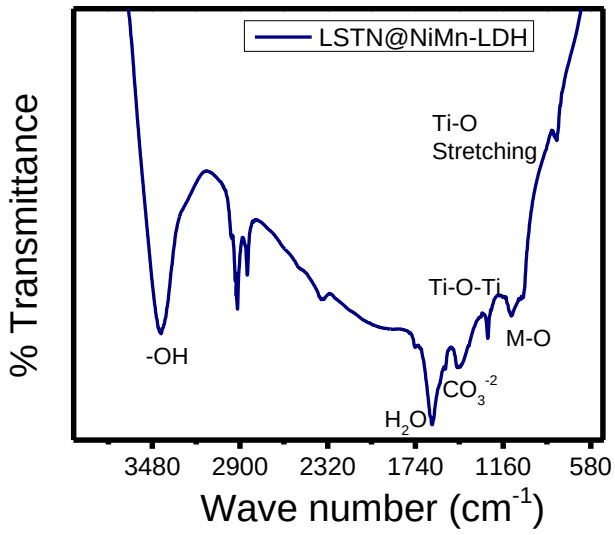

Figure 20: *FTIR result for LSTN@NiMn-LDH*

4.3.3 Raman spectroscopy

Raman spectroscopy is highly practiced to characterize double layer hydroxides. The figure shows the Raman spectra of LSTN perovskite, NiMn-LDH and, LSTN@NiMn-LDH. Raman spectra **(Fig. 21)** shows clear and distinct peaks for LDH at 532 cm^{-1} and 1023 cm^{-1} for NiMn-LDH, which are the characteristic peaks for LDH layers[33]. While, peaks for LSTN are observed at 151 cm^{-1}, 228 cm^{-1}, 267 cm^{-1}, 332cm^{-1}, 525 cm^{-1}, and 778 cm^{-1} [137]. LSTN@NiMn-LDH graph demonstrates a metal-oxygen-metal bond at 545 cm^{-1}, which indicates the characteristic peak for LDH, while peak broadening has occurred at 1687 cm^{-1} that represents CO_3^{-2} in the interlayers of NiMn-LDH[138]–[140]. Moreover, several characteristic peaks observed for LSTN at 151 cm^{-1}, 528 cm^{-1}, 695 cm^{-1}, and 778 cm^{-1}, that undergo peak broadening, which corresponds to internal mobility of oxygen contained by crystalline structure. The peak broadening in heterostructure composite may also be the result of amorphization that can lead to increased OER potentials[137].

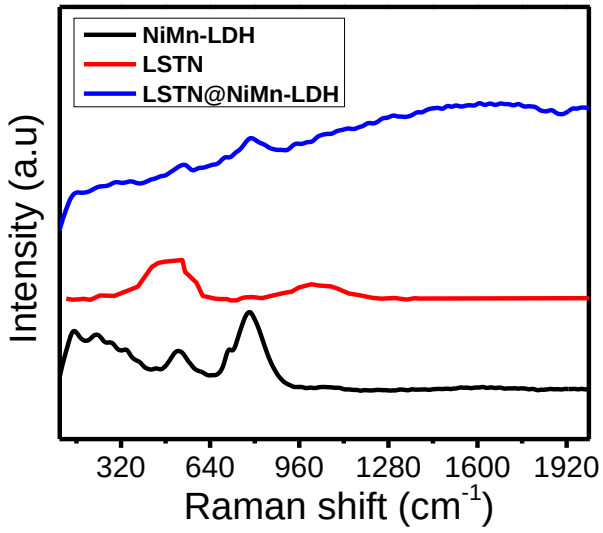

Figure 21: *Raman spectroscopy LSTN, NiMn-LDH and LSTN@NiMn-LDH.*

4.3.4 Scanning electron microscopy

The SEM image displayed in **Fig. 22(a, b)** depicts the irregularly shaped clusters of LSTN perovskite. The clusters are the fine grains of LSTN aggregates having an average dimension of ~40 nm, that provides porous channels to facilitate electrolyte mobility. The interconnecting grains are very useful in regulating charge transportation. Generally, micropores more actively support the adsorption and desorption of electrolyte and offer various active sites for redox reactions, as compared to macropores[131]. The three-dimensional porous electrodes are more beneficial as compared to conventional two-dimensional structures, as they facilitate electron transportation and penetration of electrolyte through micropores, thus, offering a highly electrochemically active surface[141]. The 3D heterostructure of upright aligned NiMn-LDH nanosheets over nickel foam are displayed in **Fig. 22(c, d).** Since, the nanolayered structure provides a quick current response owing to synergistic effect of 3D hierarchy and inherently highly active materials. Additionally, high resolution figure reflects that the interlinked nanosheets with suitable orientation should originate from the chain-like aggregates located on Ni foam. The morphology of LSTN@NiMn-LDH shows standard porous morphology on Ni foam, decorated uniformly and perpendicularly in highly dense

manner over the substrate, as shown in **Fig. 22(e, f)**. The homogeneous anchoring of NiMn-LDH onto LSTN perovskite surface effectively prevents the packing and self-aggregation. The heterostructure composite can offer a large specific surface area with porous features, that facilitates the electrolyte flow towards entire nanosheets, and thereby attain high catalytic performance. A zoomed in image of composite expresses a petal-type structure as exhibited by hydrangea having an average diameter of one micron. There are several crevices among individual petals, providing various paths for electrolyte ion penetration as well as mass transport, from **Fig. 22(f).** The hydrangea-type design consists of~25 nm thick curly sheets with an air gap of 200 nm between them. The high catalytic performance is exhibited by the ultrathin nature of highly oriented layered hybrid crystal structure. **Fig. 52(a, b)** in appendices shows images of LSTN@NiMn-LDH heterostructure.

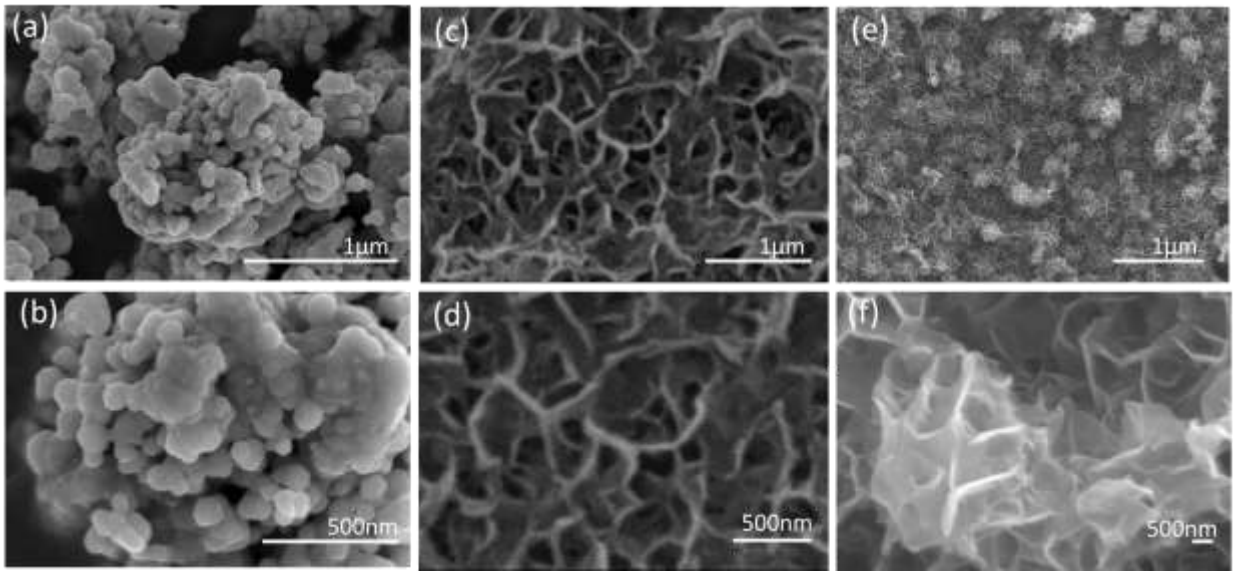

Figure 22: *(a, b) represents SEM images of LSTN. (c, d) represents SEM micrographs of NiMn-LDH. (e, f) shows SEM image of LSTN@NiMn-LDH at different magnifications.*

4.3.5 Energy dispersive X-ray spectroscopy

Energy-dispersive X-ray spectroscopy (EDX) analysis was performed for further analysis, which shows that the as prepared nanocomposite mainly consists of La, Sr, Ti, Ni, Mn and O elements, thus, implying the successful formation of hybrid of LSTN and

NiMn-LDH **(Fig. 23).** The high intensity signal for Sr and Ni element reveals that the doping of Sr and Ni elements into A-site (La) and B-site (Ti) were successfully done in LSTN[136]. The presence of high Ni fraction is the effect of a Ni substrate accompanied by its presence in heterostructure. **Table. 10** in appendices show the atomic percentage of components in LSTN@NiMn-LDH.

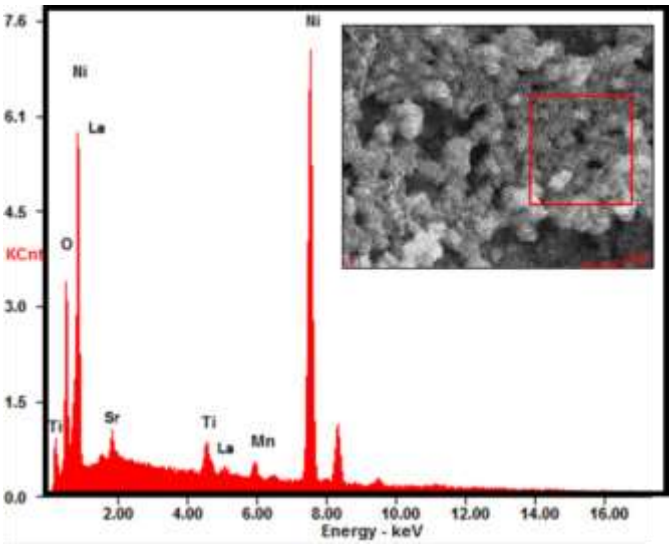

Figure 23: *EDS spectrum for LSTN@NiMn-LDH supported on Nickle foam.*

4.4 Electrochemical testing of LSTN, LSTN@NiMn-LDH, and NiMn-LDH for OER and HER

4.4.1 Linear sweep voltammetry results for OER

In order to perform electrochemical measurements, three electrode assembly of the bare Ni foam, Pt mesh, LSTN/NF, NiMn-LDH/NF, and LSTN@NiMn-LDH/NF in 1 M KOH solution was used. The OER performance of LSTN@NiMn-LDH was estimated through the LSV polarization curve. In order to study the influence of heterostructure on Ni substrate, LSTN/NF and NiMn-LDH/NF were also synthesized and tested under identical conditions for OER performance. As shown in **Fig. 24,** their polarization curve for OER shows the oxidation peak at a potential of 1.37 V which corresponds to Ni and Mn oxidation. The anodic current density of LSTN@NiMn-LDH/NF increases quickly, when potential is >1.52 V. Linear sweep voltammetry (LSV) reveals a great difference in OER

activities as compare to LSTN and NiMn-LDH activity. The doping of perovskite at A-site (Sr) and B-site (Ni) critically improves the bifunctional activity of perovskite. Several oxygen vacancies are created by Sr doping, which is responsible for providing several chances for oxygen ion to diffuse[82]. Moreover, the oxygen vacancies provided by Ni doping that enhanced the catalytic activity can be attributed to several Ni^{3+} on the surface. Still, the OER activity of LSTN is much inferior than Co based perovskites[79]. Therefore, there is a need to improve OER, by preparing hybrid catalysts that can be used for various applications. The addition of NiMn-LDH in electrode material considerably improves the electrochemical performance, which could be attained due to conductive pathways provided by NiMn-LDH network. NiMn-LDH permits efficient intercalation and deintercalation of OH^- by presenting more conductive channels for fast ions transportation through the interface of electrode/electrolyte, thus enhancing the overall electrochemical performance of electrodes[142].

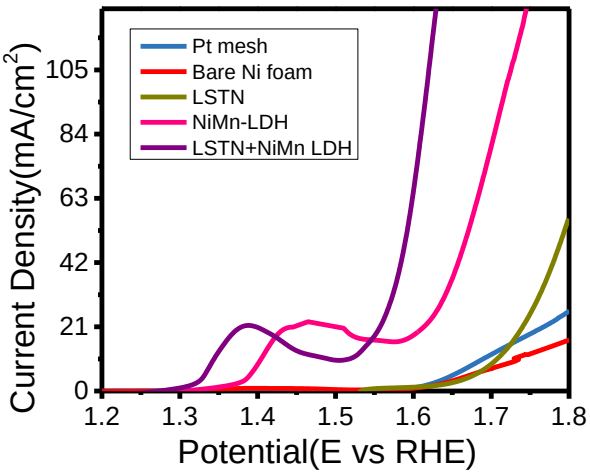

Figure 24: *Polarization curve OER for LSTN, NiMn-LDH, and LSTN@NiMn-LDH at a scan rate of 10 mV s^{-1} in 1 M KOH.*

The OER performance of LSTN@NiMn-LDH is also assessed by overpotential and anodic current density at 1.6 V, which shows that LSTN@NiMn-LDH requires very low overpotential (125 mV and 387 mV at 15 and 100 mA cm^{-2} current density), which is much less than LSTN and NiMn-LDH that has shown quite large overpotential of 185

mV and 494 mV at 15 mA cm^{-2} **(Fig. 25(a)).** In addition, the activity for LSTN@NiMn LDH has increased approx. 4 times the NiMn-LDH due to synergistic interface effect. In **Fig. 25(b)**, the current density at 1.6 V for LSTN, NiMn-LDH, and LSTN@NiMn-LDH has found to be 65, 18 and 1.28 mA cm^{-2}.

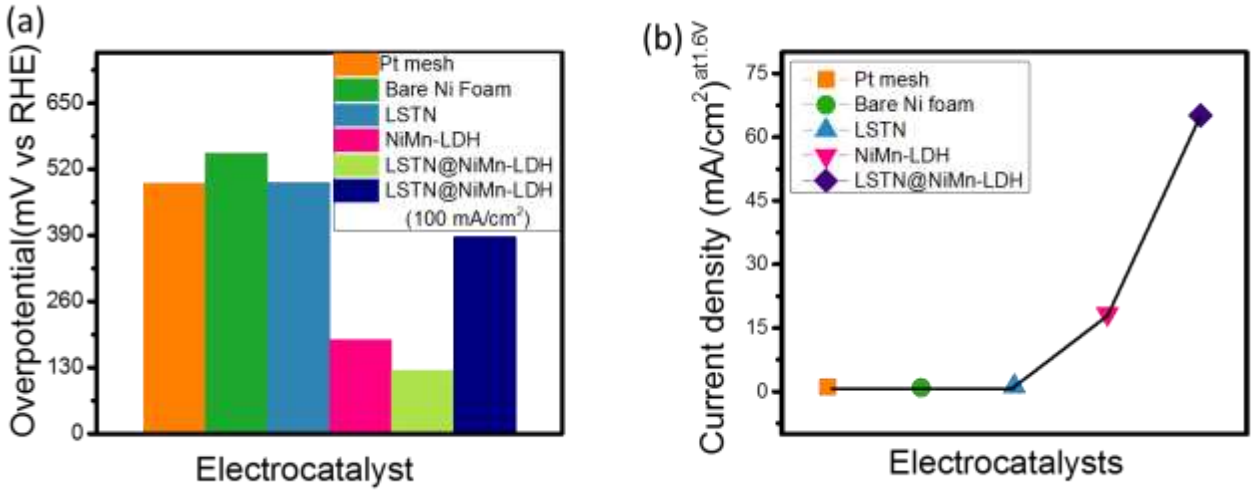

Figure 25: *(a) Overpotential required at 15 mA cm^{-2} and (b) Current density of LSTN, NiMn-LDH and LSTN@NiMn-LDH at 1.6 VRHE for OER.*

The high electrochemical activity of LSTN@NIMN-LDH can also be confirmed by the low Tafel slope of LSTN@NiMn-LDH(103 mV dec^{-1}) as compare to NiMn-LDH (134 mV dec^{-1}) and LSTN (140 mV dec^{-1}) show in **Fig. 26.** The low Tafel slope value for LSTN@NiMn-LDH shows higher electrocatalytic performance capacity as the rate of this catalyst increases with an increase in potential. A wide variety of adsorbed oxygen species and their interaction with heterostructured catalyst on cation site of transition metal is responsible for this significant behavior[39].

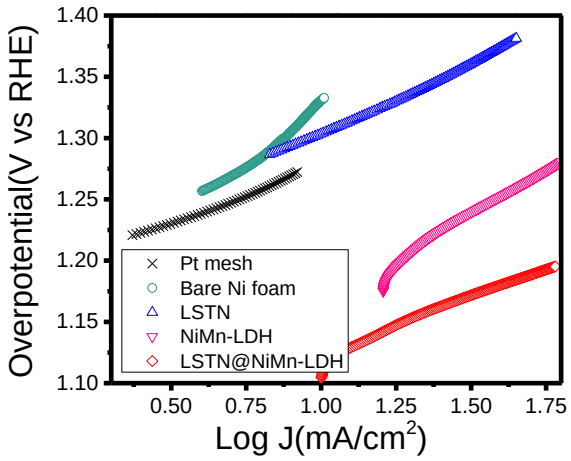

Figure 26: *Corresponding Tafel slope of Pt mesh, bare Ni foam, LSTN, NiMn-LDH and LSTN@NiMn-LDH.*

4.4.2 Linear sweep voltammetry results for HER

In order to perform electrochemical measurements, three electrode assembly of the bare Ni foam, Pt mesh, LSTN/NF, NiMn-LDH/NF, and LSTN@NiMn-LDH/NF in 1 M KOH solution was used. The OER performance of LSTN@NiMn-LDH was estimated through the LSV polarization curve. In order to study the influence of heterostructure on Ni substrate, LSTN/NF and NiMn-LDH/NF were also synthesized and tested under identical conditions for HER performance. To estimate the electrocatalytic performance of LSTN@NiMn-LDH, we further studied the HER performance of the as-synthesized catalyst. The LSTN catalyst presents good HER activity (comprising superior mass activity as well as fast reaction kinetics). As we know, the most favorable HER catalyst is Pt/C/NF, the activity of LSTN perovskite need to be further improved, in order to approach the standard activity. **Fig. 27** displays comparison of linear sweep voltammetry curve for LSTN, NiMn-LDH and LSTN@NiMn-LDH, which suggests very low onset potential for heterostructure composite supported on nickel foam.

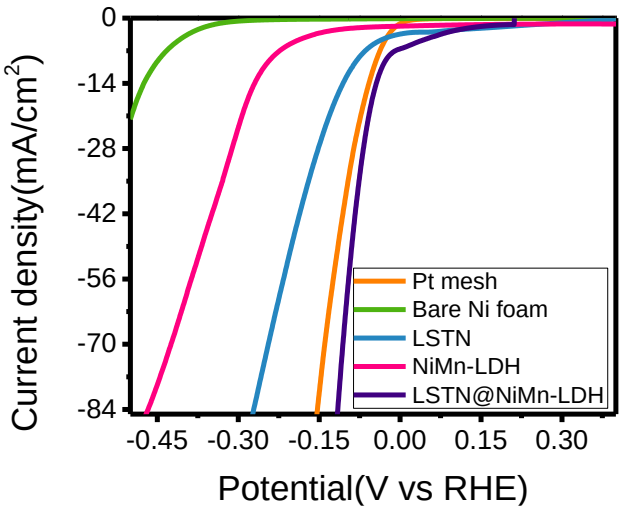

Figure 27: *Polarization curve HER for LSTN, NiMn-LDH, and LSTN@NiMn-LDH at a scan rate of 10 mV s^{-1} in 1 M KOH.*

Luckily, the overpotential value for LSTN@NiMn-LDH is 31.3 mV, which is calculated at 10 mA cm^{-2} current density, and even higher current densities at more negative potentials **(Fig. 28(a))** showing the excellent catalytic results. The overpotential required by LSTN@NiMn-LDH to achieve a current density of 100 mA cm^{-2} is only 125. Whereas, LSTN and NiMn-LDH possess large overpotentials to attain even 10 mA cm^{-2} current density. Besides, heterostructured LSTN@NiMn-LDH has also shown a low Tafel slope (84 mV dec^{-1}) than LSTN (106 mV dec^{-1}) and NiMn-LDH (194 mV dec^{-1}), indicating prime activity of LSTN@NiMn-LDH for HER (**Fig. 28(b)**). Moreover, the low Tafel slope value for composite material indicates that LSTN@NiMn-LDH possess different rate determining step than LSTN and NiMn-LDH. This idea challenged the perception that the achievement of 100 mA cm^{-2} current density is difficult for HER, while pertaining the low overpotential, which can be practically commercialized for various applications. When the overpotential is 125 mV at a current density of 100 mA cm^{-2}, the activity surpasses the overpotential for most of the reported materials in alkaline media such as $NiCo_2S_4$/NF[143] (195 mV), Cu@NiFe-LDH[144] (192 mV) and NG-NiFe@MoC_2 [145] at a current density of 100 mA cm^{-2}. LSTN@NiMn-LDH displays the high current density at -0.1 V, which is 62 mA cm^{-2} which is much greater than LSTN and NiMn-LDH (12.7 and 6.98 at -0.1 V respectively) (**Fig. 28(c)**). The exceptional

electrochemical performance of LSTN@NiMn-LDH could be attained due to synergistic effect between LSTN nanoparticles and NiMn-LDH, along with the conductive support provided by Ni foam. As, it enhances the adsorption of hydrogen and, thus the ordering of phases provide an outstanding electrocatalyst. The porous Ni foam not only offers mechanical stability but also facilitates the movement of electrolytic ions towards electroactive sites by providing smaller pathways[146].

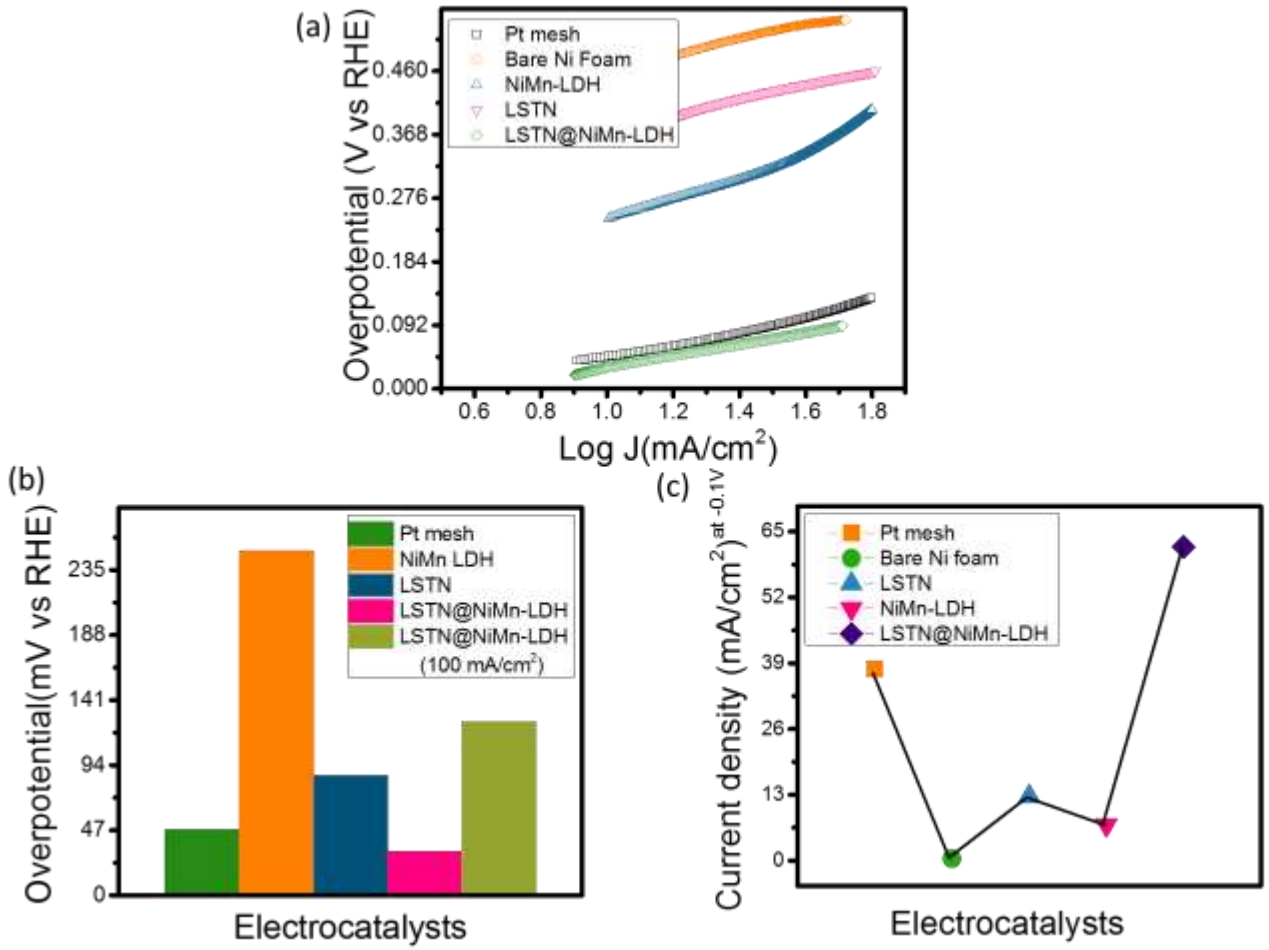

Figure 28: *(a) Corresponding Tafel plots, (b) Overpotential required at 10 mA cm^{-2} (c) Current density of LSTN, NiMn-LDH and LSTN@NiMn-LDH at -0.1 V_{RHE} for OER.*

4.4.3 Cyclic voltammetry

Fig. 29 shows the cyclic voltammogram of LSTN@NiMn-LDH/NF, when a scan rate of 5 to 100 mVs^{-1} is applied. The potential range 0-0.6 V shows a pair of definite redox peaks (corresponding to B-type curves)[147]. Moreover, the critical step in defining the reversibility of electrode material is OH^- adsorption at electrode surface. The shape of CV remains constant even by increasing the scan rate, this represents the small resistance, high cyclic stability and extraordinary catalytic performance of electrodes. By increasing the scan rate, diffusion layer resistance reduces, thereby achieving the higher current densities. Besides, the OER activity of nickel foam is low and do not contribute much in studied potential range of OER, it is only added as a conductive support material[133], [148]. The porosity in nickel foam provides efficient transmission channels, and easiness in departure of oxygen and hydrogen[149]. These redox peaks are associated with faradaic redox reactions, which are related to L-O/L-O-OC and L-S/L-S-OC, where L represents Ni or Mn, C stands for H or K[140]. NiMn-LDH dissolves in 1 M KOH giving the following redox reactions during the energy storage process[150].

$$Ni(OH)_2 + OH^- \leftrightarrow NiOOH + H_2O + e^- \quad (18)$$

$$Mn(OH)_2 + OH^- \leftrightarrow MnOOH + H_2O + e^- \quad (19)$$

$$MnOOH + OH^- \leftrightarrow MnO_2 + H_2O + e^- \quad (20)$$

The charge transfer occurs through NiMn-LDH layers by electron hopping among the redox sites and transfer of ions through the pores in the electrode, that keeps the structure neutral[140].

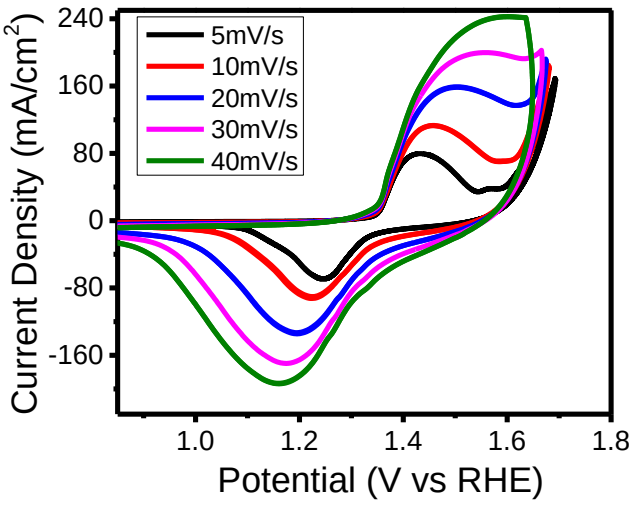

Figure 29: *Cyclic voltammetry curve for LSTN@NiMn-LDH at a scan rate of 5, 10, 20, 40 & 50 mV* s^{-1}.

The CV curves for LSTN, NiMn-LDH are shown in **Fig. 30(a-d).** The cyclic voltammogram are obtained at a scan rate of 5 to 100 mVs^{-1}. The potential range 0-0.6 V shows a pair of definite redox peaks (corresponding to B-type curves)[147]. The data shows IR-corrected graphs for LSTN, NiMn-DH and LSTN@NiMn-LDH. The critical step in defining the reversibility of electrode material is OH^- adsorption at electrode surface. The shape of CV remains constant even by increasing the scan rate, this represents the small resistance, high cyclic stability and outstanding catalytic performance of electrodes. By increasing the scan rate, diffusion layer resistance reduces, thereby achieving the higher current densities. The comparison of CV curves for LSTN, NiMn-LDH and, LSTN@NiMn-LDH shows clear difference in redox peaks as well as current density for the prepared composite. This validates the high capacitance and storage capacity of pas synthesized composite. The linear increase of redox peaks with scan rate shows that redox process is confined to LSTN@NiMn-LDH surface, which confirms the stability of electrode. The linear behavior of redox peaks with $\upsilon^{1/2}$ also reveals that electron transfer process is diffusion controlled[151].

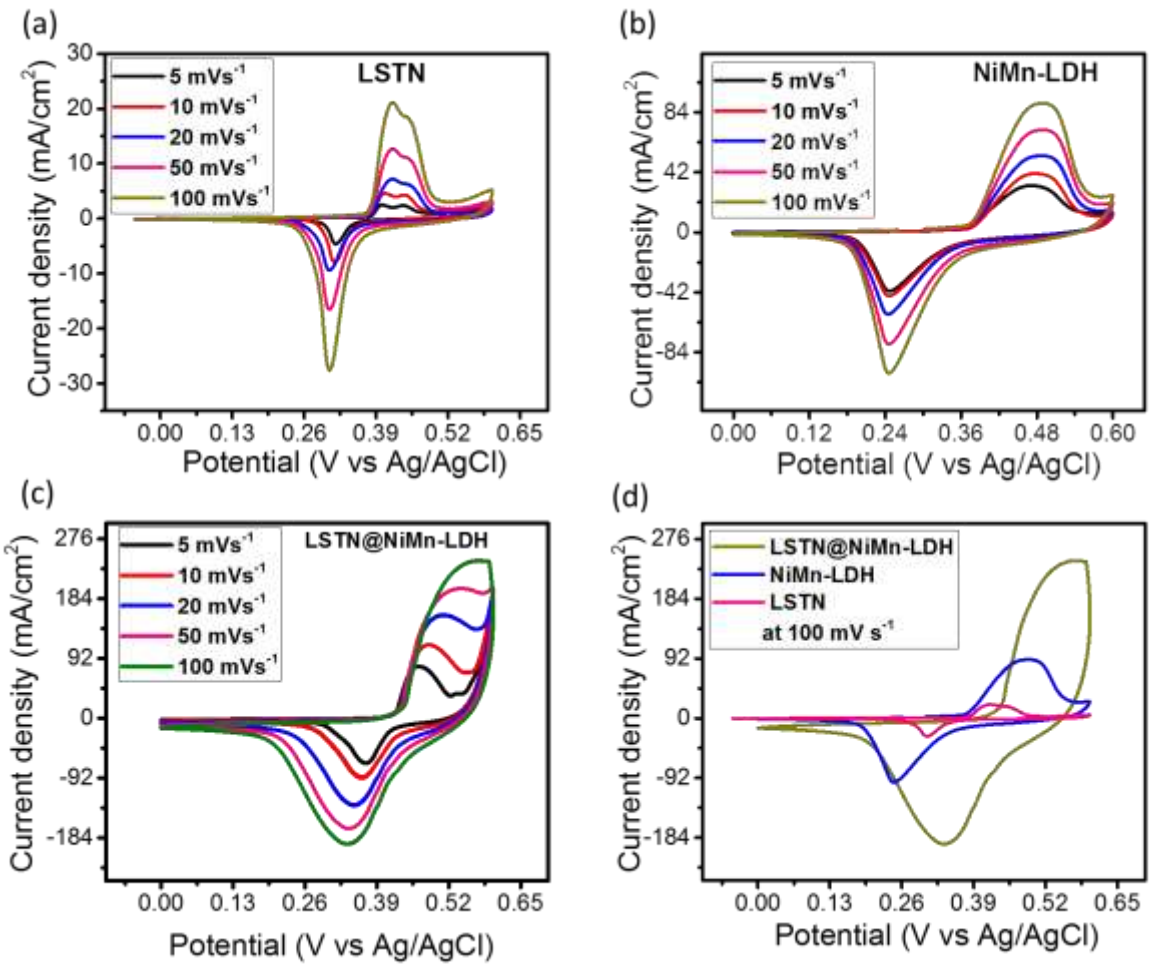

Figure 30: *CV curves at scan rates 5, 10, 20, 40, 50 and 100 mV s^{-1} of (a) LSTN, (b) NiMn-LDH, (c) LSTN@NiMn-LDH, given as potential vs reference electrode (Ag/AgCl). (d) Comparison of CV curves at 100 mV s^{-1} for LSTN@NiMn-LDH, NiMn-LDH & LSTN.*

4.4.4 Electrochemical impedance spectroscopy

Furthermore, the kinetics of as obtained catalyst was further investigated by impedance spectroscopy measurements shown in **(Fig. 31).** The test was performed in 1 M KOH solution within a frequency range of 20^5 Hz - 0.1 Hz. The graph inset shows equivalent circuit elements, the ohmic resistance which is associated to the electrolyte between two electrodes is represented by R_1, where, R_2 corresponds to charge transfer resistance given as polarization resistance, at the interface among electrode and electrolyte, where, W is named as Warburg impedance, while C_2 depicts the faradic capacitance. Alongside, a semicircle within Nyquist plot represents polarization resistance, which is caused by

faradic reaction occurring at electrode surface. The reduced charge transfer resistance (Rct) has been observed for LSTN@NiMn-LDH which is shown by a small diameter of semicircle indicating the proficient charge transferability[152], [153]. The observed polarization resistance of LSTN/NF is 3.981 Ω and for LSTN@NiMn-LDH/NF, it's 4.929 Ω, respectively. The electrolyte resistance for the LSTN/NF, NiMn-LDH/NF, and LSTN@NiMn-LDH/NF was found to be 1.245 Ω, 0.723 Ω, and 0.653 Ω, respectively, shown in **Table 5**. The high charge transfer is achieved due to band structure changes for LSTN after forming a composite with NiMn-LDH[136].

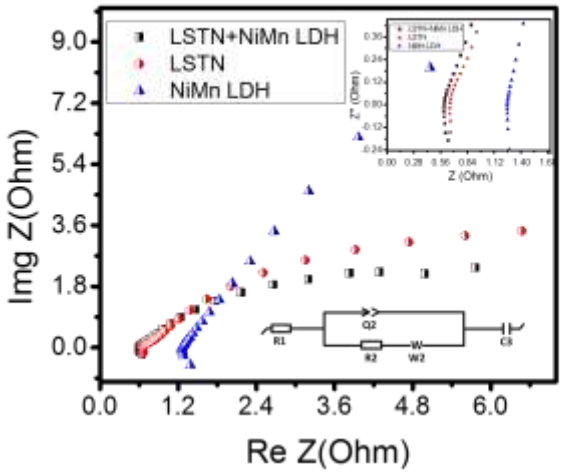

Figure 31: *The Nyquist plot at frequency 200 kHz-0.1Hz for LSTN, NiMn-LDH, and LSTN@NiMn-LDH.*

Table 5: *Electrochemical results for OER and HER.*

Catalyst	R_1 (Ω)	R_2 (Ω)	C_2 (e^{-3} F)	Voltage (V) @ 10 mA cm^{-2}	
				OER	HER
LSTN	1.245	5.041	0.017	1.704	-0.085
NiMn-LDH	0.723	4.156	0.036	1.40	-0.24
LSTN@NiMn-LDH	0.653	3.354	1.722	1.34	-0.030

4.4.5 Stability test

In addition, LSTN@NiMn-LDH was further observed for stability test at 100µA for 24 hrs., **(Fig. 32(a)).** The potential from chronopotentiometry results for heterostructure has shown the stable behavior, which is achieved by its structural characteristics. The low ion diffusion resistance which is driven by efficient interfacial area between electrode and electrolyte favors quick ion penetration across the widely exposed active sites. This occurs due to activation of synthesized material during chronopotentiometry test. The potential rapidly responds initially but then remains unchanged after 3 hrs. The difference in potential obtained is only 0.03%. **Fig. 32(b)** shows the stability test for hydrogen evolution reaction by comparing linear sweep voltammetry results for LSTN@NiMn-LDH initially and after operating it at 1000 cycles. The LSV curve shows quite a stable result, as onset potential and current density has given the same value to before 1000 cycles. The **Fig. 52** in appendices show the SEM of LSTN@NiMn-LDH after HER, and OER testing. The structure is found to be highly stable.

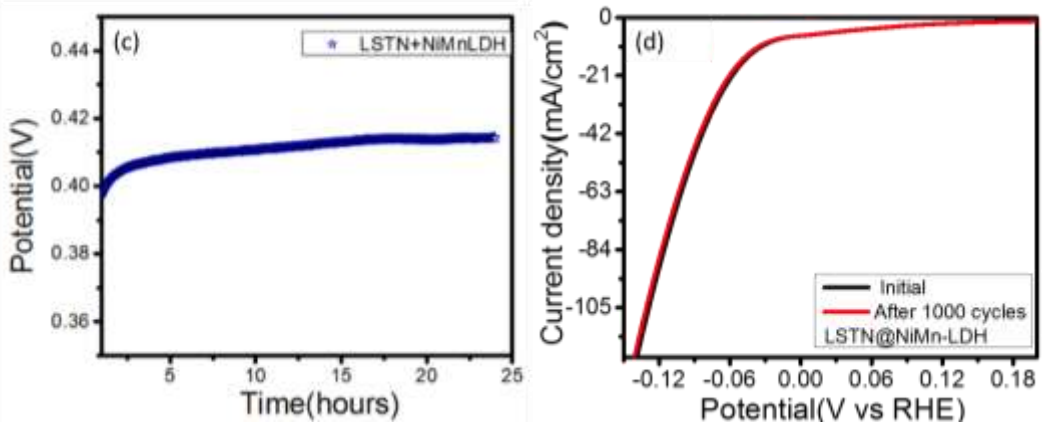

Figure 32: *(a) Chronopotentiometry curve for LSTN@NiMn-LDH for 24 hrs. (b) Stability test for LSTN@NiMn-LDH showing linear sweep voltammetry result after 1000 cycles.*

4.4.6 Comparison of result with literature

Table 6: *Comparison of bifunctional performance of various transition metal oxide catalysts.*

Catalyst	Electrolyte	Onset potential (V)	Ref

		OER	HER	
LSTN@NiMn-LDH/NF	1 M KOH	1.508	0.00675	This work
LSTN	1 M KOH	1.583	0.021	This work
NiMn-LDH	1 M KOH	1.673	-0.201	This work
$NiCo_2S_4$@NiFe LDH	1 M KOH	1.42	-0.17	[148]
NiCoP@NiMn LDH	1 M KOH	1.51	-0.06	[133]
$Sr_{0.95}Co_{0.8}Nb_{0.1}Ni_{0.1}O_{3-\delta}$	1 M KOH	1.55	N.A.	[94]
MnCo-G/NF	1 M KOH	1.52	-0.14	[20]
MnCo/NF	1 M KOH	1.54	-0.14	[20]
NiFe LDH/CNT	1 M KOH	1.50	N.A.	[43]

4.5 Characterization results of LSTN/MXene composites

4.5.1 X-ray diffraction analysis of catalysts:

The crystalline structure of all prepared electrodes was validated by means of XRD and is given in **Fig. 33**. The XRD of as synthesized LSTN exhibited characteristic peaks at 22.76°, 32.46°, 39.94°, 46.50°, 52.40°, 57.84°, 67.89°, 72.65°, 77.32°, that directly corresponds to a crystal plane of (100), (110), (111), (200), (210), (211), (220), (221), and (310). The LSTN structure is cubic having a space group of Pm-3m and cell dimensions of $a_o = b_o = c_o$= 3.90, in which La & Sr occupies A-site, while Ti and Ni resides on B-site (JCPDS No: 01-079-0181). Whereas, the MXene ($Ti_3C_2T_x$) has shown thirteen definite peaks which are located at 8.81°, 18.36°, 27.56°, 33.81°, 35.03°, 36.80°, 38.78°, 41.58°, 44.37°, 47.64°, 53.66°, 57.37°, and 60.40°, which can be referred to crystal plane of following(002), (004), (006), (101), (102), (105), (106), (107), (108), (109) and (110) plane reflections of MXene sheet. The distance between two planes is (d_{002}) 1.002 nm, which validate a successful manufacturing of MXene[37]. For confirmation of LSTN/MXene nanocomposite, the analysis of individual diffraction peaks of both components was made, LSTN powder and MXene were taken as a reference, the heterostructure showed the XRD peaks at 31.79°, 39.38°, 45.87°, 57.26°, 67.28°, 77.04°, that correspond to plane of (110), (111), (200), (211), (220), and (310), pointing towards LSTN phase. While, peaks at 8.76°, 18.25°, 34.76°, 41.54°, 59.42°, that correspond to plane of (002), (004), (101/102), (105) and (110) directs to MXene phase. The coexistence of two different phases (LSTN and MXene) confirms the formation of nanostructured composite. The HF treatment of MAX phase produce heat which resulted in formation of anatase TiO_2 in small amount[154]. Additionally, the diffraction peaks get broadened and have much lower intensity than the parent compounds, which corresponds to deposition of LSTN nanoparticles on etched MXene nanosheets[37], [38]. Moreover, the lower peak shift of (002) plane is attributed to removal of Al layers in Ti_3AlC_2 and surface terminations (-F, -OH, and -O)[155]. The shifting of peak angles for composite towards lower angle suggests increased lattice parameters for LSTN/MXene nanocomposite due to intercalation of LSTN nanoparticles within MXene microlayers[156]. As, for peak (002), the left shift of peak suggested the increased c

lattice parameter from 1.02 nm to 1.24 nm. It can be seen that size of LSTN nanoparticles is (~40 nm) larger than the interlayer distance of MXene sheets, which suggested the shift in peak position, and thereby increasing the interlayer distance[157]. While, no extra peaks are observed indicating that the pure phase LSTN particles are grown effectively on MXene layers.

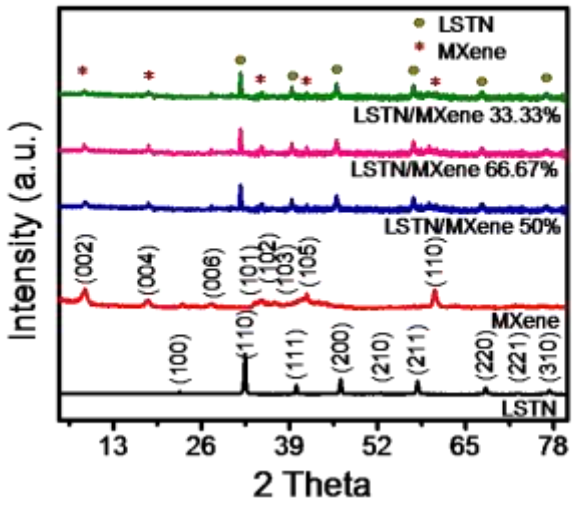

Figure 33: *XRD pattern of LSTN, MXene, LSTN/MXene 50%, LSTN/MXene 66.67% and LSTN/MXene 33.33%.*

4.5.2 Raman spectroscopy

Raman spectroscopy is highly practiced to characterize electrocatalysts. Raman spectra **(Fig. 34)** demonstrates diffraction peaks of as prepared $Ti_3C_2T_x$, which are consistent with the reported data. Raman spectroscopy of LSTN/MXene 66.67% shows a blue shift from MXene to LSTN/MXene 66.67% for bands at 376 cm^{-1} and 609 cm^{-1}, which verifies the interaction between LSTN nanoparticles and MXene layers[158]. The two broad peaks have been observed between 1000 and 1700 cm^{-1}, which are the characteristic for D and G modes. These peaks might show the presence of graphitic carbon that indicates a conductive carbide layer ensuring fast charge transfer[159]. Moreover, several characteristic peaks observed for LSTN at 151 cm^{-1}, 528 cm^{-1}, 695 cm^{-1}, and 778 cm^{-1}, which undergo peak broadening, which corresponds to the internal mobility of oxygen

contained by crystalline structure. The broadening and shifting of peaks in Raman spectra is also the result of oxygen vacancy creation by doping of Ni ion at B-site[160]. The peak broadening in heterostructure composite may also be the result of amorphization that can lead to increased OER potentials[137].

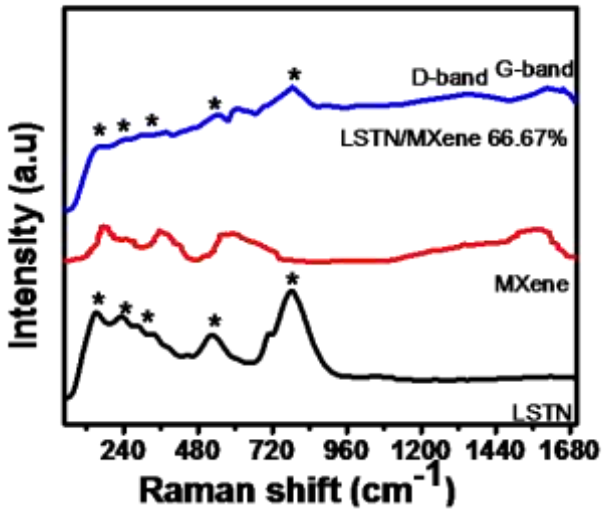

Figure 34: *Raman spectroscopy graph for LSTN, MXene, LSTN/MXene 66.67%.*

4.5.3 Surface morphology

The SEM image shown in **Fig. 35(a)** represents LSTN perovskite having irregularly shaped clusters. The clusters are the fine grains of LSTN aggregates having an average dimension of ~40 nm, that provides porous channels to facilitate electrolyte mobility. The interconnecting grains are very useful in regulating charge transportation[131]. Generally, micropores more actively support the adsorption and desorption of electrolyte and offer various active sites for redox reactions, as compared to macropores[131]. Moreover, two-dimensional titanium carbide material, which has been reported as highly conductive and hydrophilic, thereby providing quick ion/electron transport through the substrate[161]. The SEM image of MXene sheets exfoliated by HF treatment indicates that MXene $Ti_3C_2T_x$ sheets are rough after their treatment with HF that facilitates the incorporation of LSTN nanoparticles within MXene sheets. Etching process leads to formation of many termination groups such as -O, -OH, and -F on MXene sheets[154].

The SEM image of LSTN nanoparticles dispersed within the layered $Ti_3C_2T_x$ nanosheets is displayed in **Fig. 35(b).** Since, the nanolayered structure provides a quick current response owing to fast ion/electron transfer of hybrid and inherently highly active materials. The morphology of LSTN/MXene-67% has also been examined by TEM analysis. The TEM image shows two characteristic morphologies including nanosheets of MXene along with the nanoparticles of LSTN perovskite, which can be clearly seen in **Fig. 35(c-e)**. The LSTN/MXene composite layers exhibits a rough surface, suggesting that LSTN nanoparticles are effectively inserted within MXene nanosheets, which corresponds with the XRD results. The nanosheets of MXene exhibits lattice fringes having d-spacing of 0.32 nm, which reflects a plane of (006)[154]. The incorporation of LSTN nanoparticles within $Ti_3C_2T_x$ nanosheets not only increases surface area of LSTN/MXene composite by enlarging the interlayer distance between MXene nanosheets for cation intercalation, but it also offer new paths for diffusion of electrolyte ions[159]. The ultrasonication process facilitated the transport of LSTN nanoparticles within exfoliated thin and transparent films of MXene. It can be seen that the addition of MXene has provided the more open structure with numerous accessible channels that will make flow of electrolyte solution easier. The interlaced LSTN nanoparticles within 2D MXene nanosheets provides more favorable electrocatalytic activities, that will shorten the mass diffusion and facilitates the charge transfer. An enormous increase in surface area of MXene was observed on addition of perovskite nanoparticles upon ultrasonication. The achievement of large surface area with porous features helps in facilitating the electrolyte flow towards entire nanosheets, and thereby attain high catalytic performance.

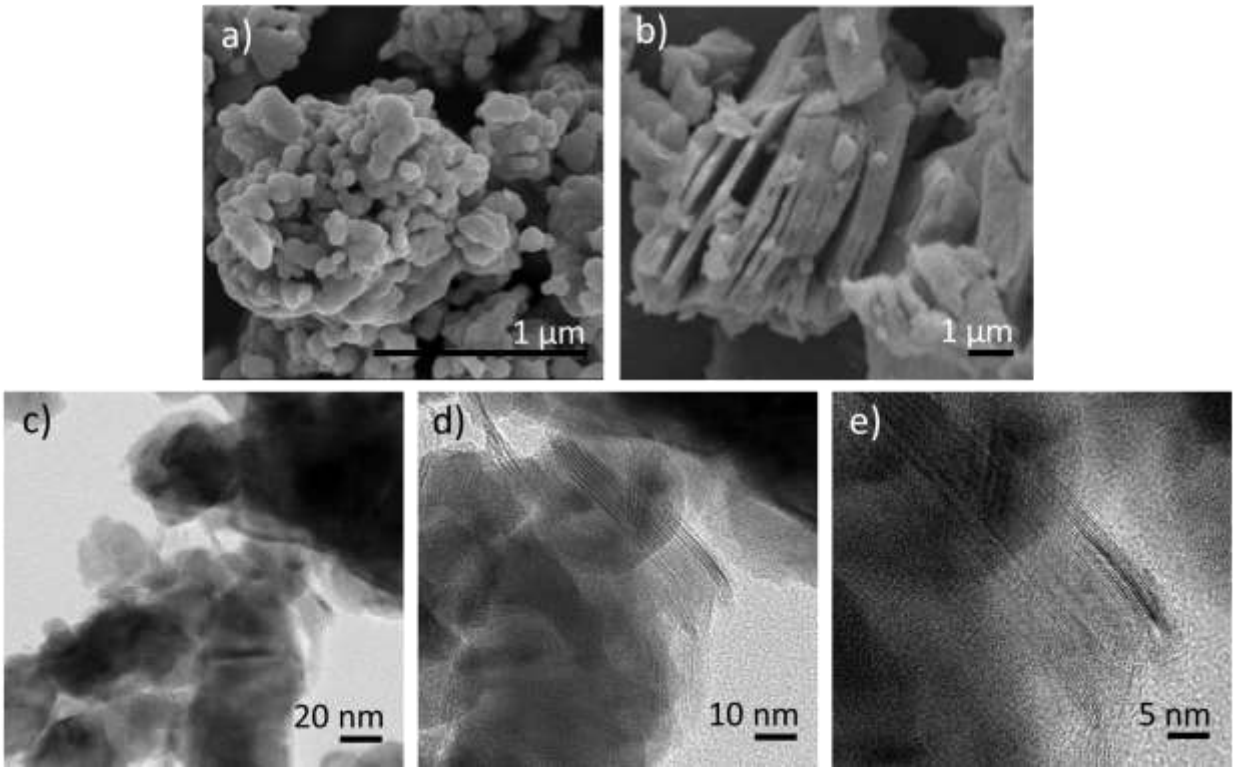

Figure 35: *(a) SEM image of LSTN nanoparticles. (b) SEM image of LSTN/MXene 66.67% composite. (c-e) TEM images of LSTN/MXene 66.67% composite at different resolutions, clearly demonstrating MXene layers along with LSTN nanoparticles.*

4.5.4 Energy dispersive X-ray spectroscopy

Energy-dispersive X-ray spectroscopy (EDX) spectrum was performed for further analysis, which shows that the as prepared nanocomposite mainly consists of La, Sr, Ti, Ni, C, F and O elements, thus, implying the successful formation of hybrid of LSTN and MXene **(Fig. 36(a)).** The high intensity signal for Sr and Ni element reveals that the doping of Sr and Ni elements into A-site (La) and B-site (Ti) were successfully done in LSTN[136]. While, the presence of C & F indicates existence of MXene nanosheets within composite structure. The elemental mapping of as synthesized material is shown in **Fig. 36(b-h).** The analysis of LSTN/MXene 66.67% was made to further confirm the formation of MXene nanosheets interlaced with LSTN nanoparticles, which validates the presence of C, Ti, La, Sr, Ni, O in composite. The amount of carbon and titanium is found to be higher due to presence of LSTN and MXene in 1:2. The presence of titanium in

perovskite structure also support rich amount in composite structure. The LSTN/MXene composite maintained the multilayered structure and has undergone attachment of LSTN nanoparticles between MXene nanolayers.

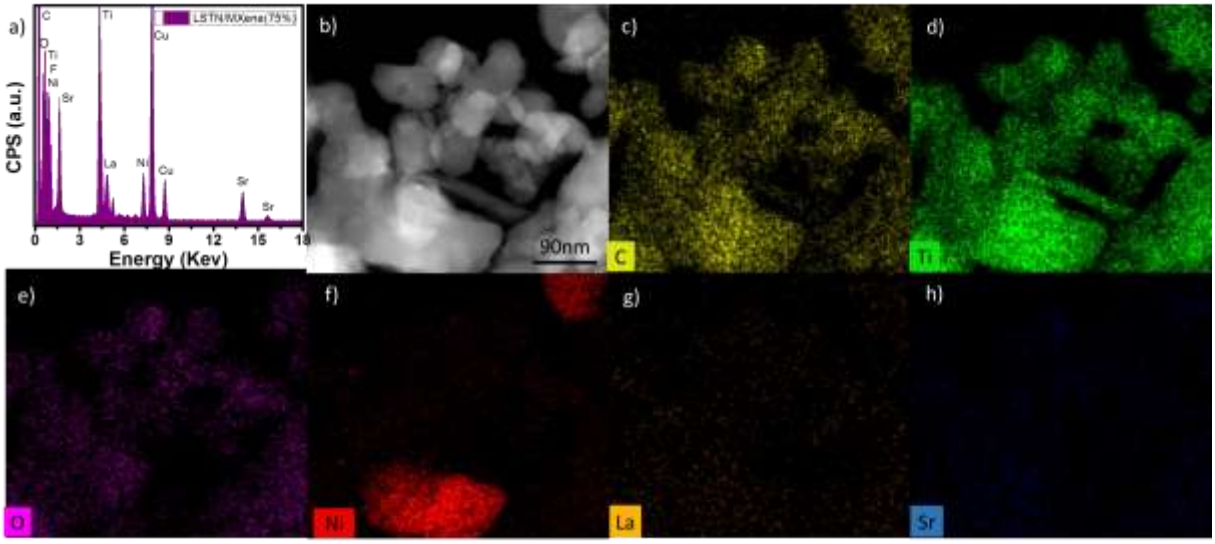

Figure 36: *(a) EDS graph for LSTN/MXene 66.67% showing elemental distribution. (b) TEM image of LSTN/MXene 66.67% composite at 90 nm. (c-h) Elemental mapping of LSTN/MXene 66.67% composite showing presence of C, Ti, O, Ni, La, and Sr.*

4.6 Electrochemical characterization of LSTN/MXene composites

4.6.1 Linear sweep voltammetry results for OER

In order to perform electrochemical measurements, three electrode assembly of the bare Ni foam, Pt mesh and prepared electrocatalysts (LSTN/NF, MXene/NF, LSTN/MXene 50%/NF, LSTN/MXene 66.67%/NF and LSTN 66.67%/MXene/NF) in 1 M KOH solution was used. The OER performance of LSTN/MXene was estimated through the LSV polarization curve. In order to study the influence of heterostructure on Ni substrate, LSTN/NF and MXene/NF were also synthesized and tested under identical conditions for OER performance. As shown in **Fig. 37,** the polarization curve of LSTN/MXene 66.67% for OER shows the oxidation peak at a potential of 1.39 V which corresponds to Ni^{+2}/Ni^{+3} oxidation[162]. The LSTN/NF shows very low activity towards Oxygen evolution

reaction (OER)[163] as compared to hydrogen evolution reaction (HER). Thus, clearly the activity of perovskite LSTN get enhanced by adding MXene. The anodic current density of LSTN/MXene 66.67% increases quickly, when potential is >1.53 V. Linear sweep voltammetry (LSV) reveals a great difference in OER activities for the prepared composites of LSTN/MXene. The doping of perovskite at A-site (Sr) and B-site (Ni) critically improves the bifunctional activity of perovskite. Several oxygen vacancies are created by Sr doping, which is responsible for providing several chances for oxygen ion to diffuse[82]. Moreover, the oxygen vacancies provided by Ni doping that enhanced the catalytic activity can be attributed to several Ni^{3+} on the surface. Still, the OER activity of LSTN is much inferior than Co based perovskites[79]. Therefore, there is a need to improve OER, by preparing hybrid catalysts that can be used for various applications. The addition MXene in electrode material considerably improves the electrochemical performance, which could be attained due to conductive pathways provided by MXene sheets. The conductive MXene opens up proton coupled electron transfer process and thus helps in increasing the redox reaction efficiency[158]. It provides intercalation and deintercalation of OH^- by presenting conductive channels through which fast ion transportation can be achieved across the interface of electrode and electrolyte. The LSTN/MXene 66.67% has shown the highest activity among the prepared catalyst of LSTN/MXene 50% and LSTN 66.67%/MXene.

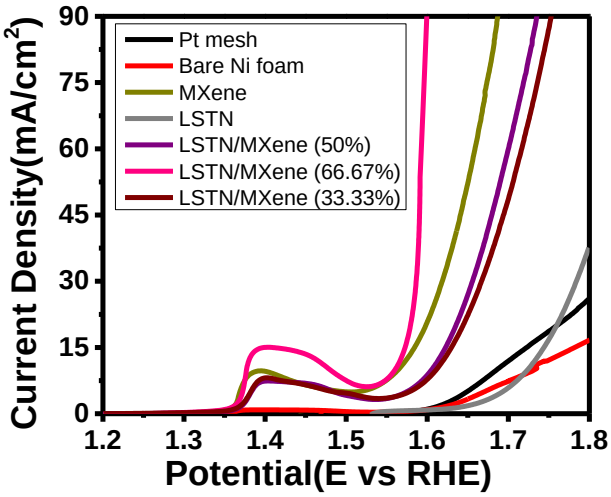

Figure 37: *Comparison of Linear sweep voltammetry curve OER for Pt mesh, Bare Ni foam, MXene, LSTN, LSTN/MXene 50%, LSTN/MXene 66.67% and LSTN 66.67%/MXene at 10 mV s^{-1}.*

Their activity is also assessed by overpotential, which shows that LSTN/MXene 66.67% requires a low overpotential of 330 mV @ 10 mA cm^{-2} current density, which is much less than LSTN (494 mV) and MXene (334 mV) at 10 mA cm^{-2} current density **(Fig. 38(b)).** In addition, the mass activity for LSTN/MXene 66.67% has increased approx. 5 times the MXene. In **Fig. 38(c)**, the mass activity at 1.59 (V vs RHE) for LSTN, MXene, and LSTN/MXene 66.67%, LSTN/MXene 50% and LSTN 66.67% /MXene has found to be 0.69, 12.2, 59.3, 5.63 and 5.2 mA mg^{-1}. The high electrochemical activity of LSTN/MXene 66.67% can also be confirmed by the low Tafel slope of LSTN/MXene 66.67% (44 mV dec^{-1}) as compare to MXene (123 mV dec^{-1}), LSTN/MXene 50% (132 mV dec^{-1}), LSTN 66.67%/MXene (123 mV dec^{-1}) and LSTN (140 mV dec^{-1}) shown in **Fig. 38(a).** The Tafel slope value for LSTN/MXene 66.67% is close 40 mV dec^{-1}, which shows the OER equilibrium attained by one electron electrochemical step along with one electron rate determining step[27].The low Tafel slope value for LSTN/MXene 66.67% shows higher electrocatalytic performance capacity as the rate of this catalyst increases with an increase in potential. A wide variety of adsorbed oxygen species and their interaction with heterostructured catalyst on cation site of transition metal is responsible for this significant behavior[39]. The oxidation of LSTN/MXene occurs by following major steps[164].

$$M + OH^- \leftrightarrow M - OH + e^- \quad (21)$$

$$M - OH + OH^- \leftrightarrow M - O + H_2O + e^- \quad (22)$$

$$M - O + OH^- \leftrightarrow M - OOH + e^- \quad (23)$$

$$M - OOH + OH^- \leftrightarrow M - OO^- + H_2O \quad (24)$$

$$M - OO^- \leftrightarrow M + O_2 + e^- \quad (25)$$

Where M stands for a site on a catalyst surface. The Tafel slope 44 mV dec^{-1} shows that eq. 25 will be rate-determining step, while, peroxide formation (M-O to M-OOH) may lead to weak binding of oxygen, given as rate-limiting step. The binding strength of oxygen with metal sites also controls the reaction kinetics for OER.

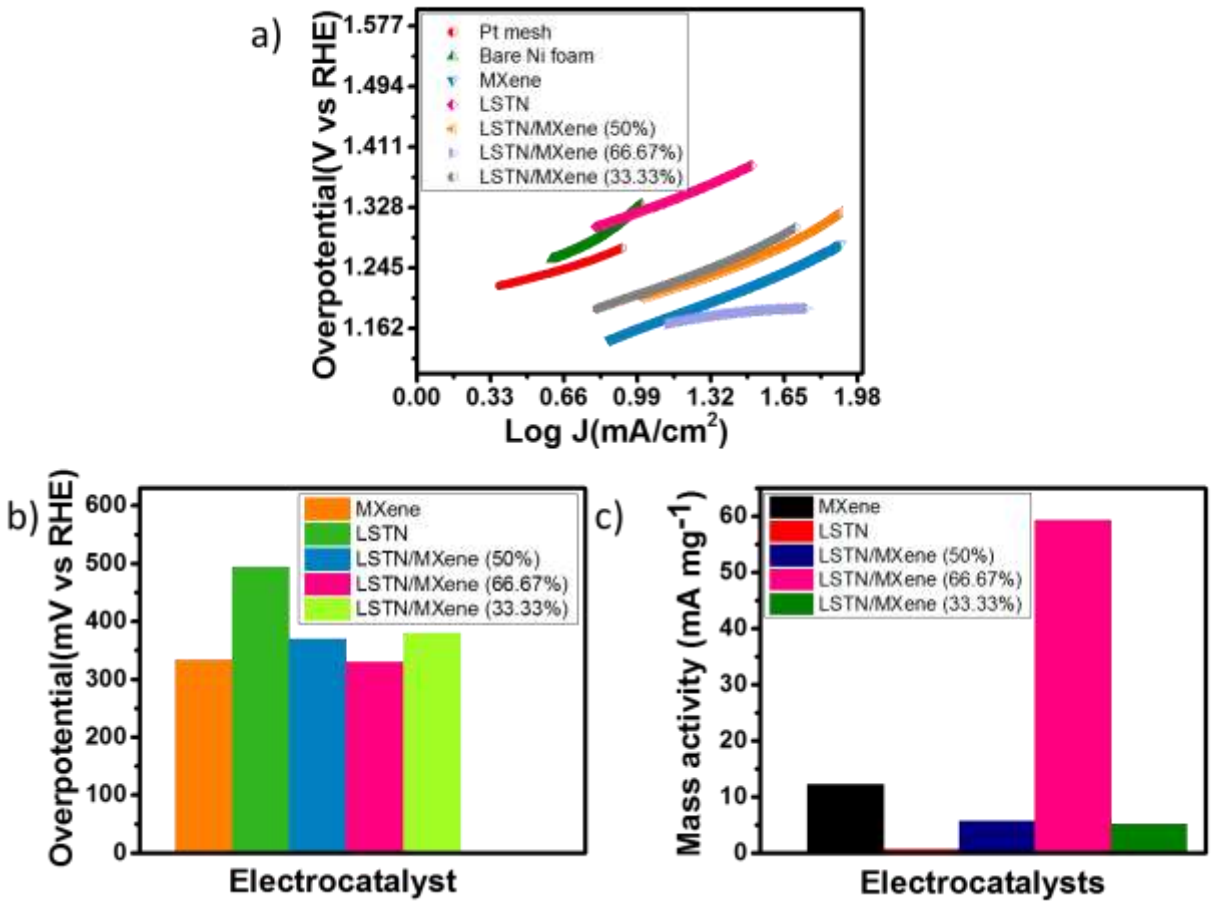

Figure 38: *(a) Corresponding Tafel slopes for Pt mesh, Bare Ni foam, MXene, LSTN, LSTN/MXene 50%, LSTN/MXene 66.67% and LSTN 66.67%/MXene. (b) Overpotential values for MXene, LSTN, LSTN/MXene 50%, LSTN/MXene 66.67% and LSTN 66.67%/MXene. (c) Corresponding Mass* activity of prepared catalysts at 1.59V.

4.6.2 Linear sweep voltammetry results for HER

In order to perform electrochemical measurements, three electrode assembly of the bare Ni foam, Pt mesh and prepared electrocatalysts (LSTN/NF, MXene/NF, LSTN/MXene 50%/NF, LSTN/MXene 66.67%/NF and LSTN 66.67%/MXene/NF) in 1 M KOH solution was used. The OER performance of LSTN/MXene was estimated through the LSV polarization curve. In order to study the influence of heterostructure on Ni substrate, LSTN/NF and MXene/NF were also synthesized and tested under identical conditions for HER performance.

To estimate the electrocatalytic performance of LSTN/MXene 66.67%, we further studied the HER performance of the as-synthesized catalyst. The LSTN catalyst presents good HER activity (comprising superior mass activity as well as fast reaction kinetics)[79]. As we know, the most favorable HER catalyst is Pt/C/NF, the activity of LSTN perovskite need to be further improved, in order to approach the standard activity. But, the MXene addition did not worked effectively for improving HER activity of LSTN perovskite. **Fig. 39(a)** displays comparison of linear sweep voltammetry curve for LSTN, MXene, LSTN/MXene 66.67%, LSTN/MXene 50% and LSTN 66.67%/MXene. The Tafel slope and overpotential value for as synthesized composite are presented in **Fig. 39(c, d)**, which suggests low onset potential for LSTN supported on nickel foam as compare to LSTN/MXene 66.67%. The electrocatalytic activity of pristine MXene nanosheets for HER is poor giving large value of overpotential as compared to LSTN nanoparticles and LSTN/MXene composite. It has been known that surface oxidation has a drastic effect on HER activity of MXene, which extensively reduces the hydrogen coverage and hydrogen adsorption sites[165]. This statement validates a possible reason for the reduced activity of as-prepared composite towards HER. Moreover, the LST perovskite having a surface largely consisting of hydroxy (O-H) helps in promoting the water dissociation, thereby forming a favorable component in LSTN for alkaline HER catalysis[79]. The HER activity of LSTN has thus shown considerable results as compared to its composite with MXene nanolayers, whose activity has been reduced due to slight oxidation of the surface. The HER activity of LSTN/MXene can be further enhanced by optimizing the synthesis technique to allow synergistic interaction among two components and suppressing the oxidization of composite.

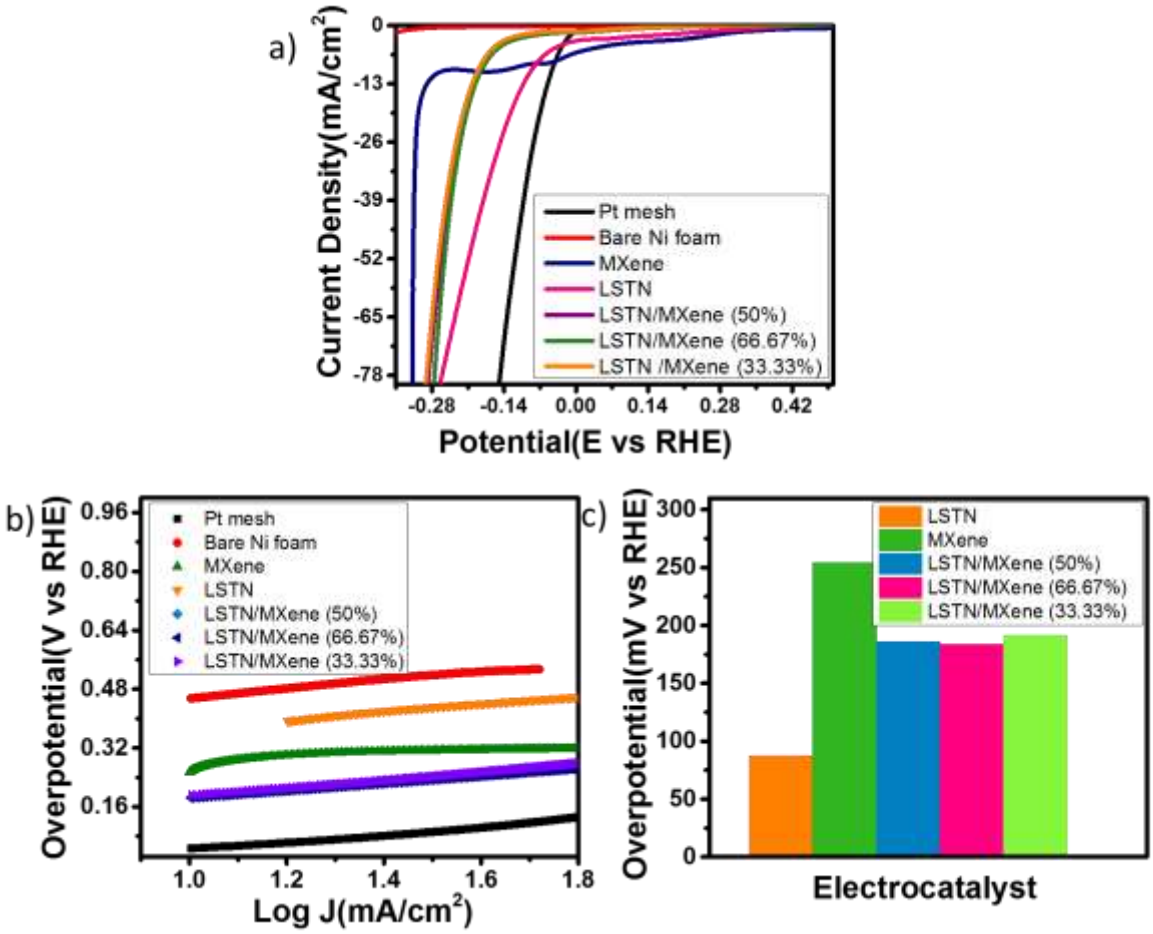

Figure 39: *(a) LSV curve of Pt mesh, bare Ni foam, MXene, LSTN, LSTN/MXene 50%, LSTN/MXene 66.67% and LSTN/MXene 33.33% for HER. (b) Corresponding Tafel plots of prepared catalysts. (c) Overpotential value at 10 mA cm^{-2} current density for LSTN, MXene, LSTN/MXene*50%, LSTN/MXene 66.67%, LSTN/MXene 33.33%.

4.6.3 Cyclic voltammetry

Fig. 40 (a-e) shows the cyclic voltammogram of LSTN/NF, MXene/NF, LSTN/MXene 50%/NF, LSTN/MXene 66.67%/NF, and LSTN 33.33%/MXene/NF over a scan rate of 10 to 50 mVs^{-1} applied potential. The potential range 1-1.6 (V vs RHE) shows a pair of definite redox peaks (corresponding to B-type curves)[147]. The **Fig. 40** sows the CV curves for LSTN, MXene, LSTN/MXene 50%, LSTN/MXene 66.67%, and LSTN/MXene 33.33%. All the CV curves represent pair of redox peaks. The highest current density has been observed of LSTN/MXene 66.67%. The forward scan results in

oxidation of catalyst for oxides and conducting removal of electrons, while the reverse scan undergoes reduction of LSTN/MXene catalyst in a reversable manner. Moreover, the reversibility of electrode material can be defined by the adsorption OH^- at electrode surface. With an increase in scan rate, shape of CV curve does not change, this feature implies to small resistance, high cyclic stability and efficient catalytic performance of electrodes. The diffusion layer resistance decreases gradually by constant increment in scan rate, thereby achieving the higher current densities. Besides, nickel foam shows very low OER activity, therefore, it's contribution towards studied potential range of OER is minimum, it only functions to provide a conductive support to catalyst material[133], [148]. The porosity in nickel foam provides efficient transmission channels, and easiness in departure of oxygen and hydrogen[149].

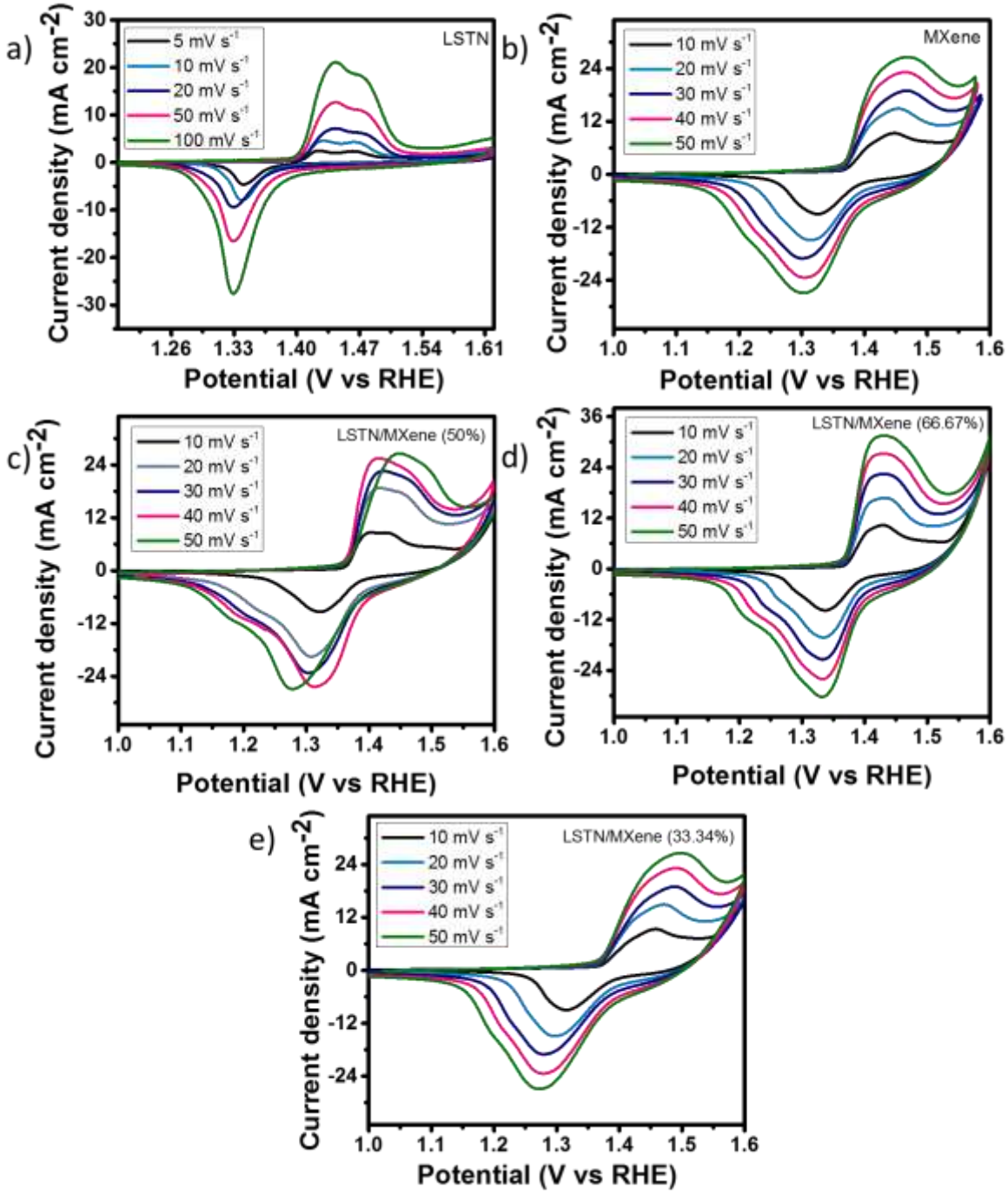

Figure 40: *(a) CV curves at scan rate 5, 10, 20, 50, 100 mV dec^{-1} for LSTN. (b-e) CV curves at scan rate 10, 20, 30, 40, 50 mV s^{-1} for MXene, LSTN/MXene 50%, LSTN/MXene 66.67% and LSTN/MXene 33.33%.*

4.6.4 Stability test

In addition, LSTN/MXene 66.67%/NF was further observed for stability at 100 mA for 20 hrs., **(Fig. 41(a))**. The potential from chronopotentiometry results for nanocomposite has shown the stable behavior, which is achieved by its structural characteristics. The low ion diffusion resistance which is driven by efficient interfacial area between electrode and electrolyte favors quick ion penetration across the widely exposed active sites. This occurs due to activation of synthesized material during chronopotentiometry test. The potential achieved the constant value with potential change of only 0.03 V, which shows a very stable catalyst with high efficiency. The stability of LSTN/MXene 66.67% was also confirmed by undergoing linear sweep voltammetry analysis after performing 1000 cycles, shown in **Fig. 41(b)**. The LSV results were found similar after 1000 cycles to the initial value of LSV. These results make LSTN/MXene 66.67% catalyst quite stable for practical application.

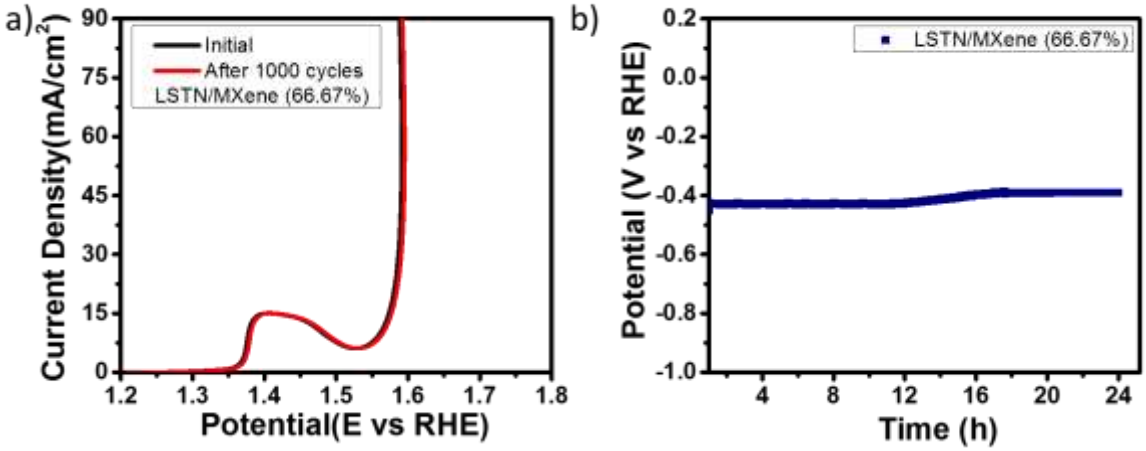

Figure 41: *(a) Comparison of Linear sweep voltammetry curve HER for Pt mesh, Bare Ni foam, MXene, LSTN, LSTN/MXene 50%, LSTN/MXene 66.67% and LSTN 66.67%/MXene. (b) Chronopotentiometry test for LSTN/MXene 66.67% operated for 24 hrs.*

4.6.5 Electrochemical impedance spectroscopy

Furthermore, impedance spectroscopy was used to further study the kinetics of as obtained catalyst **(Fig. 42(a)).** The test was performed in 1 M KOH solution within a

frequency range of 20^5 Hz - 0.1 Hz. The graph inset shows equivalent circuit elements, the ohmic resistance which corresponds to the electrolyte between two electrodes is represented by R_1, where, R_2 represents the charge transfer resistance given as polarization resistance, at the interface among electrode and electrolyte, where, W is named as Warburg impedance. Alongside, the Nyquist plot also shows a semicircle which is associated with polarization resistance. The polarization resistance is caused by faradic reaction occurring at electrode surface. The reduced charge transfer resistance (Rct) has been observed for LSTN/MXene 66.67%/NF which is shown by a small diameter of semicircle indicating the proficient charge transferability[152], [153]. The observed polarization resistance of LSTN/NF is 1.48 Ω and for, LSTN/MXene 66.67%/NF it's 0.1713 Ω, respectively. The electrolyte resistance for the LSTN/NF, MXene/NF, and LSTN/MXene 66.67%/NF was found to be 0.753 Ω, 2.095 Ω, and 0.69 Ω, respectively, shown in **Table 7**.

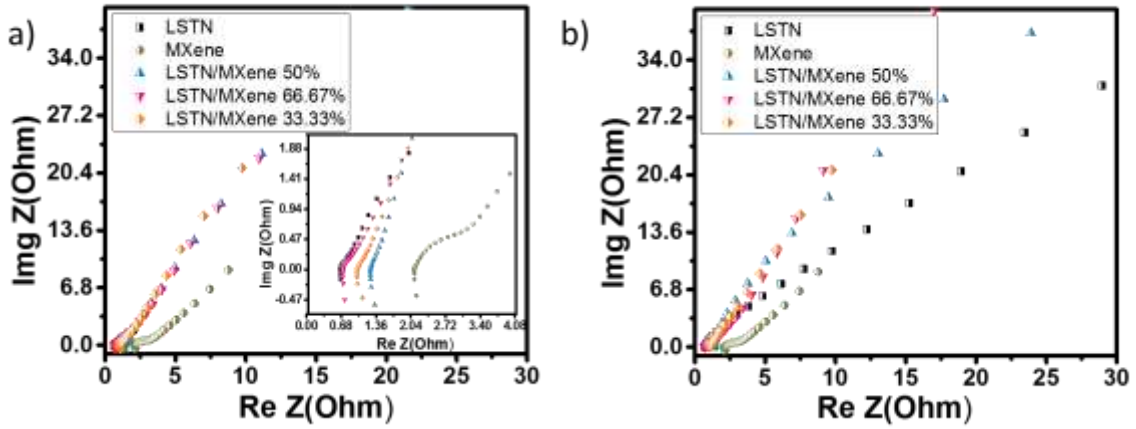

Figure 42: *(a) Nyquist plot for LSTN, MXene, LSTN/MXene 50%, LSTN/MXene 66.67% and LSTN 33.33%/MXene, Inset shows the zoomed image of graph presenting initial values. (b) Z-fitted data of respective catalysts.*

Table 7: *Summary of electrochemical performance of prepared electrodes.*

Catalyst	R_1 (Ω)	R_2 (Ω)	Tafel slope (mV dec^{-1}) OER	Voltage (V) @ 10 mA cm^2 OER
LSTN	0.753	1.48	140	1.704
MXene	2.095	0.774	123	1.564
LSTN/MXene 50%	1.329	0.254	132	1.60
LSTN/MXene 66.67%	0.69	0.1713	44	1.56
LSTN 66.67%/MXene	1.031	0.423	123	1.61

4.6.6 Comparison of results with other catalyst

Table 8*: Comparison of oxygen evolution reaction performance of various transition metal oxide catalysts.*

Catalyst	Electrolyte	Onset potential (V) OER	Ref
LSTN/MXene 66.67%/NF	1 M KOH	1.53	This work
LSTN/MXene 50%/NF	1 M KOH	1.55	This work
LSTN/MXene 33.33%/NF	1 M KOH	1.559	This work
LSTN	1 M KOH	1.583	This work
MXene	1 M KOH	1.535	This work
$LaFeO_3$	1 M KOH	1.61	[47]
$La_{0.2}Sr_{0.8}FeO_{3-\delta}$	1 M KOH	1.54	[82]
$La_{0.5}Sr_{0.5}FeO_{3-\delta}$	1 M KOH	1.58	[82]
$Sr_{0.95}Co_{0.8}Nb_{0.1}Ni_{0.1}O_{3-\delta}$	1 M KOH	1.55	[94]

NiFe-LDH/MXene	1 M KOH	1.465	[158]
Ti_3C_2@$NiCo_2O_4$	1 M KOH	1.54	[162]
Ti_3C_2P	1 M KOH	1.665	[162]
CoNi-ZIF-67@$Ti_3C_2T_x$	0.1 M KOH	1.485	[166]
Black phosphorous quantum dots/ MXene	1 M KOH	1.54	[167]

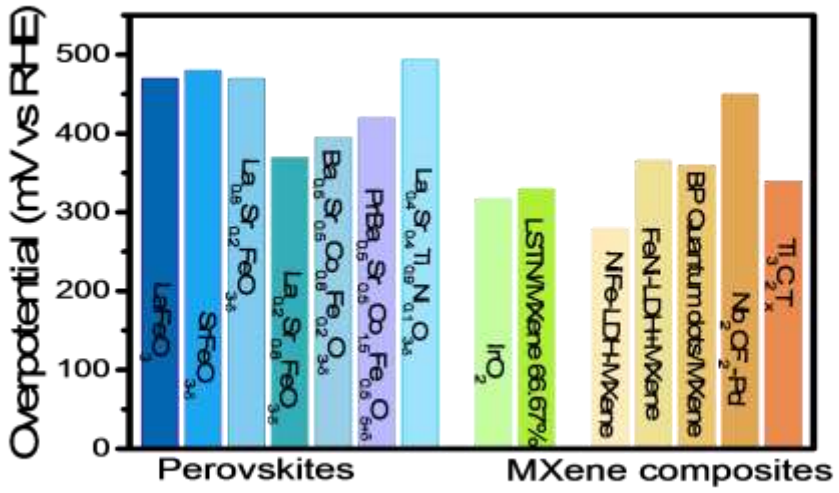

Figure 43: *C*omparison of overpotential between perovskites such as $LaFeO_3$[47], $SrFeO_{3-\delta}$ [82], $La_{0.8}Sr_{0.2}FeO_{3-\delta}$[82], $La_{0.2}Sr_{0.8}FeO_{3-\delta}$[82], $Ba_{0.5}Sr_{0.5}Co_{0.8}Fe_{0.2}O_{3-\delta}$[116], $PrBa_{0.5}Sr_{0.5}Co_{1.5}Fe_{0.5}O_{5+\delta}$[168], $La_{0.4}Sr_{0.4}Ti_{0.9}Ni_{0.1}O_{3-\delta}$[This work], IrO_2[158], and MXene composite, like, LSTN/MXene 66.67% [This work], NiFe-LDH-MXene[158], FeNi-LDH+MXene[27], black phosphorous quantum dots/MXene[167], Nb_2CF_2-Pd[169], $Ti_3C_2T_x$[This work].

Challenges for perovskites as bifunctional catalysts for water splitting

- In contrast to the substantial development of design principles for the improvement in catalytic activity, stability has given much less attention, which is of more concern specifically for device-based applications. Most perovskites undergo amorphism during OER, which results in leaching of A/B-site cations into electrolyte. Like amorphization was found in bulk and over the highly active surface (BSCF)[137], [170], leading to structural transformation from corner sharing octahedra to edge sharing octahedra. It was also found that all the catalysts are not durable during long term usage such as, Nickel and Iron based electrocatalysts.
- Although, the OER/ORR/HER mechanism has been studied widely on perovskite catalyst, but optimization of perovskite catalyst is still difficult due to its complex process. It is necessary to develop the well-defined model perovskite to better interlink the electronic structure and surface electrochemistry of perovskite oxides, which will help to grasp the mechanism of OER/HER/ORR on perovskite oxide surface. Pristine perovskites have some drawbacks related to their stability, limited electromagnetic performance and poor conductivity. To enhance the physical and chemical properties of perovskites, noble metals and rare earth (RE) metals are used as a dopant. Thus, introducing the RE metals having variable valence state and electronic structure results in flexible redox properties and improved electromagnetic characteristics. Moreover, despite the fact that partial substitution at A/B-site cations of perovskite favors in not only increasing the catalytic activity, but it also destabilizes the perovskite. In addition, the synergy effect between the oxide and secondary component needs to be further studied for composite perovskite electrocatalyst. In order to improve the performance of the perovskite catalyst, cathodic and anodic activity, the availability of more exposed active sites or using the appropriate

support material along with the tuning of composition are the major possible resources.

- The conventionally used methods to prepare perovskite electrocatalyst are very hard and require special equipment for large scale production of catalyst. There is a need to carry out such studies that will help to inhibit the perovskite oxides to undergo structural changes during catalysis for practical application.

Conclusions

The thesis report gives a deep insight to progressive developments done in perovskite oxides as an electrocatalyst for OER/HER. The main aim of this work is to find low cost, non-precious metal catalyst showing high catalytic activity and stability. Thus, this demand brought perovskite oxides quite favorable for effective catalytic properties. Perovskite oxides have been researched widely owing to their tuneable properties initiated from flexible crystal structure, with an ability to undergo substitution of A/B-site cation and oxygen defects. It was concluded that the oxygen electrocatalysis is mainly determined by B-site elements, the substitution at A-site as well as the selection of A-site element strongly influences catalytic activity, synergistic effect is achieved on combining two different elements at B-site, and addition of small amount of noble metal greatly enhances catalytic activity.

Although significant work has been done to investigate the application of perovskite materials as electrocatalysts for water splitting, there is still space for further research, especially in the case of hydrogen evolution reaction. Due to the different nature of both HER and OER at the perovskite surface, achieving a higher activity for bifunctionality of perovskites will be challenging. However, it might be possible to achieve the desired activities of the perovskite based bifunctional catalysts by further studies designed to undertake the challenge.

In this regard, we presented a highly active bifunctional 3D heterostructure LSTN@NiMn-LDH arrays supported on NF, which were successfully synthesized by CA/EDTA complexing sol-gel method followed by hydrothermal reaction as a new catalyst for water splitting. The unusual synergistic effect in such a hybrid catalyst is responsible for the efficient electron transfer process. The heterostructure LSTN@NiMn-LDH/NF has shown outstanding activity for both HER and OER, exhibiting 125 mV and 387 mV overpotential at a higher current density of 100 mA cm^{-2}. Moreover, a highly active perovskite nanoparticle interlaced within MXene layers has been synthesized via complexing CA/EDTA sol-gel method, which was followed by sonication with MXene synthesized by HF etching of MAX phase..The future work is based on preparing double perovskites to attain highly exposed active sites and increased ion diffusion. Therefore, a B-site cation doped double perovskite has also been synthesized to achieve high

bifunctional activity. Among STF, STPF-0.1, and STPF-0.2, 2% Pr doping in STF has shown highest activity for OER and HER. The prepared catalyst has provided a new pathway to prepare bifunctional electrocatalyst.

Future recommendations

There is a need for an improved understanding of the OER, ORR and HER mechanism on the perovskite surfaces. The mechanisms published in the literature need extensive validation by carefully designed experiments. On the other hand, the perovskite catalyst design strategies need to be optimized. By combining the insights from the reaction mechanisms and optimized catalyst design, it may be possible to quickly develop the active perovskite HER catalysts. The dependence on very expensive and state-of-the-art characterization tools limits further exploration of mechanisms. Therefore, the development of new materials may create new structures and therefore new functionalities, among which some have been predicted theoretically by using DFT analysis. Similarly, for the industrial application point of view, due to the lower HER activity of the perovskite catalyst, there might be possibility to explore the application of hybrid catalysts i.e. separate catalyst for both OER and HER.

The operational stability of the perovskite catalysts is also one of the main hurdles toward widespread application of the perovskite electrocatalysts. In the current literature, as we have discussed at length, the reported stability tests involve short-term electrochemical testing. During the initial hours of the operation, the changes at the electrode surfaces are very dynamic. For developing a stable and commercially viable catalyst, long-term electrochemical stability experiments might be designed to elucidate the reasons for performance degradation of the perovskites electrocatalysts. Moreover, in research laboratories stability tests conditions do not match with the industrial requirements. For example, in actual electrolyser, there is possibility of operation at different voltage due and the catalyst stability for operation at multiple voltages may also be investigated to understand the long-term operability of the perovskite electrocatalysts. Therefore, application-oriented investigations should be carried out more extensively for longer testing hours at the operating conditions more of industrial interest, for example, at current density range of 0.5 – 2.0 A cm^{-2} and higher temperature (80 °C). It is speculated that a perovskite electrocatalysts based operative water electrolyzer can be expected sooner if the combination of inputs from both the fundamental and applied research is employed.

A lot of work can be done in this area to commercialize catalysts.

1. Double perovskites, and triple perovskites are having great potential to be explored in this area.

2. Insitu synthesis of perovskite composites with MoS_2 will result in highly active HER catalyst.

3. Regeneration of catalyst is also an effective area to work in this field.

References

[1] J. A. Turner, "Sustainable hydrogen production," *Science (80-.).*, vol. 305, no. 5686, pp. 972–974, 2004.

[2] T. R. Cook, "D. K, Dogutan, SY Reece, Y. Surendranath, TS Teets, DG Nocera," *Sol. energy Supply storage Leg. nonlegacy worlds. Chem. Rev*, vol. 110, pp. 6474–6502, 2010.

[3] N. S. Lewis and D. G. Nocera, "Powering the planet: Chemical challenges in solar energy utilization," *Proc. Natl. Acad. Sci.*, vol. 103, no. 43, pp. 15729 LP – 15735, Oct. 2006.

[4] Z. Wei, F. Colin, K. Jens, and F. Thomas, "Combining theory and experiment in electrocatalysis : Insights into materials design Combining Theory and Experiment in Electrocatalysis : Insights into Materials Design," 2017.

[5] "The Outlook for Energy: A View to 2040."

[6] J. M. Campos-Martin, G. Blanco-Brieva, and J. L. G. Fierro, "Hydrogen Peroxide Synthesis: An Outlook beyond the Anthraquinone Process," *Angew. Chemie Int. Ed.*, vol. 45, no. 42, pp. 6962–6984, Oct. 2006.

[7] H. Ding, C. Luo, X. Li, D. Cao, Q. Shen, and L. Zhang, "Development of BaSrCo-based perovskite for chemical-looping steam methane reforming: A study on synergistic effects of A-site elements and CeO2 support," *Fuel*, vol. 253, pp. 311–319, 2019.

[8] R. Z. Batteries, "A Highly E ffi cient and Robust Cation Ordered," pp. 11594–11601, 2017.

[9] F. Song *et al.*, "Transition Metal Oxides as Electrocatalysts for the Oxygen Evolution Reaction in Alkaline Solutions: An Application-Inspired Renaissance," *J. Am. Chem. Soc.*, vol. 140, no. 25, pp. 7748–7759, Jun. 2018.

[10] J. Wang, W. Cui, Q. Liu, Z. Xing, A. M. Asiri, and X. Sun, "Recent Progress in Cobalt-Based Heterogeneous Catalysts for Electrochemical Water Splitting," *Adv.*

Mater., vol. 28, no. 2, pp. 215–230, Jan. 2016.

[11] J. Yu, Q. Wang, D. O'Hare, and L. Sun, "Preparation of two dimensional layered double hydroxide nanosheets and their applications," *Chem. Soc. Rev.*, vol. 46, no. 19, pp. 5950–5974, 2017.

[12] L. Lv, Z. Yang, K. Chen, C. Wang, and Y. Xiong, "Electrocatalysts: 2D Layered Double Hydroxides for Oxygen Evolution Reaction: From Fundamental Design to Application (Adv. Energy Mater. 17/2019)," *Adv. Energy Mater.*, vol. 9, no. 17, p. 1970057, May 2019.

[13] S. Gupta, W. Kellogg, H. Xu, X. Liu, J. Cho, and G. Wu, "Bifunctional Perovskite Oxide Catalysts for Oxygen Reduction and Evolution in Alkaline Media," pp. 10–21, 2016.

[14] M. Gong and H. Dai, "A mini review of NiFe-based materials as highly active oxygen evolution reaction electrocatalysts," *Nano Res.*, vol. 8, no. 1, pp. 23–39, 2015.

[15] N.-T. Suen, S.-F. Hung, Q. Quan, N. Zhang, Y.-J. Xu, and H. M. Chen, "Electrocatalysis for the oxygen evolution reaction: recent development and future perspectives," *Chem. Soc. Rev.*, vol. 46, no. 2, pp. 337–365, 2017.

[16] H. Osgood, D. SV, H. Xu, J. Cho, and G. Wu, "Transition metal (Fe, Co, Ni, and Mn) oxides for oxygen reduction and evolution bifunctional catalysts in alkaline media," *Nano Today*, vol. 11, no. 5, pp. 601–625, 2016.

[17] M. Tahir *et al.*, "Electrocatalytic oxygen evolution reaction for energy conversion and storage: A comprehensive review," *Nano Energy*, vol. 37, pp. 136–157, 2017.

[18] T. Liu *et al.*, "Enhanced Electrocatalysis for Energy-Efficient Hydrogen Production over CoP Catalyst with Nonelectroactive Zn as a Promoter," *Adv. Energy Mater.*, vol. 7, no. 15, p. 1700020, Aug. 2017.

[19] C. Xiong *et al.*, "Nitrogen-doped carbon nanotubes as catalysts for oxygen reduction reaction," *J. Power Sources*, vol. 215, pp. 216–220, 2012.

[20] J. Bao *et al.*, "Two-dimensional Mn-Co LDH/graphene composite towards high-performance water splitting," *Catalysts*, vol. 8, no. 9, 2018.

[21] Y. Wang, D. Yan, S. El Hankari, Y. Zou, and S. Wang, "Recent Progress on Layered Double Hydroxides and Their Derivatives for Electrocatalytic Water Splitting," *Adv. Sci.*, vol. 5, no. 8, 2018.

[22] S. Liu *et al.*, "The synergistic effect of Ni promoter on Mo-S/CNT catalyst towards hydrodesulfurization and hydrogen evolution reactions," *Fuel*, vol. 232, pp. 36–44, 2018.

[23] S. Hussain *et al.*, "WS(1−x) Sex nanoparticles decorated three-dimensional graphene on nickel foam: A robust and highly efficient electrocatalyst for the hydrogen evolution reaction," *Nanomaterials*, vol. 8, no. 11, pp. 1–12, 2018.

[24] X. Zhang, Q. Zhang, Y. Sun, and J. Guo, "Hybrid catalyst of MoS2-CoMo2S4 on graphene for robust electrochemical hydrogen evolution," *Fuel*, vol. 184, pp. 559–564, 2016.

[25] Y. Hou, M. R. Lohe, J. Zhang, S. Liu, X. Zhuang, and X. Feng, "Vertically Oriented Cobalt Selenide / NiFe Layered-Double-Hydroxide Energy & Environmental Science," *Energy Environ. Sci.*, vol. 9, no. June, pp. 478–483, 2016.

[26] Z. Cai, X. Bu, P. Wang, J. C. Ho, J. Yang, and X. Wang, "Recent advances in layered double hydroxide electrocatalysts for the oxygen evolution reaction," *J. Mater. Chem. A*, vol. 7, no. 10, pp. 5069–5089, 2019.

[27] M. Yu, S. Zhou, Z. Wang, J. Zhao, and J. Qiu, "Boosting electrocatalytic oxygen evolution by synergistically coupling layered double hydroxide with MXene," *Nano Energy*, vol. 44, no. November 2017, pp. 181–190, 2018.

[28] T. Kuila, S. Bose, A. K. Mishra, P. Khanra, N. H. Kim, and J. H. Lee, "Chemical functionalization of graphene and its applications," *Prog. Mater. Sci.*, vol. 57, no. 7, pp. 1061–1105, 2012.

[29] M. Naguib, V. N. Mochalin, M. W. Barsoum, and Y. Gogotsi, "25th Anniversary

Article: MXenes: A New Family of Two-Dimensional Materials," *Adv. Mater.*, vol. 26, no. 7, pp. 992–1005, Feb. 2014.

[30] M. Naguib *et al.*, "Two-Dimensional Nanocrystals Produced by Exfoliation of Ti3AlC2," *Adv. Mater.*, vol. 23, no. 37, pp. 4248–4253, Oct. 2011.

[31] M. Ghidiu, M. R. Lukatskaya, M.-Q. Zhao, Y. Gogotsi, and M. W. Barsoum, "Conductive two-dimensional titanium carbide 'clay' with high volumetric capacitance.," *Nature*, vol. 516, no. 7529, pp. 78–81, Dec. 2014.

[32] M. R. Lukatskaya *et al.*, "Cation Intercalation and High Volumetric Capacitance of Two-Dimensional Titanium Carbide," *Science (80-.).*, vol. 341, no. 6153, pp. 1502 LP – 1505, Sep. 2013.

[33] J.-C. Lei, X. Zhang, and Z. Zhou, "Recent advances in MXene: Preparation, properties, and applications," *Front. Phys.*, vol. 10, no. 3, pp. 276–286, 2015.

[34] T. Y. Ma, J. L. Cao, M. Jaroniec, and S. Z. Qiao, "Interacting Carbon Nitride and Titanium Carbide Nanosheets for High-Performance Oxygen Evolution.," *Angew. Chem. Int. Ed. Engl.*, vol. 55, no. 3, pp. 1138–1142, Jan. 2016.

[35] N. H. Attanayake *et al.*, "Vertically aligned MoS2 on Ti3C2 (MXene) as an improved HER catalyst," *J. Mater. Chem. A*, vol. 6, no. 35, pp. 16882–16889, 2018.

[36] L. Zhao *et al.*, "Interdiffusion Reaction-Assisted Hybridization of Two-Dimensional Metal–Organic Frameworks and Ti3C2Tx Nanosheets for Electrocatalytic Oxygen Evolution," *ACS Nano*, vol. 11, no. 6, pp. 5800–5807, Jun. 2017.

[37] S. Chen, Y. Xiang, W. Xu, and C. Peng, "A novel MnO 2 /MXene composite prepared by electrostatic self-assembly and its use as an electrode for enhanced supercapacitive performance," *Inorg. Chem. Front.*, vol. 6, no. 1, pp. 199–208, 2019.

[38] A. Tariq, S. I. Ali, D. Akinwande, and S. Rizwan, "Efficient Visible-Light Photocatalysis of 2D-MXene Nanohybrids with Gd3+- and Sn4+-Codoped

Bismuth Ferrite," *ACS Omega*, vol. 3, no. 10, pp. 13828–13836, 2018.

[39] X. Zhang, Z. Lai, Q. Ma, and H. Zhang, "Novel structured transition metal dichalcogenide nanosheets," *Chem. Soc. Rev.*, vol. 47, no. 9, pp. 3301–3338, 2018.

[40] F. Geng, "Coupling Molecularly Ultrathin Sheets of NiFe-Layered Double Hydroxide on NiCo 2 O 4 Nanowire Arrays for Highly E ffi cient Overall Water-Splitting Activity," 2017.

[41] J. Zhang *et al.*, "Overall Water Splitting Interface Engineering of MoS 2 / Ni 3 S 2 Heterostructures for Highly Enhanced Electrochemical Overall-Water-Splitting Activity," pp. 6702–6707, 2016.

[42] T. Ouyang, Y. Ye, C. Wu, K. Xiao, and Z. Liu, "Water Splitting Very Important Paper Heterostructures Composed of N-Doped Carbon Nanotubes Encapsulating Cobalt and b -Mo 2 C Nanoparticles as Bifunctional Electrodes for Water Splitting," pp. 4923–4928, 2019.

[43] M. Gong *et al.*, "An advanced Ni-Fe layered double hydroxide electrocatalyst for water oxidation," *J. Am. Chem. Soc.*, vol. 135, no. 23, pp. 8452–8455, 2013.

[44] "www.advenergymat.de," vol. 7, no. 18, p. 2017, 2017.

[45] H. Tanaka and M. Misono, "Advances in designing perovskite catalysts," *Curr. Opin. Solid State Mater. Sci.*, vol. 5, no. 5, pp. 381–387, 2001.

[46] J. Xu, C. Chen, Z. Han, Y. Yang, J. Li, and Q. Deng, "Recent advances in oxygen electrocatalysts based on perovskite oxides," *Nanomaterials*, vol. 9, no. 8, 2019.

[47] J. Dai *et al.*, "Enabling High and Stable Electrocatalytic Activity of Iron-Based Perovskite Oxides for Water Splitting by Combined Bulk Doping and Morphology Designing," *Adv. Mater. INTERFACES*, no. November, 2018.

[48] W. G. Hardin *et al.*, "Tuning the electrocatalytic activity of perovskites through active site variation and support interactions," *Chem. Mater.*, vol. 26, no. 11, pp. 3368–3376, 2014.

[49] W. G. Hardin, D. A. Slanac, X. Wang, S. Dai, K. P. Johnston, and K. J. Stevenson,

"Highly active, nonprecious metal perovskite electrocatalysts for bifunctional metal–air battery electrodes," *J. Phys. Chem. Lett.*, vol. 4, no. 8, pp. 1254–1259, 2013.

[50] J. T. Mefford, W. G. Hardin, S. Dai, K. P. Johnston, and K. J. Stevenson, "Anion charge storage through oxygen intercalation in LaMnO 3 perovskite pseudocapacitor electrodes," *Nat. Mater.*, vol. 13, no. 7, p. 726, 2014.

[51] M. Risch, K. A. Stoerzinger, S. Maruyama, W. T. Hong, I. Takeuchi, and Y. Shao-Horn, "La0. 8Sr0. 2MnO3− δ decorated with Ba0. 5Sr0. 5Co0. 8Fe0. 2O3− δ: a bifunctional surface for oxygen electrocatalysis with enhanced stability and activity," *J. Am. Chem. Soc.*, vol. 136, no. 14, pp. 5229–5232, 2014.

[52] J. Suntivich, H. A. Gasteiger, N. Yabuuchi, and Y. Shao-Horn, "Electrocatalytic measurement methodology of oxide catalysts using a thin-film rotating disk electrode," *J. Electrochem. Soc.*, vol. 157, no. 8, pp. B1263–B1268, 2010.

[53] H. Zhu, P. Zhang, and S. Dai, "Recent advances of lanthanum-based perovskite oxides for catalysis," *ACS Catal.*, vol. 5, no. 11, pp. 6370–6385, 2015.

[54] K. A. Stoerzinger *et al.*, "Oxygen electrocatalysis on (001)-oriented manganese perovskite films: Mn valency and charge transfer at the nanoscale," *Energy Environ. Sci.*, vol. 6, no. 5, pp. 1582–1588, 2013.

[55] J. Miao *et al.*, "Boosting performance of lanthanide magnetism perovskite for advanced oxidation through lattice doping with catalytically inert element," *Chem. Eng. J.*, vol. 355, no. 5, pp. 721–730, 2019.

[56] N. S. Arul, *Materials Horizons : From Nature to Nanomaterials Revolution of Perovskite*. .

[57] X. Zou and Y. Zhang, "Noble metal-free hydrogen evolution catalysts for water splitting," *Chem. Soc. Rev.*, vol. 44, no. 15, pp. 5148–5180, 2015.

[58] A. Lasia, "Hydrogen evolution reaction," *Handb. fuel cells*, 2010.

[59] O. Diaz-Morales, F. Calle-Vallejo, C. de Munck, and M. T. M. Koper,

"Electrochemical water splitting by gold: evidence for an oxide decomposition mechanism," *Chem. Sci.*, vol. 4, no. 6, pp. 2334–2343, 2013.

[60] Z.-L. Wang, D. Xu, J.-J. Xu, and X.-B. Zhang, "Oxygen electrocatalysts in metal–air batteries: from aqueous to nonaqueous electrolytes," *Chem. Soc. Rev.*, vol. 43, no. 22, pp. 7746–7786, 2014.

[61] J. HORIUTI, A. MATSUDA, M. ENYO, and H. KITA, "THE MECHANISM OF THE HYDROGEN EVOLUTION REACTION," in *Electrochemistry*, J. A. FRIEND and F. B. T.-E. GUTMANN, Eds. Pergamon, 1965, pp. 750–779.

[62] A. K. M. S. Huq, "PLATINUM SILVER AND TUNGSTEN SURFACES I N ACID SOLUTIONS t," *J. Phys. Chem.*, vol. 61, no. 6, pp. 879–886, 1957.

[63] X. Xu, Y. Chen, W. Zhou, Z. Zhu, C. Su, and M. Liu, "A Perovskite Electrocatalyst for Efficient Hydrogen Evolution Reaction," no. 5, 2016.

[64] J. D. Benck, T. R. Hellstern, J. Kibsgaard, P. Chakthranont, and T. F. Jaramillo, "Catalyzing the Hydrogen Evolution Reaction (HER) with Molybdenum Sulfide Nanomaterials," *ACS Catal.*, vol. 4, no. 11, pp. 3957–3971, Nov. 2014.

[65] R. Parsons, "The rate of electrolytic hydrogen evolution and the heat of adsorption of hydrogen," *Trans. Faraday Soc.*, vol. 54, no. 0, pp. 1053–1063, 1958.

[66] S. Trasatti, "Electrocatalysis by oxides—attempt at a unifying approach," *J. Electroanal. Chem. Interfacial Electrochem.*, vol. 111, no. 1, pp. 125–131, 1980.

[67] S. Trasatti, "Electrocatalysis in the anodic evolution of oxygen and chlorine," *Electrochim. Acta*, vol. 29, no. 11, pp. 1503–1512, 1984.

[68] J. O'M. Bockris, T. Otagawa, and V. Young, "Solid state surface studies of the electrocatalysis of oxygen evolution on perovskites," *J. Electroanal. Chem.*, vol. 150, no. 1–2, pp. 633–643, 1983.

[69] J. O. M. Bockris and T. Otagawa, "Mechanism of Oxygen Evolution on Perovskites," *J. Phys. chemsitry*, vol. 79, no. 32, pp. 2960–2971, 1983.

[70] I. C. Man *et al.*, "Universality in Oxygen Evolution Electrocatalysis on Oxide

Surfaces," *ChemCatChem*, vol. 3, no. 7, pp. 1159–1165, Jul. 2011.

[71] D. A. Kuznetsov *et al.*, "Tuning Redox Transitions via Inductive Effect in Metal Oxides and Complexes, and Implications in Oxygen Electrocatalysis," *Joule*, vol. 2, no. 2, pp. 225–244, 2018.

[72] J. Suntivich, H. A. Gasteiger, N. Yabuuchi, H. Nakanishi, J. B. Goodenough, and Y. Shao-Horn, "Erratum: Design principles for oxygen-reduction activity on perovskite oxide catalysts for fuel cells and metal–air batteries," *Nat. Chem.*, vol. 3, no. 8, p. 647, 2011.

[73] J. Suntivich, "A Perovskite Oxide Optimized for," *Science (80-.).*, vol. 334, no. 2011, 2012.

[74] J. Suntivich, K. J. May, H. A. Gasteiger, J. B. Goodenough, and Y. Shao-Horn, "A perovskite oxide optimized for oxygen evolution catalysis from molecular orbital principles," *Science (80-.).*, vol. 334, no. 6061, pp. 1383–1385, 2011.

[75] J. Rossmeisl, A. Logadottir, and J. K. Nørskov, "Electrolysis of water on (oxidized) metal surfaces," *Chem. Phys.*, vol. 319, no. 1, pp. 178–184, 2005.

[76] J. K. Nørskov *et al.*, "Origin of the Overpotential for Oxygen Reduction at a Fuel-Cell Cathode," *J. Phys. Chem. B*, vol. 108, no. 46, pp. 17886–17892, Nov. 2004.

[77] J. Rossmeisl, Z. W. Qu, H. Zhu, G. J. Kroes, and J. K. Nørskov, "Electrolysis of water on oxide surfaces," *J. Electroanal. Chem.*, vol. 607, no. 1–2, pp. 83–89, 2007.

[78] C. Jin, X. Cao, F. Lu, Z. Yang, and R. Yang, "perovskite as bifunctional catalyst in alkaline media," *Int. J. Hydrogen Energy*, vol. 38, no. 25, pp. 10389–10393, 2013.

[79] Y. Zhu, J. Dai, W. Zhou, Y. Zhong, H. Wang, and Z. Shao, "Synergistically enhanced hydrogen evolution electrocatalysis by in situ exsolution of metallic nanoparticles on perovskites," *J. Mater. Chem. A*, vol. 6, no. 28, pp. 13582–13587, 2018.

[80] J. T. Mefford *et al.*, "Water electrolysis on La 1," 2016.

[81] X. Rong, J. Parolin, and A. M. Kolpak, “A Fundamental Relationship between Reaction Mechanism and Stability in Metal Oxide Catalysts for Oxygen Evolution,” *ACS Catal.*, vol. 6, no. 2, pp. 1153–1158, Feb. 2016.

[82] S. X. She *et al.*, “ocatalysts in Alkaline Media A Systematic Study of Oxygen Evolution Activity and Stability on La 1-x Sr x FeO 3-δ Perovskite Electrocatalysts in AlkalineA Systematic Study of Oxygen Evolution Activity and Stability on La1-xSrxFeO3- # Perovskite Electr Med,” *Appl. Mater. Interfaces*, 2018.

[83] C. Jin, X. Cao, L. Zhang, C. Zhang, and R. Yang, “Preparation and electrochemical properties of urchin-like La 0 . 8 Sr 0 . 2 MnO 3 perovskite oxide as a bifunctional catalyst for oxygen reduction and oxygen evolution reaction,” *J. Power Sources*, vol. 241, pp. 225–230, 2013.

[84] J. Tulloch and S. W. Donne, “Activity of perovskite La 1 − x Sr x MnO 3 catalysts towards oxygen reduction in alkaline electrolytes,” *J. Power Sources*, vol. 188, pp. 359–366, 2009.

[85] Y. Duan *et al.*, “Tailoring the Co 3d-O 2p covalency in LaCoO3 by Fe substitution to promote oxygen evolution reaction,” *Chem. Mater.*, vol. 29, no. 24, pp. 10534–10541, 2017.

[86] S. K. Tiwari, S. P. Singh, and R. N. Singh, “Effects of Ni , Fe , Cu , and Cr Substitutions for Co in La08Sr02CoO3 on Electrocatalytic Properties for Oxygen Evolution,” *J Electrochem. Soc*, vol. 143, no. 5, pp. 1505–1510, 1996.

[87] Y. Lee, A. Grimaud, and Y. Shao-horn, “In fl uence of Oxygen Evolution during Water Oxidation on the Surface of Perovskite Oxide Catalysts,” *J. Phys. Chem. Lett.*, 2012.

[88] Y. Chang, Y. Chang, P. Wu, C. Wu, and P. Lin, “for Oxygen Reduction Reaction in an Alkaline Electrolyte (a) (b) JCPDS-36-1389,” *J. Electrochem. Soc.*, vol. 157, pp. 900–905, 2010.

[89] Y. Zhu, J. Sunarso, W. Zhou, and Z. Shao, “New phosphorus-doped perovskite

oxide as an oxygen reduction reaction electrocatalyst in an alkaline solution," *Chem. - A Eur. J.*, no. February, 2018.

[90] Y. Zhu, W. Zhou, J. Sunarso, Y. Zhong, and Z. Shao, "Phosphorus-Doped Perovskite Oxide as Highly Efficient Water Oxidation Electrocatalyst in Alkaline Solution," *Adv. Funct. Mater.*, vol. 26, no. 32, pp. 5862–5872, Aug. 2016.

[91] H. and N. C. B.-S.-O. D. P. C. for E. O. E. R. Sun, G. Chen, J. Sunarso, J. Dai, W. Zhou, and Z. Shao, "Molybdenum and Niobium Codoped B-Site-Ordered Double Perovskite Catalyst for Efficient Oxygen Evolution Reaction," *ACS Appl. Mater. Interfaces*, vol. 10, no. 20, pp. 16939–16942, 2018.

[92] X. Xu, Y. Chen, W. Zhou, Y. Zhong, D. Guan, and Z. Shao, "Earth-Abundant Silicon for Facilitating Water Oxidation over Iron-Based Perovskite Electrocatalyst," *Adv. Mater. INTERFACES*, vol. 1701693, pp. 1–7, 2018.

[93] Y. Zhu, W. Zhou, J. Yu, Y. Chen, M. Liu, and Z. Shao, "Enhancing Electrocatalytic Activity of Perovskite Oxides by Tuning Cation Deficiency for Oxygen Reduction and Evolution Reactions," *Chem. Mater.*, vol. 28, no. 6, pp. 1691–1697, 2016.

[94] Q. A. Islam, R. Majee, and S. Bhattacharyya, "Bimetallic nanoparticle decorated perovskite oxide for state-of-the-art trifunctional electrocatalysis," *J. Mater. Chem. A*, vol. 7, no. 33, pp. 19453–19464, 2019.

[95] H. Liu, X. Ding, L. Wang, D. Ding, S. Zhang, and G. Yuan, "Cation deficiency design: A simple and efficient strategy for promoting oxygen evolution reaction activity of perovskite electrocatalyst," *Electrochim. Acta*, vol. 259, no. 51362012, pp. 1004–1010, 2018.

[96] M. Yuasa, G. Sakai, K. Shimanoe, Y. Teraoka, and N. Yamazoe, "Reverse Micelle-Based Preparation of Carbon-Supported La 1 À x Sr x Mn 1 À y Fe y O 3 ¿ □ for Oxygen Reduction Electrode," *J. Electrochem. Soc.*, pp. 1690–1695, 2004.

[97] R. N. Singh, J. P. Singh, and A. Singh, "Electrocatalytic properties of new spinel-type MMoO4 (M= Fe, Co and Ni) electrodes for oxygen evolution in alkaline

solutions," *Int. J. Hydrogen Energy*, vol. 33, no. 16, pp. 4260–4264, 2008.

[98] R. N. Singh, M. Kumar, and A. S. K. Sinha, "Novel FexCr2− x (MoO4) 3 electrocatalysts for oxygen evolution reaction," *Int. J. Hydrogen Energy*, vol. 37, no. 20, pp. 15117–15124, 2012.

[99] W. Zhou and J. Sunarso, "Enhancing Bi-functional electrocatalytic activity of perovskite by temperature shock: A case study of LaNiO3-δ," *J. Phys. Chem. Lett.*, vol. 4, no. 17, pp. 2982–2988, 2013.

[100] J. Du, T. Zhang, F. Cheng, W. Chu, Z. Wu, and J. Chen, "Nonstoichiometric Perovskite CaMnO3−δ for Oxygen Electrocatalysis with High Activity," *Inorg. Chem.*, 2014.

[101] J. Kim, X. Yin, K. Tsao, S. Fang, and H. Yang, "Ca 2 Mn 2 O 5 as Oxygen-De fi cient Perovskite Electrocatalyst for Oxygen Evolution Reaction," *J. Am. Chem. Soc.*, vol. 136, pp. 14646–14649, 2014.

[102] C. Chen *et al.*, "Oxygen-de fi cient BaTiO 3 À x perovskite as an ef fi cient bifunctional oxygen electrocatalyst," pp. 423–432, 2015.

[103] Z. Wang *et al.*, "Nickel-doped La Sr Mn Ni O nanoparticles containing abundant oxygen vacancies as an optimized bifunctional catalyst for oxygen cathode in rechargeable lithium-air batteries abundant oxygen vacancies as an optimized bifunctional catalyst for oxygen cathode," *Appl. Mater. Interfaces*, 2016.

[104] J. Tong, R. M. Richards, O. Hayre, and S. Pylypenko, "Synthesis of high surface area CaxLa(1−x)Al(1−x)MnxO(3−δ) perovskite oxides for oxygen reduction electrocatalysis in alkaline media†," *Catal. Sci. Technol.*, 2016.

[105] B.-Q. Li, Z.-J. Xia, B. Zhang, C. Tang, H.-F. Wang, and Q. Zhang, "Regulating p-block metals in perovskite nanodots for efficient electrocatalytic water oxidation," *Nat. Commun.*, vol. 8, no. 1, p. 934, 2017.

[106] G. Chen *et al.*, "An Amorphous Nickel – Iron-Based Electrocatalyst with Unusual Local Structures for Ultrafast Oxygen Evolution Reaction," *Adv. Mater.*, vol. 1900883, pp. 1–7, 2019.

[107] Y. Zhu *et al.*, "Unusual synergistic effect in layered Ruddlesden − Popper oxide enables ultrafast hydrogen evolution," *Nat. Commun.*, pp. 1–9, 2019.

[108] Y. Zhu, W. Zhou, Y. Zhong, Y. Bu, X. Chen, and Q. Zhong, "A Perovskite Nanorod as Bifunctional Electrocatalyst for Overall Water Splitting," *Adv. Energy Mater.*, no. December 2017, 2016.

[109] A. C. Tavares *et al.*, "Perovskite-Type Catalysts Prepared by Nanocasting: Effect of Metal Silicates on the Electrocatalytic Activity toward Oxygen Evolution and Reduction Reactions," *ACS Appl. Energy Mater.*, vol. 1, no. 6, pp. 2565–2575, 2018.

[110] Y. Bu, H. Jang, O. Gwon, H. Kim, and H. Joo, "Synergistic interaction of perovskite oxides and N-doped graphene in versatile electrocatalyst †," *J. Mater. Chem. A*, 2018.

[111] Q. Sun *et al.*, "Double perovskite PrBaCo 2 O 5 . 5 : An efficient and stable electrocatalyst for hydrogen evolution reaction," *J. Power Sources*, vol. 427, no. April, pp. 194–200, 2019.

[112] A. Grimaud *et al.*, "Double perovskites as a family of highly active catalysts for oxygen evolution in alkaline solution," *Nat. Commun.*, vol. 4, no. 1, p. 2439, 2013.

[113] H. Sun, X. Xu, and Z. Hu, "Boosting oxygen evolution reaction activity of perovskite through introducing multi-elements synergy and building ordered structure," *J. Mater. Chem. A*, no. March, 2019.

[114] H. Sun, J. He, Z. Hu, C. Chen, W. Zhou, and Z. Shao, "Electrochimica Acta Multi-active sites derived from a single / double perovskite hybrid for highly ef fi cient water oxidation," *Electrochim. Acta*, vol. 299, pp. 926–932, 2019.

[115] H. Sun, G. Chen, Y. Zhu, B. Liu, W. Zhou, and Z. Shao, "B-Site Cation Ordered Double Perovskites as Efficient and Stable Electrocatalysts for Oxygen Evolution Reaction," *Chem. Eur. J.*, pp. 5722–5728, 2017.

[116] N. Kim *et al.*, "Oxygen-deficient triple perovskites as highly active and durable bifunctional electrocatalysts for oxygen electrode reactions," *Sci. Adv.*, 2018.

[117] J. Wang *et al.*, "Water Splitting with an Enhanced Bifunctional Double Perovskite," *ACS Catal.*, vol. 8, no. 1, pp. 364–371, Jan. 2018.

[118] K. J. Stevenson, "Highly Active, Nonprecious Metal Perovskite Electrocatalysts for Bifunctional Metal − Air Battery Electrodes," *J. Phys. Chem. Lett.*, pp. 1254–1259, 2013.

[119] J. Kim, X. Chen, P.-C. Shih, and H. Yang, "Porous Perovskite-Type Lanthanum Cobaltite as Electrocatalysts toward Oxygen Evolution Reaction," *ACS Sustain. Chem. Eng.*, vol. 5, no. 11, pp. 10910–10917, 2017.

[120] S. K. Tiwari, P. Chartier, and R. N. Singh, "Preparation of Perovskite-Type Oxides of Cobalt by the Malic Acid Aided Process and Their Electrocatalytic Surface Properties in Relation to Oxygen Evolution," *J. Electrochem. Soc.*, vol. 142, no. 1, pp. 148–153, 1995.

[121] M. Yuasa, N. Tachibana, and K. Shimanoe, "Oxygen Reduction Activity of Carbon-Supported La1−xCaxMn1−yFeyO3 Nanoparticles," *Chem. Mater.*, 2013.

[122] Y. Chang, Y. Hsieh, P. Wu, C. Lai, and T. Chang, "Enhancement of bifunctional catalysis by Ir doping of La 0 . 6 Ca 0 . 4 CoO 3 perovskites," *Mater. Lett.*, vol. 62, pp. 4220–4222, 2008.

[123] S. Park, E. Lee, H. Song, and Y. Kim, "Bifunctional enhancement of oxygen reduction reaction activity on Ag catalysts due to water activation on LaMnO 3 supports in alkaline media," *Nat. Publ. Gr.*, no. August, pp. 1–14, 2015.

[124] M. I. Silva, "PtRu / C-LaNiO 3 Composite Electrodes for Electrocatalysis," *J. Electrochem. Soc.*, vol. 160, no. 10, pp. 1138–1142, 2013.

[125] X. Han, F. Cheng, T. Zhang, J. Yang, Y. Hu, and J. Chen, "Hydrogenated Uniform Pt Clusters Supported on Porous CaMnO 3 as a Bifunctional Electrocatalyst for Enhanced Oxygen Reduction and Evolution," *Adv. Mater.*, no. April, 2014.

[126] T. D. Thanh, N. D. Chuong, J. Balamurugan, H. Van Hien, N. H. Kim, and J. H. Lee, "Porous Hollow-Structured LaNiO3 Stabilized N, S-Codoped Graphene as an Active Electrocatalyst for Oxygen Reduction Reaction," *Small*, vol. 13, no. 39, p.

1701884, 2017.

[127] J. Mathias, “How Does FTIR Work_ _ Innovatech Labs.” 2015.

[128] J. M. Thomas, *Heterogenous catalysis*. Wiley-VCH, 2015.

[129] D. Lidzey, “Cyclic Voltammetry: Basic Principles & Set Up.” .

[130] C. Sophia and J. M. Gohil, “Chapter 19 - Microbial Desalination Cell Technology: Functions and Future Prospects,” P. P. Kundu and K. B. T.-P. and R. T. in M. F. C. Dutta, Eds. Elsevier, 2018, pp. 399–422.

[131] J. Xu, X. Zhou, X. Dong, L. Pan, and K. Sun, “Catalytic activity of infiltrated La0.3Sr0.7Ti0.3Fe0.7O3−δ–CeO2 as a composite SOFC anode material for H2 and CO oxidation,” *Int. J. Hydrogen Energy*, vol. 42, no. 23, pp. 15632–15640, 2017.

[132] R. Khan *et al.*, “Role of perovskites as a bi-functional catalyst for electrochemical water splitting: A review,” *Int. J. Energy Res.*, vol. n/a, no. n/a, Jul. 2020.

[133] P. Wang *et al.*, “Three-Dimensional Heterostructured NiCoP@NiMn-Layered Double Hydroxide Arrays Supported on Ni Foam as a Bifunctional Electrocatalyst for Overall Water Splitting,” *Appl. Mater. Interfaces*, vol. 12, pp. 4385–4395, 2020.

[134] X. Ge, C. Gu, Z. Yin, X. Wang, J. Tu, and J. Li, “Periodic stacking of 2D charged sheets: Self-assembled superlattice of Ni–Al layered double hydroxide (LDH) and reduced graphene oxide,” *Nano Energy*, vol. 20, pp. 185–193, 2016.

[135] F. Wang, T. Wang, S. Sun, Y. Xu, R. Yu, and H. Li, “n,” *Sci. Rep.*, vol. 8, no. 1, pp. 1–10, 2018.

[136] X. Zhang *et al.*, “Synergistic effects of lanthanum and strontium to enhance the osteogenic activity of TiO2 nanotube biological interface,” *Ceram. Int.*, no. February, pp. 0–1, 2020.

[137] K. J. May *et al.*, “Influence of Oxygen Evolution during Water Oxidation on the Surface of Perovskite Oxide Catalysts,” *J. Phys. Chem. Lett.*, vol. 3, no. 22, pp.

3264–3270, Nov. 2012.

[138] J. Zhou, M. Min, Y. Liu, J. Tang, and W. Tang, “Layered assembly of NiMn-layered double hydroxide on graphene oxide for enhanced non-enzymatic sugars and hydrogen peroxide detection,” *Sensors Actuators, B Chem.*, vol. 260, no. May, pp. 408–417, 2018.

[139] W. Guo *et al.*, “High-Stacking-Density, Superior-Roughness LDH Bridged with Vertically Aligned Graphene for High-Performance Asymmetric Supercapacitors,” *Small*, vol. 13, no. 37, pp. 1–9, 2017.

[140] S. Yu *et al.*, “Synthesis of NiMn-LDH Nanosheet@Ni3S2 Nanorod Hybrid Structures for Supercapacitor Electrode Materials with Ultrahigh Specific Capacitance,” *Sci. Rep.*, vol. 8, no. 1, pp. 1–12, 2018.

[141] H. Chen, L. Hu, M. Chen, Y. Yan, and L. Wu, “Nickel–Cobalt Layered Double Hydroxide Nanosheets for High-performance Supercapacitor Electrode Materials,” *Adv. Funct. Mater.*, vol. 24, no. 7, pp. 934–942, Feb. 2014.

[142] D. P. Dubal, G. S. Gund, C. D. Lokhande, and R. Holze, “Decoration of Spongelike Ni(OH)2 Nanoparticles onto MWCNTs Using an Easily Manipulated Chemical Protocol for Supercapacitors,” *ACS Appl. Mater. Interfaces*, vol. 5, no. 7, pp. 2446–2454, Apr. 2013.

[143] A. Sivanantham, P. Ganesan, and S. Shanmugam, “Hierarchical NiCo2S4 Nanowire Arrays Supported on Ni Foam: An Efficient and Durable Bifunctional Electrocatalyst for Oxygen and Hydrogen Evolution Reactions,” *Adv. Funct. Mater.*, vol. 26, no. 26, pp. 4661–4672, Jul. 2016.

[144] L. Yu *et al.*, “Cu nanowires shelled with NiFe layered double hydroxide nanosheets as bifunctional electrocatalysts for overall water splitting,” *Energy Environ. Sci.*, vol. 10, no. 8, pp. 1820–1827, 2017.

[145] Q. Hu *et al.*, “Crafting MoC2-doped bimetallic alloy nanoparticles encapsulated within N-doped graphene as roust bifunctional electrocatalysts for overall water splitting,” *Nano Energy*, vol. 50, no. May, pp. 212–219, 2018.

[146] M. M. Baig, I. H. Gul, M. Z. Khan, M. T. Mehran, and M. S. Akhtar, “Binder-free heterostructured MWCNTs/Al2S3 decorated on NiCo foam as highly reversible cathode material for high-performance supercapacitors,” *Electrochim. Acta*, vol. 340, p. 135955, 2020.

[147] Y. Gogotsi and R. M. Penner, “Energy Storage in Nanomaterials – Capacitive, Pseudocapacitive, or Battery-like?,” *ACS Nano*, vol. 12, no. 3, pp. 2081–2083, Mar. 2018.

[148] J. Liu *et al.*, “Hierarchical NiCo2S4 @ NiFe LDH Heterostructures Supported on Nickel Foam for Enhanced Overall-Water-Splitting Activity Hierarchical NiCo 2 S 4 @ NiFe LDH Heterostructures Supported on Nickel Foam for Enhanced Overall-Water-Splitting Activity,” 2017.

[149] Y. Bu, S. Kim, O. Kwon, Q. Zhong, and G. Kim, “A Composite Catalyst Based on Perovskites for Overall Water Splitting in Alkaline Conditions,” *Chemelectrochem Commun.*, pp. 1520–1524, 2019.

[150] A. Yan, X. Wang, and J. Cheng, “Research Progress of NiMn Layered Double Hydroxides for Supercapacitors : A Review,” pp. 1–17, 2018.

[151] F. Yusoff, N. Mohamed, A. Aziz, and S. A. Ghani, “Electrocatalytic Reduction of Oxygen at Perovskite (BSCF) -MWCNT Composite Electrodes,” no. March, pp. 199–211, 2014.

[152] N. E. A. Shuhaimi, L. P. Teo, H. J. Woo, S. R. Majid, and A. K. Arof, “Electrical double-layer capacitors with plasticized polymer electrolyte based on methyl cellulose,” *Polym. Bull.*, vol. 69, no. 7, pp. 807–826, 2012.

[153] Y.-P. Gao, K.-J. Huang, X. Wu, Z.-Q. Hou, and Y.-Y. Liu, “MoS2 nanosheets assembling three-dimensional nanospheres for enhanced-performance supercapacitor,” *J. Alloys Compd.*, vol. 741, pp. 174–181, 2018.

[154] R. B. Rakhi, B. Ahmed, D. Anjum, and H. N. Alshareef, “Direct Chemical Synthesis of MnO2 Nanowhiskers on Transition-Metal Carbide Surfaces for Supercapacitor Applications,” *ACS Appl. Mater. Interfaces*, vol. 8, no. 29, pp.

18806–18814, 2016.

[155] B. A. Mohamed Alhabeb, Kathleen Maleski and and Y. G. Pavel Lelyukh, Leah Clark, Saleesha Sin, “Guidelines for Synthesis and Processing of 2D Titanium Carbide (Ti3C2Tx MXene).” ACS Publications, pp. 7633–7644.

[156] J. Halim, *Synthesis and transport properties of 2D transition metal carbides (MXenes)*, no. October. 2018.

[157] Z. Li *et al.*, “Highly conductive dodecaborate/MXene composites for high performance supercapacitors,” *Nano Res.*, vol. 13, no. 1, pp. 196–202, 2020.

[158] Y. Wen *et al.*, “Synergistic cerium doping and MXene coupling in layered double hydroxides as efficient electrocatalysts for oxygen evolution,” *J. Energy Chem.*, vol. 52, pp. 412–420, 2020.

[159] J. Zhu, Y. Tang, C. Yang, F. Wang, and M. Cao, “ Composites of TiO 2 Nanoparticles Deposited on Ti 3 C 2 MXene Nanosheets with Enhanced Electrochemical Performance ,” *J. Electrochem. Soc.*, vol. 163, no. 5, pp. A785–A791, 2016.

[160] A. Manuscript, “The Formation and Detection Techniques of Oxygen Vacancies in Titanium Oxide-based Nano-structures,” *Nanoscale*, vol. 11, pp. 3414–3444, 2019.

[161] R. B. Rakhi, P. Nayuk, C. Xia, and H. N. Alshareef, “Novel amperometric glucose biosensor based on MXene nanocomposite,” *Sci. Rep.*, vol. 6, no. November, 2016.

[162] Q. Yue *et al.*, “Hierarchical Mesoporous MXene-NiCoP Electrocatalyst for Water-Splitting,” *ACS Appl. Mater. Interfaces*, vol. 12, no. 16, pp. 18570–18577, 2020.

[163] Y. Zhu, J. Dai, W. Zhou, Y. Zhong, H. Wang, and Z. Shao, “Synergistically enhanced hydrogen evolution electrocatalysis by in situ exsolution of metallic nanoparticles on perovskites,” *J. Mater. Chem. A*, vol. 6, no. 28, pp. 13582–13587, 2018.

[164] T. Shinagawa, A. T. Garcia-esparza, and K. Takanabe, “Insight on Tafel slopes

from a microkinetic analysis of aqueous electrocatalysis for energy conversion," *Nat. Publ. Gr.*, no. August, pp. 1–21, 2015.

[165] H. Pan, "Ultra-high electrochemical catalytic activity of MXenes," *Nat. Publ. Gr.*, no. April, pp. 1–10, 2016.

[166] Y. Wen, Z. Wei, X. Xing, Z. Li, and D. Luo, "MXene Boosted CoNi-ZIF-67 as Highly E ffi cient Electrocatalysts for Oxygen Evolution," 2019.

[167] X. Zhu, Y. Xie, and Y. Liu, "Exploring the synergy of 2D MXene-supported black phosphorus quantum dots in hydrogen and oxygen evolution reactions†," vol. 6, pp. 21255–21260, 2018.

[168] R. Z. Batteries, "A Highly Efficient and Robust Cation Ordered Perovskite Oxide as a Bifunctional Catalyst for Rechargeable Zinc-Air Batteries," *ACS Nano*, pp. 11594–11601, 2017.

[169] P. P. Nb and C. T. Mxene, "Rational design of bifunctional ORR/OER catalysts based on Pt/Pd-doped Nb2CT2 MXene by firstprinciples calculations†," *J. Mater. Chem. A*, 2020.

[170] M. Risch *et al.*, "Structural Changes of Cobalt-Based Perovskites upon Water Oxidation Investigated by EXAFS," *J. Phys. Chem. C*, vol. 117, no. 17, pp. 8628–8635, May 2013.

[171] A. A. Case, B. Sr, and C. Fe, "Electrochimica Acta Toward Enhanced Oxygen Evolution on Perovskite Oxides Synthesized," *Electrochim. Acta*, vol. 219, pp. 553–559, 2016.

Appendices

Table 9: *Results for OER shown by various Perovskites.*

Ref #	Catalyst	Group	Preparation	Characteristics BET surface area m^2/g	Tafel slope mV dec^{-1}	Onset Potential V
[47]	LaFeO3 (LF) 3DOM-LF 3DOM-LFC82 $LaFe_{0.8}Co_{0.2}O_3$(LFC82)	B-site Co doped perovskite	Colloidal crystal template method	8 20 16 6	72 62 56 70	1.61 1.59 1.57 1.62
[82]	$LaFeO_3$ (LF) (LaSrFe)-0.2 (LaSrFe)-0.5 LaSrFe-0.8 SrFe	A-site Sr doped perovskite	Synthesized using a sol-gel route	 2	76.96 72.35 68.05 60.10 74.92	1.64 1.62 1.58 1.54 1.59
[171]	BSCF-SS BSCF-SC BSCF-SG	A-site Sr and B-site Fe doped oxygen deficient perovskite	Solution combustion, sol-gel process and solid-state reaction	0.52 0.8 1.05	N.A.	N.A.
[92]	$SrFe_{0.9}Si_{0.1}O_{3-\delta}$ (SFSi) SF	B-site Si doped oxygen deficient perovskite	Solid-state reaction	N.A.	58 70	N.A.
[8]	$PrBa_{0.5}Sr_{0.5}Co_{2-x}Fe_xO_{5+\delta}$ (x = 0-2) PBSCF-NF BSCF	A and B-site doped double perovskite	Electrospinning	20 16.2	121 81 196	N.A.
[105]	n-SnNiFe p-SnNiFe.	B-site Fe doped perovskite	In situ co-precipitation. MGF is manufactured by chemical vapor deposition (CVD) method	N.A.	35 45.9	N.A.
[119]	$LaCoO_3$ porous nanostructures hollow spheres	Nanostructured perovskite	hydrothermal synthesis	14.6 11.4	74 72	1.5

[85]	$LaCo_{1-x}Fe_xO_3$ (x = 0 -1)	B-site Fe doped perovskite	Sol−gel method	12 13 14 15	N.A.	N.A.
[83]	Urchin-like $La_{0.8}Sr_{0.2}MnO_3$ (LSM)	A-site Sr doped perovskite	Coprecipitation method with urea as a precipitator	48	N.A.	0.6
[78]	$Ba_{0.5}Sr_{0.5}Co_{0.8}Fe_{0.2}O_3$	A/B-site doped perovskite	Sol-gel method	2.78	N.A.	0.5
[98]	$Fe_xCr_{2-x}(MoO_4)_3$ (x = 0 - 0.75)	B-site Fe doped	Co-precipitation method	9.9 2.7 2.8 1.7	N.A.	N.A.
[108]	SNCF-NR SNCF	B-site Co & Fe doped perovskite	By electrospinning	45	76 61	1.52
[120]	$Ni/LaCoO_3$ $Ni/La_{0.8}Sr_{0.2}CoO_3$ $Ni/La_{0.6}Sr_{0.4}CoO_3$ $Ni/La_{0.8}Sr_{0.2}CoO_3$ $Pt/La_{0.8}Sr_{0.2}CoO_3$	Perovskite composites	Malic acid aided method Nitrate decomposition method	N.A.	60 63 60 59 61	N.A.
[86]	$La_{0.8}Sr_{0.2}CoO_3$ $La_{0.8}Sr_{0.2}Co_{0.9}Fe_{0.1}O_3$ $La_{0.8}Sr_{0.2}Co_{0.8}Fe_{0.2}O_3$ $La_{0.8}Sr_{0.2}Co_{0.6}Fe_{0.4}O_3$ $La_{0.8}Sr_{0.2}Co_{0.9}Ni_{0.1}O_3$ $La_{0.8}Sr_{0.2}Co_{0.8}Ni_{0.2}O_3$ $La_{0.8}Sr_{0.2}Co_{0.6}Ni_{0.4}O_3$ $La_{0.8}Sr_{0.2}Co_{0.8}Cu_{0.2}O_3$ $La_{0.8}Sr_{0.2}Co_{0.8}Cr_{0.2}O_3$ $La_{0.8}Sr_{0.2}Co_{0.8}Fe_{0.1}Ni_{0.1}O_3$ $La_{0.8}Sr_{0.2}Co_{0.6}Fe_{0.2}Ni_{0.2}O_3$	A-site Sr and B-site Fe doped B-site Fe doped B-site Fe doped B-site Ni doped B-site Ni doped B-site Ni doped B-site Cu doped B-site Cr doped B-site Fe & Ni doped perovskite	N.A.	N.A.	63 56 51 55 66 61 55 55 60 67 54	N.A.

[116]	($Nd_{1.5}Ba_{1.5}CoFeMnO_{9-\delta}$) NBCFM NBSCF NBCFM/N-rGO	A/B site doped ternary perovskite composite with reduced graphene oxide	Glycine-nitrate combustion method	7.1 4.6 119.6	81 84 88	N.A.
[100]	MS $CaMnO_{2.93}$ MS $CaMnO_{2.76}$ MS $CaMnO_{2.5}$ NP $CaMnO_{2.9}$ NP $CaMnO_{2.77}$	Oxygen deficient perovskite	Controllable thermal reduction of pristine and pechini route	N.A.	65 63 67 62 59	N.A.
[101]	$Ca_2Mn_2O_5$/C $CaMnO_3$/C	Double perovskite supported on carbon	Facile reductive annealing process	N.A.	149 197	N.A.
[109]	LSFM-SBA(Santa Barbara Amorphous) LSFM-HMS(Hexagonal mesoporous silica) LSFM-AS(Amorphous silica) LSFM	A-site Sr and B-site Mn doped perovskite	Soft hard templating method	150 53 25 25	37 96 44 80 61 112 83 128	N.A.
[93]	LF La0.98Fe La0.95Fe La0.9Fe	A-site cation deficient perovskite	Standard combined EDTA citrate complexing sol-gel process	N.A.	77 59 48 54	N.A.
[99]	LaNi-RT LaNi-400 LaNi-600 LaNi-800	Oxygen deficient perovskite	Combined EDTA−citrate complexing process	N.A.	104 94 92 80	N.A.
[113]	$Sr_2Fe_{0.8}Co_{0.2}Mo_{0.65}Ni_{0.35}O_{6-\delta}$ SFMN	A/B-site doped double perovskite	Sol-gel	4	56 61	0.19 0.252
[106]	LNF-t-d LNF-b-u C-LNF LN	B-site Fe doped perovskite	Co-precipitation	157 159 6.3 2.3	36 73 47 115	1.44 1.47 1.52 1.57
[110]	P-3G P-HF 3DNG	Double perovskite composite with N doped reduced	N.A.	N.A.	74 119 183	1.52 1.54 1.64

		graphene oxide				
[95]	S0.9NCF S0.95NCF S0.98NCF SNCF	B-ste doped A-site cation deficient perovskite	Solid-state reaction	N.A.	77 70 74 85	1.53 1.52 1.53 1.53
[94]	$Sr_{0.95}Co_{0.8}Nb_{0.1}Ni_{0.1}O_{3-\delta}$	B-ste doped A-site cation deficient perovskite	Non-aqueous sol-gel method	N.A.	64	1.55
[91]	BCMN	B-site Mn & Nb doped double perovskite	Solid state reaction	N.A.	77	1.6
[114]	BC1.5MN	-site doped double perovskite	Solid-state reaction	N.A.	70	0.26

Table 10: *Elemental distribution of elements in electrocatalyst LSTN@NiMn-LDH*

Element	Atomic %
OK	37.26
SrK	0.68
LaK	0.99
TiK	01.99
MnK	01.20
NiK	57.88
Matrix ZAF	ZAF

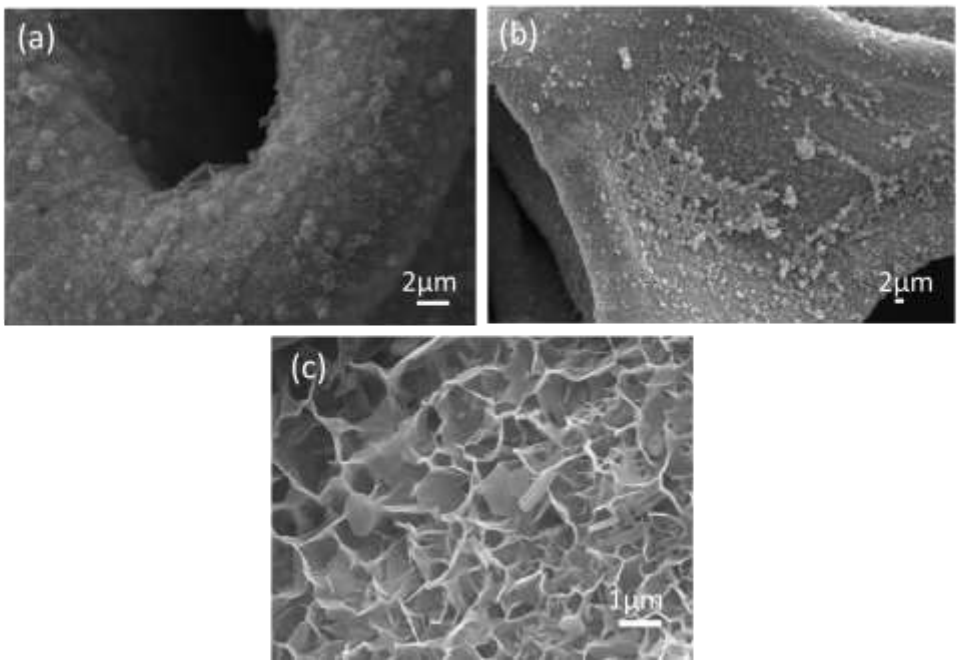

Figure 44: *(a, b) SEM images of LSTN@NiMn-LDH supported on nickel foam at different magnifications. (c) SEM image of LSTN@NiMn-LDH after performing HER & OER tests.*